Project Title:

Low Cost High Performance Phased Array Antennas with Beam Steering Capabilities
(N00014-06-1-1173)

Technical Point of Contact:
Project Manager
Magdy F. Iskander, PhD
Hawaii Center for Advanced Communications
University of Hawaii at Manoa
1680 East West Road, POST 201
Honolulu, HI, 96822
Tel: 808 956 3434
Fax: 808 956 5746
Email : magdy@hawaii.edu

REPORT DOCUMENTATION PAGE

1. REPORT DATE *(DD-MM-YYYY)*	2. REPORT TYPE		3. DATES COVERED *(From - To)*
	Final Technical		September 2006 through December 2009

4. TITLE AND SUBTITLE	5a. CONTRACT NUMBER
Low Cost High Performance Phased Array Antennas with Beam Steering Capabilities Using an Integrated CTS and Ferroelectric Materials Technologies	n/a
	5b. GRANT NUMBER
	N00014-06-1-1173
	5c. PROGRAM ELEMENT NUMBER
	1152AB

6. AUTHOR(S)	5d. PROJECT NUMBER
Iskander, Magdy F.	09PR04346-00
	5e. TASK NUMBER
	n/a
	5f. WORK UNIT NUMBER
	n/a

7. PERFORMING ORGANIZATION NAME(S) AND ADDRESS(ES)	8. PERFORMING ORGANIZATION REPORT NUMBER
University of Hawaii 2530 Dole Street, Sakamaki D-200 Honolulu, Hawaii 96822	0W411

9. SPONSORING/MONITORING AGENCY NAME(S) AND ADDRESS(ES)	10. SPONSOR/MONITOR'S ACRONYM(S)
Office of Naval Research 875 North Randolph Street Arlington, VA 22203-1995	ONR
	11. SPONSOR/MONITOR'S REPORT NUMBER(S)

12. DISTRIBUTION/AVAILABILITY STATEMENT

Approved for public release; distribution unlimited.

13. SUPPLEMENTARY NOTES

The views, opinions and/or findings contained in this report are those of the author(s) and should not be construed as an official Department of the Army position, policy or decision, unless so designated by other documentation.

14. ABSTRACT

In this report, we focused on fabricating the tunable ferroelectric phase shifter and verifying the simulation results with the fabricated device. To achieve low loss and high tunable characteristics of BSTO, the RF vacuum sputtering technique has been used and we investigated effects of sputtering parameters such as substrate temperature, sputtering pressure, and gas mixture ration on properties of BSTO. Optimal sputtering conditions for BSTO deposition were determined based on epitaxial qualities characterized by the RBS-channeling spectrometry, which will be discussed in later part of the report. Using the optimized sputtering parameters, various sets of BSTO films have been deposited on different substrates and various size of CPW phase shifters have been fabricated on the BSTO layer using lift-off process. RF performances of the fabricated ferroelectric CPW phase shifters were characterized by using on-wafer probe station connected to a vector network analyzer. The fabrication procedures of ferroelectric phase shifters are described and the experimental measurement data are compared with simulated results for verification.

15. SUBJECT TERMS

16. SECURITY CLASSIFICATION OF:			17. LIMITATION OF ABSTRACT	18. NUMBER OF PAGES	19a. NAME OF RESPONSIBLE PERSON
a. REPORT	b. ABSTRACT	c. THIS PAGE			Magdy F. Iskander
U	U	U	UU		**19b. TELEPHONE NUMBER** *(Include area code)* 808-956-3434

Table of Contents

Executive Summary

The objective of the proposed work is to develop a high performance low cost antenna array using integrated Continuous Transverse Stub (CTS) and Ferroelectric material technologies. Tasks included the design of a CTS antenna array in the Ka-Band with bandwidth of over 1GHz, simulation of the beam steering capability of an integrated CTS array with ferroelectric phase shifters placed between the antenna array elements, the fabrication and characterization of multi-dielectric layers ferroelectric phase shifters, and the possible evaluation of a complete integrated antenna array design with the proposed ferroelectric material phase shifters.

Accomplished tasks include a successful design of the Ka-band CTS antenna array with over 1 GHz bandwidth, the simulation of the integrated CTS antenna array performance with multi-dielectric layer ferroelectric phase shifters, conducting a comparative study between the multi- and single- layer coplanar waveguide ferroelectric phase shifters designs, and the more recent successful fabrication and characterization of ferroelectric phase shifters. Results from the CTS antenna design work may be found in references [1-4], and results from the comparative study of the single- and multilayer ferroelectric phase shifters may be found in [5-7]. Simulation results that demonstrate the feasibility of using the integrated CTS and ferroelectric materials approach for designing high performance phased antenna array can also be found in reference [8]. In this case it is shown that while this approach is feasible, inclusion of thicker layer of ferroelectric material will be required to achieve beam steering more than $\pm 20^{0}$. To avoid the use of thicker ferroelectric layers and the corresponding need for a larger DC bias voltage, an approach in which analog phase shifting would be accomplished using the proposed technology while larger phase shifts would be achieved using available digital technologies. It is believed that this combined analog (small beam steering angles) and digital (large steering angles) would lead to

3

optimum phased antenna array designs with performance, cost, and required DC bias voltage all taken into consideration.

As the results of the antenna array design and the simulated performance of the integrated CTS and ferroelectric antenna array are available in articles published by our group [1-8], focus in this report is placed on the fabrication and characterization aspect of the ferroelectric phase shifters. While our group has been successful in fabricating thin film ferroelectric phase shifter with as much as 27 degrees of phase shifts at 20 GHz, work is still underway to help develop multilayer ferroelectric phase shifters as well as on the development of an integrated CTS and ferroelectric phased antenna array. We hope that we will be able to attract additional funding to help us complete the development of this innovative phased antenna array technology.

Low Cost High Performance Phased Array Antennas with Beam Steering Capabilities

1. Introduction

Low cost and high performance steerable antennas have been a critically important and challenging topic in satellite communication, radar, navigation, remote sensing, and space exploration. Ferroelectric tunable RF devices such as phase shifters and RF switches incorporated into high performance phased-array antennas with beam steering capabilities are one promising technology to satisfy these requirements. While many emerging designs and alternative approaches are being developed to help achieve the desired high RF performance and low cost objectives, there is still a need for fresh ideas that may provide complementary avenues to other ongoing research. For example, while some are continuing with the development of the MEMs technology with focus on overcoming some of the remaining difficulties including RF packaging, reliability, reducing the response time, and lowering the required switching voltages, others are pursuing the development of metamaterials and Electromagnetic Band Gap Surfaces (EPG) to help develop new devices say with reduced size, multiband capabilities, or to enhance the performance by increasing gain and mitigating interferences.

In our research, we investigate development of the low cost ferroelectric tunable RF devices and integrated phased antenna arrays with beam steering capabilities. Ferroelectric materials are characterized by change in permittivity with an applied dc-bias voltage. This change in permittivity can be used to change the electrical length of a transmission line and, hence, in the design of low-cost phase shifters. Furthermore, the ferroelectric material can be embedded in phased array antenna designs such as that based on the Continuous Transverse Stub (CTS)

5

technology [1-4], leading to an integrated antenna array design with beam steering capability. [5-8]

The most popular ferroelectric material for room temperature operation is $Ba_xSr_{1-x}TiO_3$ (BSTO) where varying x can vary the maximum of the dielectric constant. However, BSTO films had suffered from a high loss tangent. Many researches have been conducted to improve the high loss characteristics of BSTO and recent advances in the development of this material have resulted in decreasing the loss tangent (0.001) by using dopants [9], and increasing the tunability by annealing process [10]. It was, however, generally felt that designs based on this technology, although low cost, still exhibited unacceptably high insertion losses and impractical low input impedance values. Specifically, input impedance values for microstrip and parallel plate waveguide type structures were too small for utilization in practical designs. Furthermore, Ohmic losses are unacceptably high in addition to the input impedance issues. Therefore, in order to address such high insertion losses and the unacceptably low input impedance values, HCAC proposed a new phase-shifter design procedure that was based on the use of "multi-dielectric" layers substrate including a middle layer of highly tunable ferroelectric material [6-8] and numerically verified that this approach significantly reduced the insertion losses, while maintaining a large percentage (85%) of the tunability.[8] This multilayer-dielectric loading technique involves a novel biasing procedure for the ferroelectric layer beneath the low dielectric layer. The recently developed coplanar waveguide (CPW) version of the CTS technology [3,4] can be integrated with this multilayer ferroelectric tunable RF component to achieve high performance and low cost phased antenna arrays. It is believed that the application of the multi-dielectric layers in this new CPW-CTS antenna design is ready to provide the much anticipated breakthrough in developing low cost antenna arrays with beam steering capabilities. Unlike any

6

other approach, the multilayer ferroelectric CPW-CTS antenna is based on "integrating the phase shifters with the antenna element," rather than as part of the electronics package, and as a result is expected to achieve a high system performance in addition to satisfying the much desired goal of reducing the cost. However, these encouraging preliminary studies were mainly conducted by using numerical simulation and still require experimental verification. Therefore, in this report, we focused on fabricating the tunable ferroelectric phase shifter and verifying the simulation results with the fabricated device. To achieve low loss and high tunable characteristics of BSTO, the RF vacuum sputtering technique has been used and we investigated effects of sputtering parameters such as substrate temperature, sputtering pressure, and gas mixture ration on properties of BSTO. Optimal sputtering conditions for BSTO deposition were determined based on epitaxial qualities characterized by the X-ray diffraction and RBS-channeling spectrometry, which will be discussed in later part of the report. Using the optimized sputtering parameters, various sets of BSTO films have been deposited on different substrates and various size of CPW phase shifters have been fabricated on the BSTO layer using lift-off process. RF performances of the fabricated ferroelectric CPW phase shifters were characterized by using on-wafer probe station connected to a vector network analyzer. In this report, the fabrication procedures of ferroelectric phase shifters will be described and the experimental measurement data will also be compared with simulated results for verification.

2. Analytical modeling and analysis of multi-dielectric layers Ferroelectric coplanar phase shifters

Many fundamental features regarding the operation of the coplanar waveguide CTS antenna are still unknown, and are necessary to understand before the performance of such a unique system could be optimized. This is particularly complicated by the fact that we intend to integrate the antenna structure with a layer of ferroelectric material which has significant

7

tunability property, very high permittivity, and tendency to change characteristics depending on thickness, type of interface, relative composition, and temperature. In a typical design parameters such as attenuation, impedance mismatch, higher order modes, and phase sensitivity versus thickness of and type of interface with the ferroelectric layer, need to carefully investigated. To this end, we have developed a spectral-domain approach which is an analytical method that together with numerical simulations will help in quantifying and providing answer to these questions.

As an example of this analytical procedure, Figure 1 illustrates the geometry of the thin-film ferroelectric coplanar phase shifter [11]. The structure uses Barium Strontium Titanate ($Ba_xSr_{1-x}TiO_3$) with a compositional ratio of $x = 0.6$ over a Lanthanum Aluminate ($LaAlO_3$) substrate. The total device width is 174µm, the ferroelectric layer thickness is 0.5µm, and the $LaAlO_3$ substrate layer thickness was 508µm. The relative dielectric constant for the $LaAlO_3$ substrate is $\varepsilon_r = 23.5$ with $\tan\delta = 3e-4$. The $\tan\delta$ for the $Ba_{0.6}Sr_{0.4}TiO_3$ material is 0.01. The center strip width is 32.76µm, the gap width is 16.4µm, and the conductor thickness is 1.5µm and is made of pure silver with resistivity $\rho = 1.629 \times 10^{-6} \, \Omega$ cm.

For the coplanar device, which is modeled as two coupled slots, with the fields in the slot locations expanded in a complete set of basis functions, the dyadic Green's function in admittance form is given by [6,11]:

$$G'_{ad} = \frac{1}{\det G'} \begin{bmatrix} G'_{zz} & -G'_{xz} \\ -G'_{zx} & G'_{xx} \end{bmatrix} \qquad (1)$$

where:

$$\det G' = G'_{xx} \, G'_{zz} - G'_{xz} \, G'_{zx} \qquad (2)$$

8

The Green's function in (1) is used in a system of homogenous equations to compute the propagation constant in the coplanar device as a function of frequency [6].
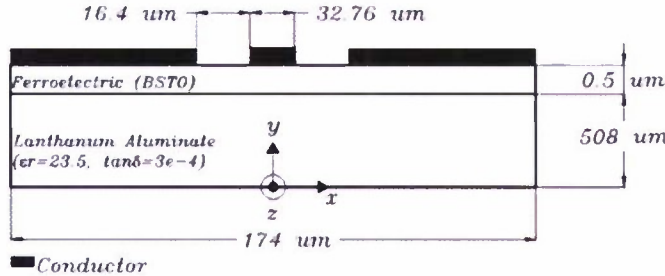

Figure 1. Cross section of ferroelectric coplanar waveguide phase shifter employing thin-film ferroelectric technology over Lanthanum Aluminate substrate.

For modeling attenuation, it is important to note that in the spectral domain approach described in [11], it was necessary to modify the self consistent admittance Green's function terms in (1) to account for extrinsic parameters such as the finite thickness of the conductors and to account for the substantial amount of field lines that couple between and penetrate laterally into the coplanar arrangement. This modification was implemented to the diagonal elements of (1) and is given by:

$$G'_{zz} = G_{zz} - \frac{1}{\sigma w_{eff}} \left\{ (1+j)\frac{t}{4\delta} + c(f)\frac{w_{cs}}{w_{cs} + 2w_{slot}} \cdot \left[\frac{\frac{(1+j)w_{cs}}{\delta}}{\tanh\left[\frac{(1+j)w_{cs}}{\delta}\right]} \right] \right\} \qquad (3)$$

where

$$c(f) = \left(\frac{f}{f_o}\right)^k \qquad \delta = \frac{1}{\sqrt{\pi f \mu_o \sigma}} \qquad (4)$$

9

where w_{cs} is the center conductor strip width, w_{slot} is the gap width of the coplanar waveguide device and w_{eff} is the newly quantified term, defined as the summation of the current crowding depths of the center and ground conductors [6]. A similar expression may also be used to modify the second diagonal term, $G'_{xx.}$

The relation between current and charge density distributions may be given by:

$$j_s(x) = q n_s(x) v = \rho_s v \quad (5)$$

where $n_s(x)$ is the surface charge concentration and q the electronic charge. Based on a study on the applicability of using a quasi-TEM approximation [13] we can assume no transverse currents in the CPW device, hence the charge velocity v is assumed to have only a longitudinal component and therefore the charge and current distributions are identical.

To quantify w_{eff} in the two layer substrate illustrated in Figure 1, we have employed the method of finite differences numerical method for multilayered structures as described in [6]. In this study, the effect of current crowding is quantified by introducing a current crowding depth (δ_{cc}), defined as the depth from the conductor edges at which 63% of the current is concentrated. The current crowding effect may be explained by the extremely high field confinement in the ferroelectric material as a result of the increase in permittivity. With increased film permittivity, the electric field is forced towards the edges of the electrodes, thus increasing the current crowding near the edges.

With the above definition, the current crowding may be defined as [14]:

$$\int_{s-\delta_{cc}}^{s} j_s(x) dx = \left(1 - \frac{1}{e}\right) \int_{0}^{s} j_s(x) dx \qquad (7)$$

where $j_s(x)$ is the surface current density, s is the width of the conductor, and e=2.718.

10

Based on the current crowding expression in (7), the effective width, w_{eff}, in the modifying Green's function term (3) may be expressed by:

$$w_{eff} = \delta_s + \delta_g \quad (8)$$

where w_{cs} is the width of the center strip, δ_s is the current crowding depth of the center strip, w_{gp} is the width of the ground plane, and δ_g is the current crowding depth of the ground plane. The charge/current distribution of the coplanar electrodes is illustrated in Figure 2(a) for the center conductor and Figure 2(b) for the ground plane conductor. The charge distribution is evaluated by multiplying the normal component of the electric field with the equivalent permittivity surrounding the electrodes and is given by:

$$\varepsilon_o \varepsilon_r E_{norm} = \rho_s \quad (9)$$


(a)   (b)
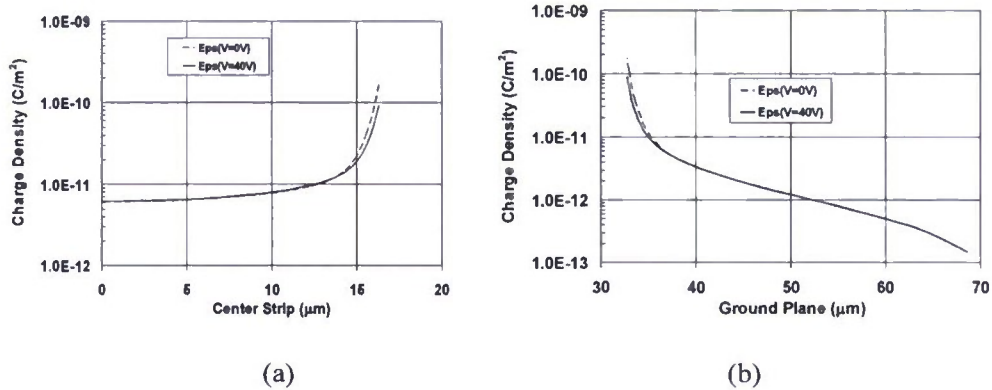
Figure 2. Charge distributions on the center strip conductor (a) and ground plane (b) for both biased and unbiased cases. Taking symmetry into account (see Figure 1), only one-half of the center strip (from x=0 to x=16.38μm) is illustrated.

The permittivity for the ferroelectric unbiased case was set to $\varepsilon_r(V=0V) = 440 - j440 \tan\delta_{fe}$, and the permittivity for the biased case was set to $\varepsilon_r(V=40V) = 187.4 - j187.4 \tan\delta_{fe}$ as was reported in [6] to satisfy both α and β simultaneously.

In an earlier publication we validated the accuracy of the developed spectral-domanin method by comparing with published experimental results [6]. Figure 3(a) shows example of these comparisons between the measured attenuation constant and the theoretical results from the above calculations, while Figure 3(b) shows the measured phase shift [11] compared with theory.
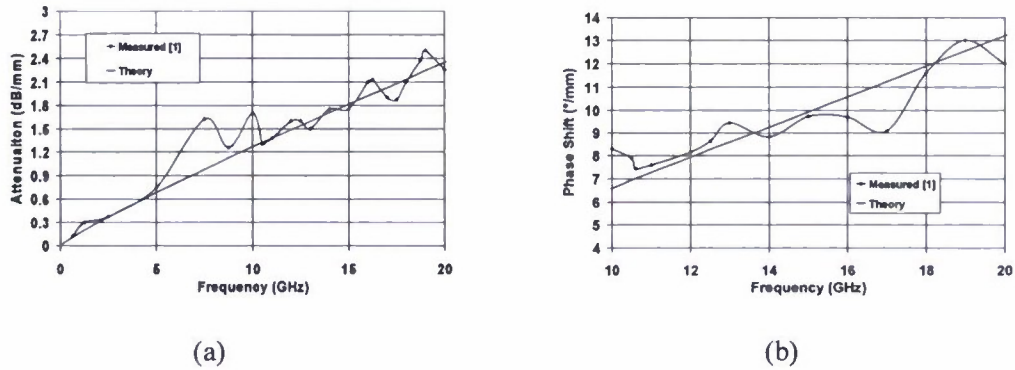

Figure 3. Attenuation constant α (a) and phase shift (b) comparing experimental data to theory.

As pointed out in [12], the experimental data between about 5 to 11 GHz was questionable and therefore should be ignored. Disregarding this region, the attenuation and propagation constants show excellent agreement between the experimental data and the presented theoretical results.

In the results shown in Figure 3 we analyzed the case where the coplanar conductors were placed directly on the ferroelectric material. This case where no multi-dielectric layer was used was analyzed first to help compare with experimental data published in literature [11]. As it may be noted, the measured attenuation constant illustrated in Figure 3 is too high for implementation

12

in phased array antenna systems due to the anticipated high scan loss and low radiation efficiencies. In an attempt to improve the phase shifter performance an alternate multi-dielectric layers design was proposed in [8]. Figure 4 depicts such a design of a multi-dielectric ferroelectric phase shifter design which is expected to reduce the attenuation constant and improve the FOM. The FOM is defined as the amount of phase shift per decibel loss, where the loss is calculated based on the unbiased condition. This new design was also analyzed modeled in this paper using the method of finite differences and newly developed spectral matrix method.
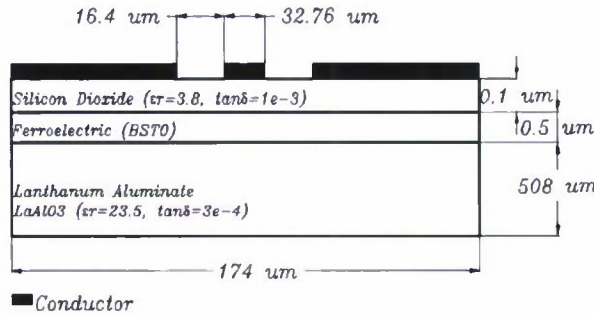

Figure 4. Cross section of multi-dielectric ferroelectric coplanar waveguide phase shifter employing very thin, non-tunable layer between the ferroelectric film and the coplanar electrodes.

Figures 5 compares the attenuation constant of the direct metallization design illustrated in Figure 1 to the multi-dielectric approach illustrated in Figure 5 for the unbiased and biased cases respectively. The attenuation constant decreased by ~1.85dB/mm at 20GHz for the unbiased case and decreased by ~1.07dB/mm at 20 GHz for the biased condition. Figure 6 depicts the FOM results and shows a significant increase in FOM that is primarily due to the large decrease in attenuation constant. The FOM increased by nearly a factor of four at 20GHz and illustrates that the multi-dielectric design improves the overall phase shifter performance.

(a)

(b)
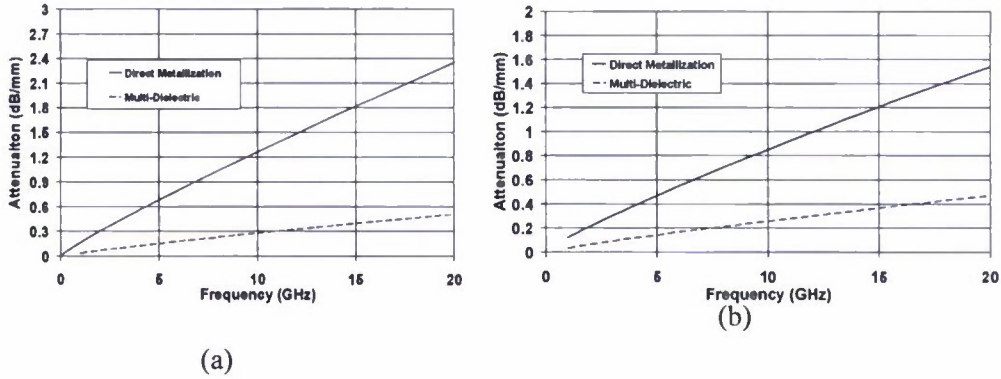
Figure 5. Attenuation constant α for (a) the unbiased case $\varepsilon_r(V=0V)$ and (b0 for the biased case (V=40 V)
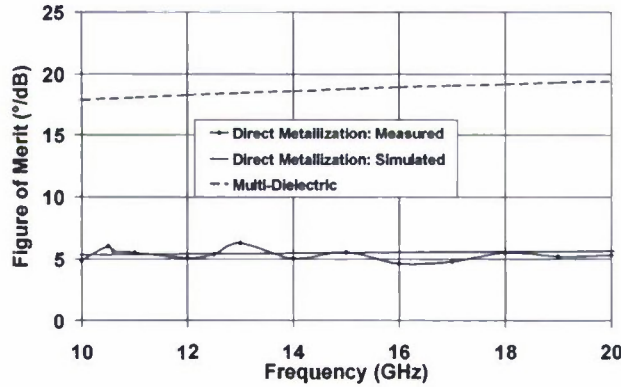
Figure 6. Figure of Merit comparing the direct metallization design shown in Figure 1 to the multi-dielectric phase shifter design shown in Figure 4.

The coplanar ferroelectric design employing multilayer substrate, therefore provided significant advantages over those when direct metallization of the electrodes with the ferroelectric material are used [8]. The developed spectral domain approach was useful in modeling these designs and the obtained results demonstrated nearly four fold increase in FOM, and hence the proposed procedure is attractive for implementation in phased array antenna systems.

14

3. RF sputtering system and On-wafer probe station

3.1 RF puttering system

In this report, the RF sputtering technology is employed for deposition of the BSTO ferroelectric film. The RF sputtering system, a vacuum chamber, and its schematic are shown in Figure 7. Strong magnetron is usually located close to the target (i.e. BSTO) and used as sputtering source which traps electrons close to the surface of the magnetron.

The electrons around the magnetic field undergoing more ionizing collisions with gaseous neutrals near the target surface. The sputter gas is inert, typically argon. The extra argon ions created as a result of these collisions leads to a higher deposition rate. The sputtered atoms are neutrally charged and so are unaffected by the magnetic trap. Charge build-up on insulating targets can be avoided with the use of RF sputtering where the sign of the anode-cathode bias is varied at a high rate. Stray magnetic fields leaking from ferromagnetic targets also disturb the sputtering process. Specially designed sputter guns with unusually strong permanent magnets should be used in compensation. RF sputtering works well to produce highly insulating films. However it requires RF power supplies and impedance matching networks. Our RF sputter system equipped four sputter magnetron guns and a RF power generator supply 13.56 MHz RF source (Max. power 600 W) together with the RF matching networks into the sputter guns. The sputter guns are oriented 30° off-axis and 15 cm from the substrate holder, which can accommodate up to 2" diameter. An Inconel heating block is installed into the substrate holder and the wafers can be heated up to 900 °C. The vacuum chamber is equipped with a rotary vacuum pump and a cryopump. The rotary pump is in charge of decompression down to 0.2 Torr as an initial buffer pressure state before the cryopump takes over the decompression process down to the maximum base vacuum pressure ($\sim 10^{-10}$ Torr).
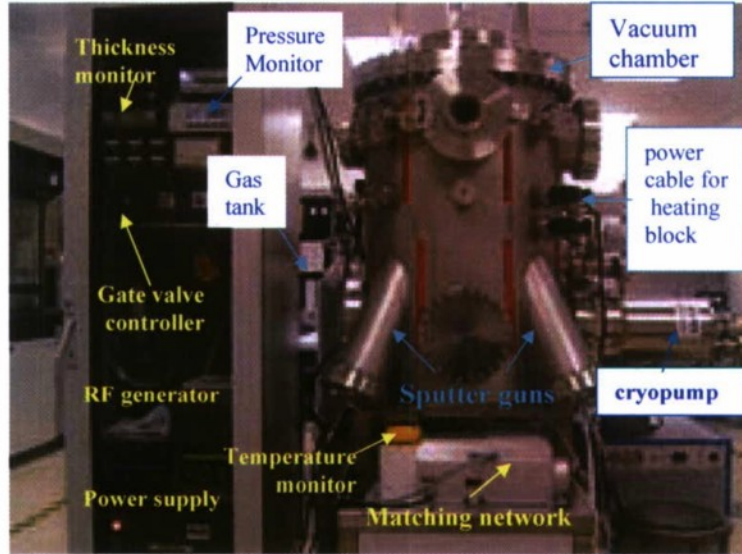
(a)　　　　　Sputter deposition chamber and devices.
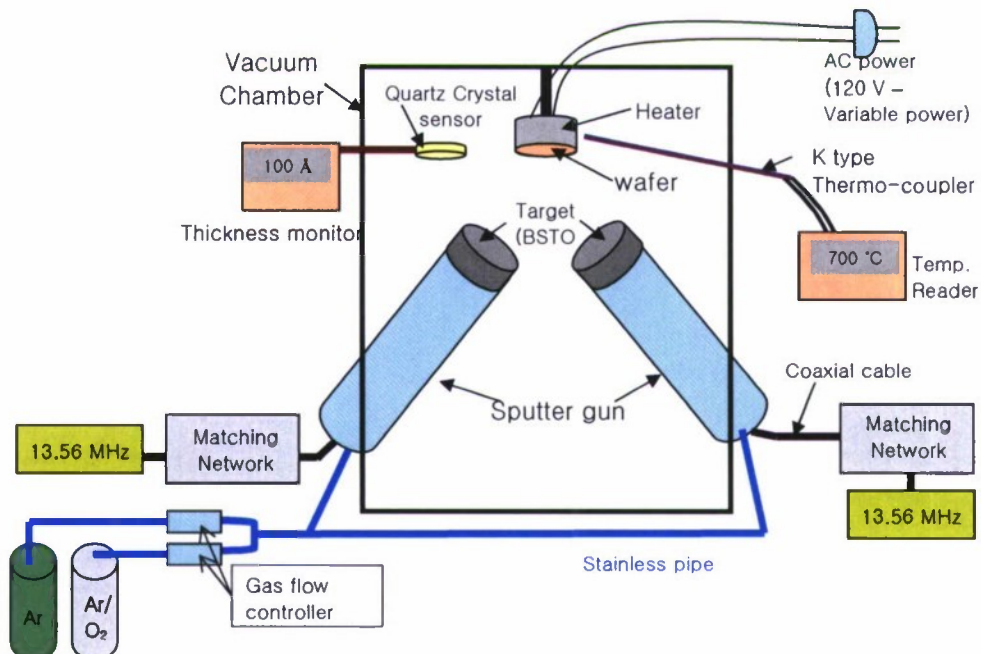
(b) Schematic of the RF sputter system.

Figure 7. The RF sputter system. The sputter guns are connected into RF source with matching network through a coaxial cable and Ar and Ar/O₂ gas tank with gas flow controllers through a stainless pipe. Heating block integrated with substrate (wafer) holder is connected into type K thermo-coupler. Quartz crystal sensor located close to the substrate holder is connected into a thickness monitor.

Control over gas composition and pressure is achieved using two independent flow controllers and a pneumatic three position gate valve. These gas flow controllers are capable of keeping a constant flow rate of gas into the chamber. While there is a constant flow rate of gas into the chamber during sputtering process, maintaining a fixed pressure inside the chamber plays an important role in targeting a desired microstructure property of the film. In order to monitor the chamber pressure, two separate pressure sensors are equipped in inside the chamber. Type K (chromel–alumel) thermo-coupler has been used to monitor the substrate temperature and a quartz crystal thickness sensor was used to monitor the deposition rate and thickness of the film.

3.2 Lift-off etching technique for fabricating small RF device

After depositing BSTO film on a wafer, lift-off etching techniques were used to fabricate the CPW phase shifter on the wafer. Lift-off process is a method of patterning structures (i.e. curcuitry) of a target material on the surface of a substrate (i.e. wafer) using a sacrificial material. It is an additive technique as opposed to more traditional subtracting technique like etching. The scale of the structures can vary from the nanoscale up to the centimeter scale or further. Thus the lift-off process is suitable for our ferroelectic CPW phase shifters discussed in this report since they require at least 1 μm resolution.

Figure 8 illustrates the procecure of the lift-off etching technique. Procedure of the lift-off etching starts from creating an inverse pattern in the sacrificial (stensiled) layer (i.e. photoresist layer) deposited on the surface of the substrate. The sacrificial layer covers certain area on the substrate and exposes the rest. The layer to be 'patterned' is then deposited over the stenciled wafer. In the exposed areas of the stencil, conducing (Cr and Cu) material gets deposited directly on the substrate, while in the covered areas, the material gets deposited on top of the stencil film. After the conducting layer has been deposited, the wafer is immersed in a liquid that can dissolve

17

the stencil layer. Once the stencil is dissolved by the liquid, the layer material over it gets 'lifted off', leaving behind the conducting layer that were deposited over the wafer substrate itself, which forms the final pattern on the wafer.

For sacrificial layer, the photoresist (S1813) has been selected and acetone was chosen as a dissolver. In order to deposit conducting layer, another RF sputtering process with 25 nm chrome (Cr) adhesion layer followed by a 1 µm thick cupper layer have been performed.

(a) Deposition of the sacrificial stencil layer

(b) Patterning the sacrificial

(c) Depostion of conduing layer

(e) Final pattern

(d) Lift off in Acetone
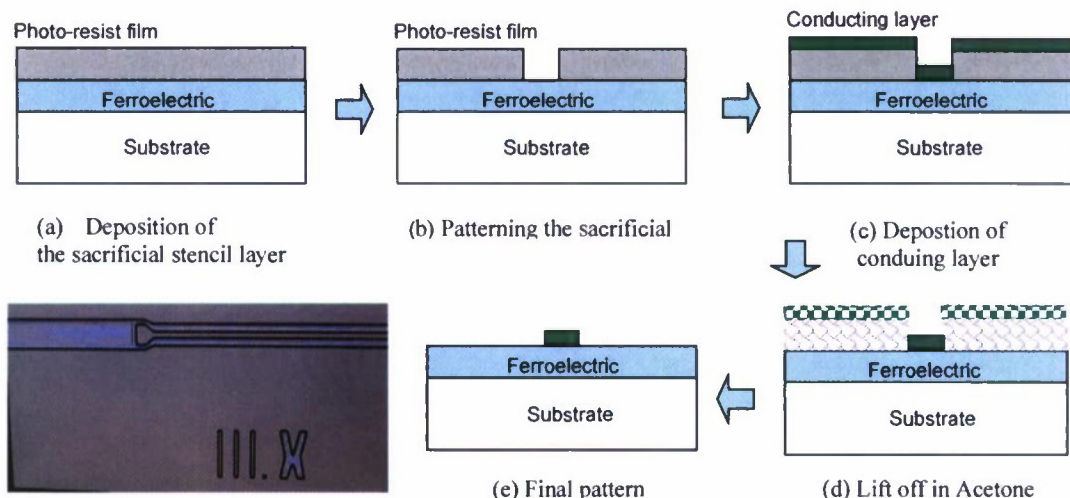
Figure 8. Procecure of the lift-off etching technique.

3.3 On-wafer probe station for measurement of phase shifter

RF performance and characterization of the ferroelectric CPW phase shifters were measured from 40 MHz to 20 GHz using on-wafer probe station (Cascade Microtech, Inc) connected to a vector network analyzer (Anritsu 3821). Figure 9 shows the on-wafer probe station and measurement setup with DC bias devices. Two bias tees were inserted between RF probes and VNA. DC power supply was connected into both bias tees to supply DC voltage, then this was applied between center conductor and ground. Full 2 port S-parameter measurements are

conducted directely on the wafer, vacuum-mounted on a Wafer Chuck. This on-wafer measurement device requires sophisticated calibration process to obtain accurate results. Impedance Standard Substrate (ISS) and an operating software (Wincal XE software), which is developed by Cascade Micorthech Inc, are used for the calibration of the probe and S-parameter measurements.
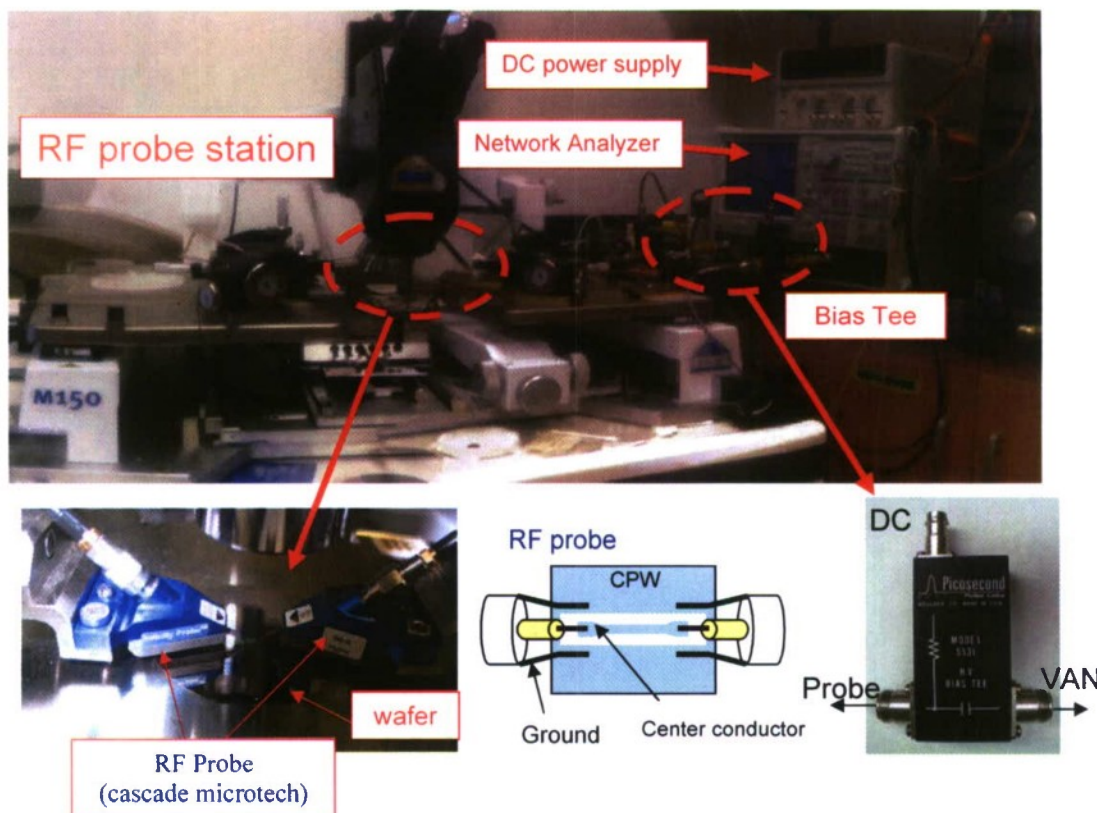


Figure 9. On-wafer probe station connected with a vector network analyzer and DC power supply.

4. Optimization of the sputtering parameters for BSTO deposition

During deposition of BSTO target on a substrate, sputtering parameters including the substrate temperature, oxygen gas flow, and chamber pressure play an important role to control the quality

19

of BSTO thin films. Thus, our first research goal was to find the optimal sputtering parameters for obtaining high quality of BSTO films. BSTO films were grown on $LaAlO_3$ substrates at different substrate temperatures and with different gas mixture ratios. X-ray diffraction (XRD) and Rutherford Backscattering Spectroscopy (RBS) tests were performed on these BSTO films to evaluate the quality of the BSTO films. XRD and RBS analysis was conducted by Arizona State University.

4.1 The first BSTO film sample

The first BSTO film was manufactured to calibrate the thickness sensor and to evaluate overall performance of the sputter system. $LaAlO_3$ wafer with 2 inch diameter was mounted on the heating block by using a clamp. BSTO film was grown with the sputtering parameters summarized in Table 1.

Table 1. Sputtering parameters for the first BSTO film sample.

Temp (°C)	700 (Heater)		Target	BSTO on LaAlO3 wafer
Gas mixture	Pure Ar - (5.0 ccm) and Ar/O_2 mixture (4:1) gas (5.0 ccm)		Pressure (mTorr)	50
Rotation (speed)	Fixed (0 %)		Thickness monitor reading	5 KÅ
Pre-sputter	30 min.@ 50W RF		RF power	250W

To characterize the BSTO film on $LaAlO_3$ substrate the RBS analysis was conducted and the results are shown in Figure 10. As one can see in Figure 10(a), the film is stoichiometric ($Ba_{0.5}Sr_{0.5}Ti_1O_3$) and its thickness is 1900 /cm2 which is equivalent to 2350 Å on the assumption that density of BSTO film is 5.62 g/cc). From this result, it is found that actual thickness of the BSTO film is half of the thickness monitor reading. In Figure 10(b), BSTO film does not show any channeling, which indicates absence of epitaxy in the film. To get epitaxy which is desirable for better properties, growth conditions (mainly growth temperature and pressure) should to be

changed systematically. It is known that window of growth temperature for the BSTO deposition is in the range of 700 – 850 °C.
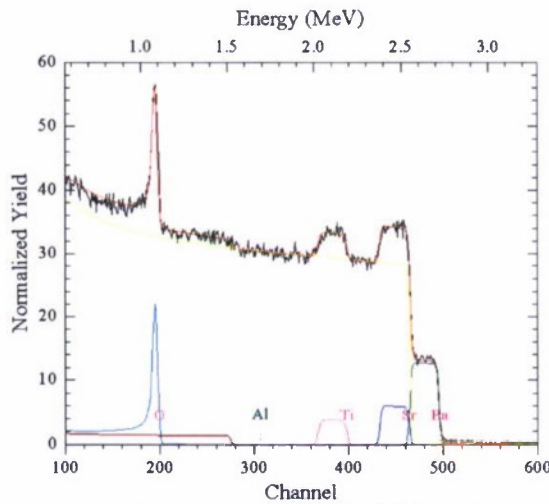
(a) Composition: Ba 0.5 Sr 0.5 Ti 1 O 3
Thickness: 1900 /cm2 (~2350 A, assuming density of BSTO as 5.62 g/cc)
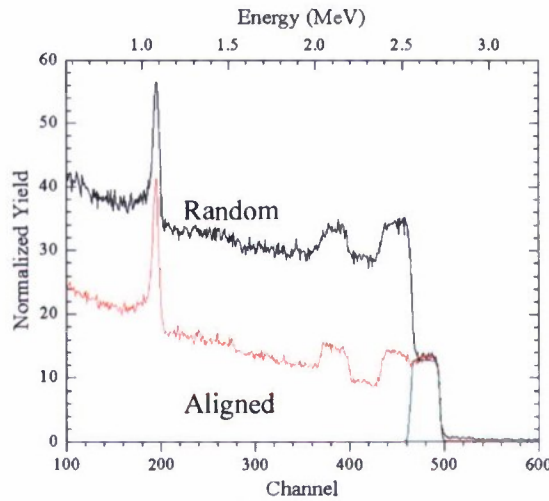
(b) No channeling observed in the film.

Figure 10. Rutherford Backscattering Spectroscopy (RBS) analysis of BSTO film on LaAlO₃.

Heater temperature of the first sample was 700 °C, which is on the lower end of this range. The actual substrate temperature might be lower than 700 °C due to imperfect thermal contact

21

between the substrate and the heater, since the substrate was fixed on the heater only by clamp. Therefore, we conclude to utilize a thermal transfer agent such as silver (Ag) paste between the substrate and the heater to ensure the substrate temperature is same as the temperature reading. We also decided to increase oxygen ratio to improve the epitaxial quality.

4.2 The second BSTO film samples

Based on lesson from the first analysis, the second set of BSTO film samples were manufactured. To ensure thermal contact, the silver paste was applied between the $LaAlO_3$ substrate and the heater. To improve the epitaxial quality of the BSTO, oxygen gas rate was increased. To investigate effects of the substrate temperature on the epitaxial quality, 3 individual BSTO films were deposited on $LaAlO_3$ at 700, 750, and 800 °C, respectively. Table 2 presents the sputtering parameters for the second set of BSTO film examples.

Table 2 Sputtering parameters for the second set of BSTO film samples.

Temp (°C)	700, 750, 800		Target	BSTO on LaAlO3 wafer
Gas mixture	Ar/O_2 mixture (4:1) gas (10.0 ccm)		Pressure (mTorr)	50
Rotation (speed)	Fixed (0 %)		Thickness monitor reading	5 KÅ
Pre-sputter	30 min.@ 50W RF		RF power	250W :

Figure 11 shows the RBS analysis for comparison of composition of films grown at 700, 750 and 800°C. As one can see, film composition is stable till 750°C and then falls apart, particularly for Ba and Sr, at 800°C. Film thickness at 700°C and 750°C is 2900 Å and drops to 2500 Å at 800°C. Since same growth times were applied for all the films, the growth rate appears to drop at 800°C. Based on these results, 700 – 750°C appears to be the right window for growth temperature of BSTO.
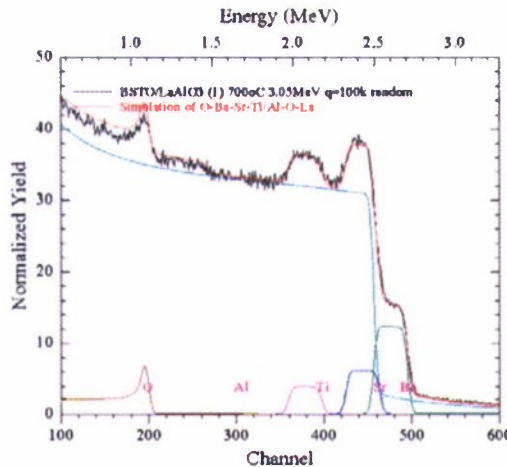
(a) Thickness: 2350 /cm^2 (2900 Å) : Ba$_{0.48}$Sr$_{0.52}$Ti$_1$O$_3$ on LaAlO3
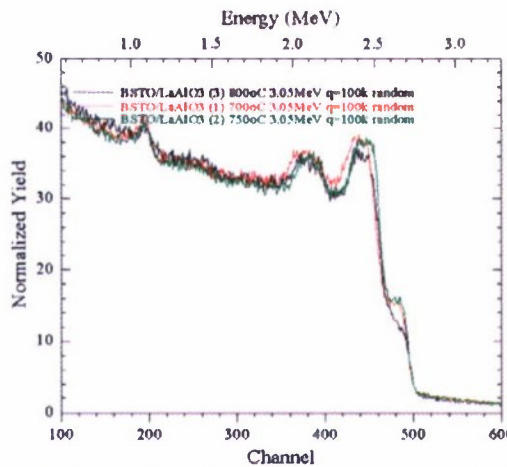
(b) Comparison of composition of films grown at 700, 750 and 800°C.

Figure 11. RBS analysis of the second set of BSTO films on LaAlO$_3$ for thickness and composition.

Figure 12 presents the RBS analysis results for comparison of epitaxy in films grown at 700, 750 and 800 °C. As can be seen in the figure, epitaxy of all the films is similar (Figure 12(a)), with a chi min value of around 15 % (Figure 12(b)). This shows a significant improvement in structural quality from the first film where no channeling was observed. Chi min for perfect epitaxy should be around 3%. Thus there is a scope for further improvement in structural quality

of the film. Since chi min did not change as a function of temperature in 700–800 $^{\circ}$C range, further improvement can be achieved by increasing growth pressure. Based on these results and analysis, we concluded to determine 750 °C as an optimal growth temperature for our RF sputter system. Ar/O2 mixture gas with ratio 4:1 and deposition pressure of 100 mTorr were chosen to achieve proper epitaxial films. Optimal sputtering parameters for BSTO film are summarized in Table 3.
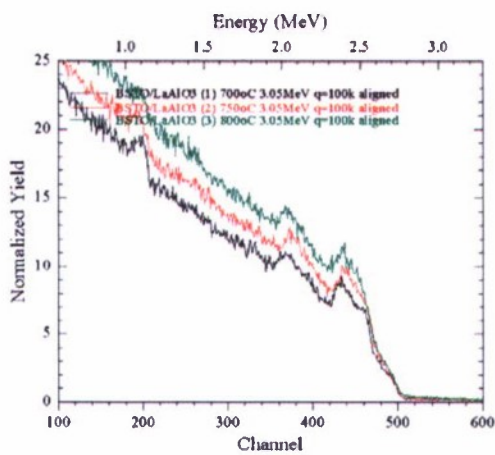
(a) Comparison of epitaxy in films grown at 700, 750 and 800°C.
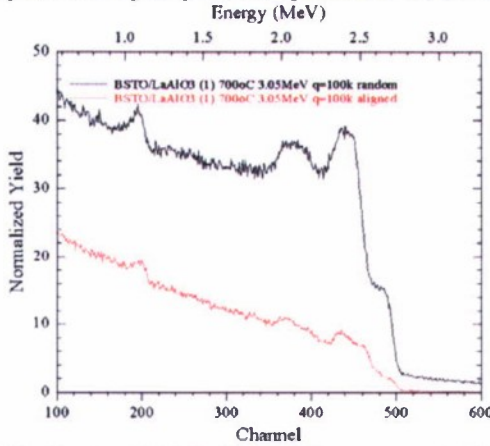
(b) chi min: 15 % for BSTO film grown at 700 °C.

Figure 12. RBS analysis of the second set of BSTO films on LaAlO$_3$ for epitaxy in films.

Table 3. Optimal sputtering parameters for the BSTO film deposition.

Temperature	750 °C
Gas mixture	Ar/O_2 (4:1) mixture gas (10.0 ccm)
Pressure	100 mTorr
RF power	250 W

5. Design, Fabrication, and measurement of the Coplanar waveguide (CPW) phase shifter.

In our previous research, behaviors of the CPW phase shifter which is fabricated on thin BSTO film were predicted by numerical simulation [8]. Furthermore, design curves for the ferroelectric CPW phase shifter, which provided guide lines for the trade offs involved in designing phase shifters on thin ferroelectric films, have been developed based on numerical simulation. Figure 13 plots the design curve of ferroelectric coplanar weave guide (CPW) phase shifter. This design curve, which was also constructed based on simulation results, shows variation of input impedance and insertion loss as a function of gap width and strip width. These simulated efforts have not been verified by experimental measurements. In this chapter, we fabricated several sets of ferroelectric CPW phase shifters to verify the simulation methods.


(a) Zo vs. Attenuation   (b) FOM vs. Phase Shift
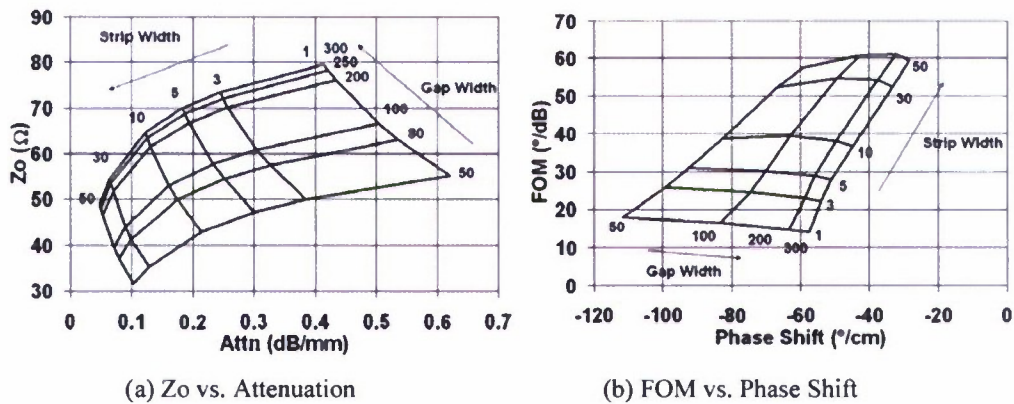
Figure 13. Design optimization curve for the CPW phase shifter as a function of strip width and gap width at 10 GHz.

25

5.1 Effects of the gap width and strip width

To investigate effects of the gap width and strip width on characteristics of the ferroelectric CPW phase shifter, 8 phase shifters were fabricated on BSTO film which was grown at LaAlO3 wafer with optimized sputter parameters discussed in previous chapter. Thickness of the BSTO film was 0.45 μm. After BSTO deposition, the film was metalized using the RF sputter system with 25 nm chrome (Cr) adhesion layer followed by a 1 μm thick cupper layer. The conductivity of Cr is $\sigma = 7.714$ MS/m and of Cu is $\sigma = 59.6$ MS/m. Then standard lift-off chemical etching techniques were used to fabricate the Cu/ BSTO/ substrate phase shifter. Figure 14 shows geometry of the ferroelectric CPW phase shifter. The conductor layer consists of the multi-metallization system of Cr/Cu (250 Å, 10 KÅ). Total lengths of the phase shifters was 3 mm. Each pahse shifter was designed to have different strip width (s) and gap width (g). Sizes of the gap and strip width of each phase shifter were tabulated in Table 4.
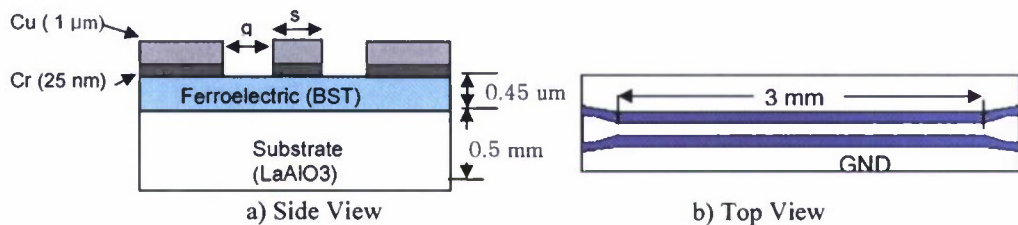
Figure 14. Layout and cross-section of the ferroelectric CPW phase shifter.

Table 4. Strip widths and Gap widths of 8 phase shifters

No.	Strip width (μm)	Gap width (μm)	No.	Strip width (μm)	Gap width (μm)
1	30	40	5	50	40
2	30	80	6	50	80
3	30	140	7	50	140
4	30	200	8	50	200

The Performance of these ferroelectric phase shifters at microwave frequencies was evaluated by measuring the transmission (S21) and reflection (S11) scattering parameters between 40 Mhz and 20 GHz using using on-wafer probe station (Cascade Microtech, Inc) connected to a vector network analyzer (Anritsu 3821).

Figure 15 shows the S-parameter measurement results for the CPW phase shifters. As one can see in Figure 15(a), insertion loss (attenuation) of the phase shifters decrease as the gap widths increase and the strip widths increase. It should be noted that the attenuation values in this plot were calculated based on corrected S_{21} (dB). S_{21corr} calculated from measured S_{21} as follows: $S_{21corr} = \sqrt{S_{21m}^2 /(1 - S_{11m}^2)}$, $S_{21coor} = 20 \log_{10}(S_{21coor})\,[dB]$, Attenuation = S_{21corr} / L [dB/mm], where L = 3 mm. S_{21corr} values are calculated to exclude mismatch losses, same as in simulations. Figure 15(b) presents phase shift of the CPW phase shifters. As one can see, phase shift also slightly were decreased as the gap and strip width increase. Input impedance of the phase shifters is proportional to the gap width while inversely proportional to the strip width as shown in Figure 15(c). Theses experimental results are in good agreement with those predicted by numerical simulation.

(a) Attenuation

(b) Phase shift

(c) Input impedance
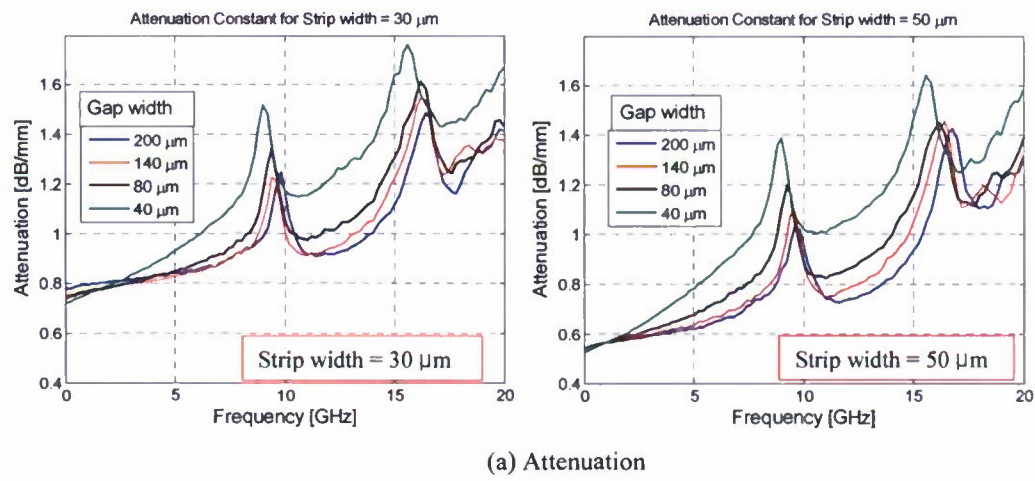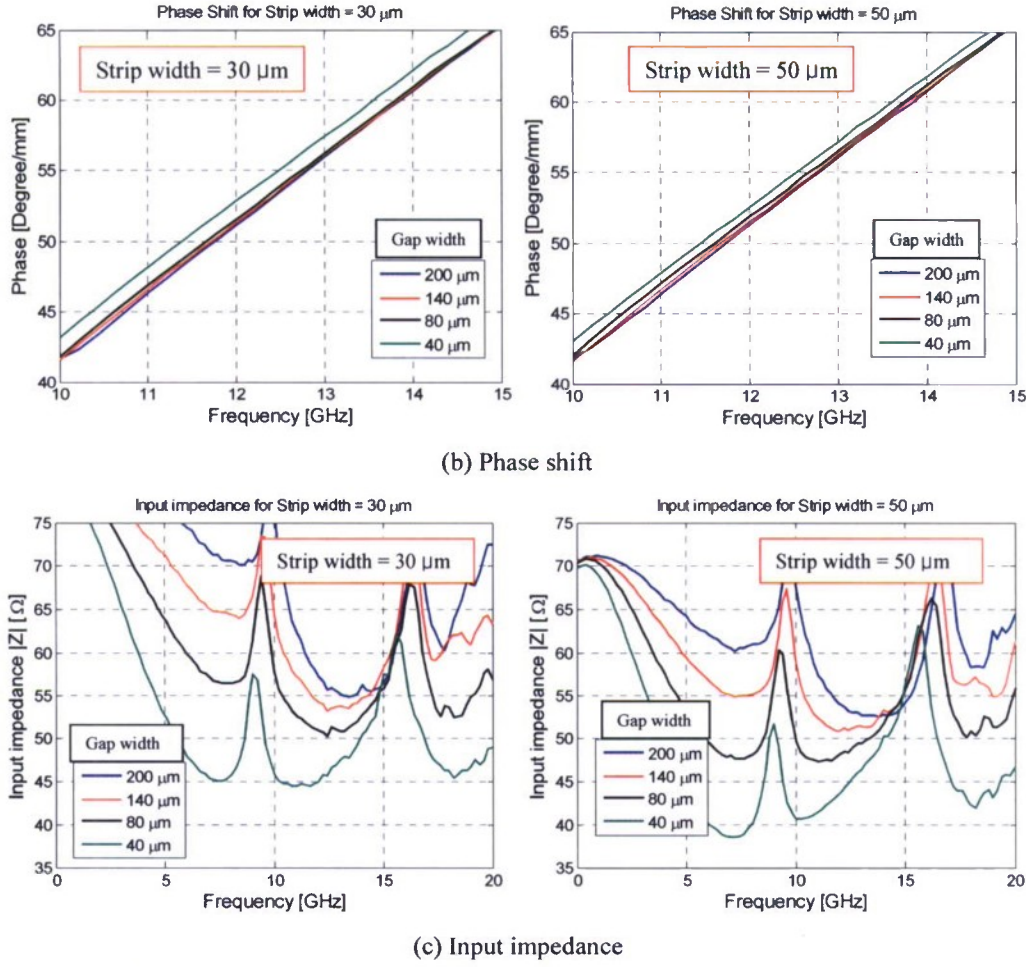
Figure 15. RF characteristics of CPW phase shifter as a function of the gap width and strip width.

5.2 Effects of thickness of BSTO film on RF characteristics of the CPW phase shifter

To exam effects of thickness of BSTO film on characteristics of the ferroelectric CPW phase shifter, three different thicknesses (0.5 μm, 0.75 μm and 1.75 μm) of BSTO films were deposited at separate LaAlO3 substrates, respectively. After BSTO deposition, the films were metalized using the RF sputter system with 25 nm chrome (Cr) adhesion layer followed by a 1 μm thick cupper layer. Standard lift-off chemical etching techniques were also utilized to fabricate the Cu/ BSTO/ substrate phase shifter. Total lengths of the phase shifters were 3 mm. From each wafer, a

phase shifter with strip width of 40 µm and gap width of 20 µm was chosen to compare its RF characteristics. Figure 16 presents measured S-parameter of the CPW phase shifter fabricated on three different thicknesses of BSTO films. As one can see in the S_{21} plot, increase in thickness of the BSTO layer results in significant attenuation increase, while the phase shift slightly increases. Thus simply increasing BSTO film thickness will not help to improve performance of the phase shifter. A smith chart in Figure 8 shows that thickness of the BSTO layer is also proportional to input impedance of the phase shifter due to high dielectric constant of the BSTO. Such trends which were observed from experimental measurement also agree with those from simulation.
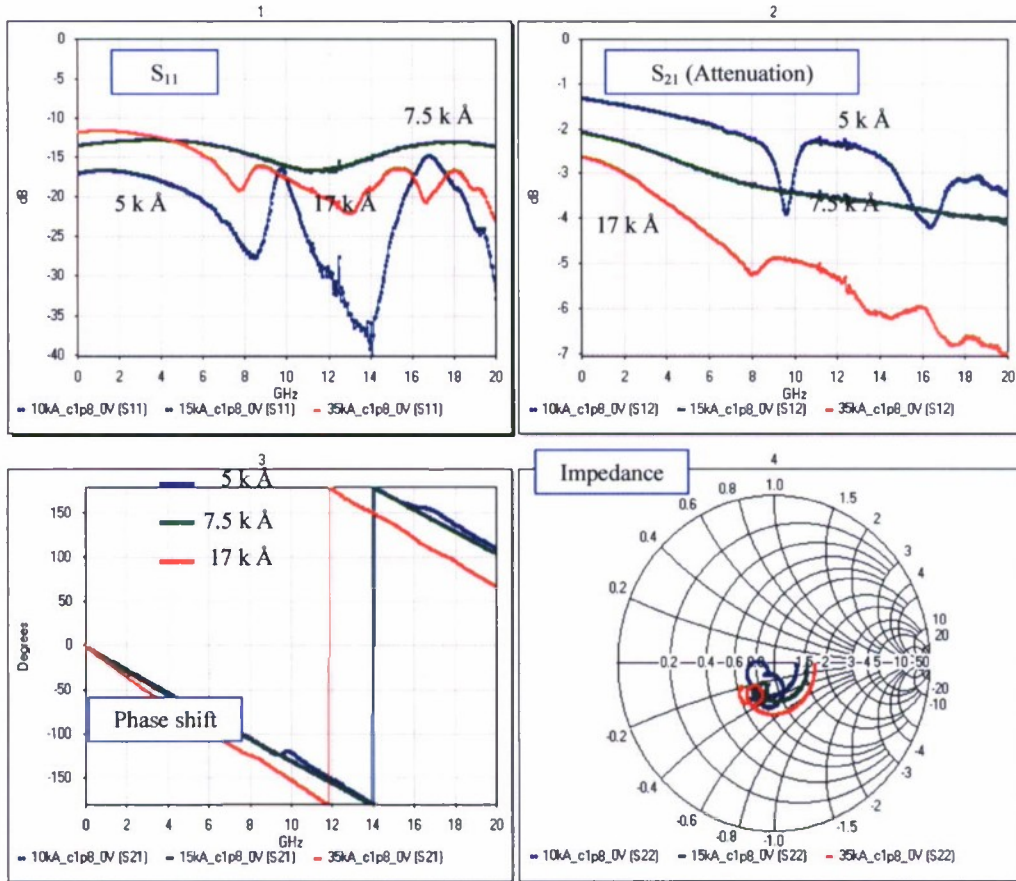

Figure 16. Measured S-parameter of the CPW phase shifter (gap witdth = 20 µm, strip width = 40 µm) fabricated on three different thicknesses of BSTO films.

5.3 Effects of different type of substrates

To investigate effects of different type of substrate, we proceeded to fabricate and test ferroelectric phase shifters on different types of substrates. For this study, we prepared three different types of substrates including MgO, LaAlO$_3$, and SrTiO$_3$ (STO). BSTO layer with 0.45 µm thickness was deposited on each substrate by using the optimized sputter parameters. The same size of CPW phase shifter, which have 30 µm of strip width and 80 µm of gap width, were fabricated on the BSTO layer of each substrate. Figure 17 shows the obtained experimental results for three types of substrates including MgO, LaAlO$_3$, and SrTiO$_3$. As it may be seen from Figure 17, the ferroelectric layer grown on STO substrate provides much larger phase change with DC bias voltage. This, however, came at the expense of much larger attenuation values compared with the MgO and the LaAlO$_3$ cases. This may be due to the fact that the ferroelectric layer in our measurements was too thin to fully utilize the tuning capability of BSTO, and having a substrate of complementary properties helped with overcoming the materials mismatch at the layers interface and hence achieved the significant increase in the amount phase shift with change in DC bias. It worth noting that dielectric constants for MgO, LaAlO$_3$, and SrTiO$_3$ are 9.8, 25, and 475 at 10 GHz in room temperature, respectively. Input impedances of the phase shifters were inversely proportional to dielectric constant of the three types of substrates (Mgo, LaAlO3, and STO). The significant reduction in the input impedance for the STO substrate case, which could be caused by high dielectric constant of the STO substrate, would cause an increase in current for a given applied DC bias voltage, and may hence have contributed to the overall increase in the attenuation values.

It is, however, of interest to compare these measured results with simulation data using the WIPL-D software. Figure 18, shows the comparison between simulated and measured date for the case of STO substrate, while Figure 19 shows data for the other two cases. It is very

30

encouraging to see such good agreement between measured and calculated values and besides providing confidence in the device fabrication and experimental characterization processes, the results also validate the accuracy of the modeling and simulation tools and their invaluable input into the design and optimization process.
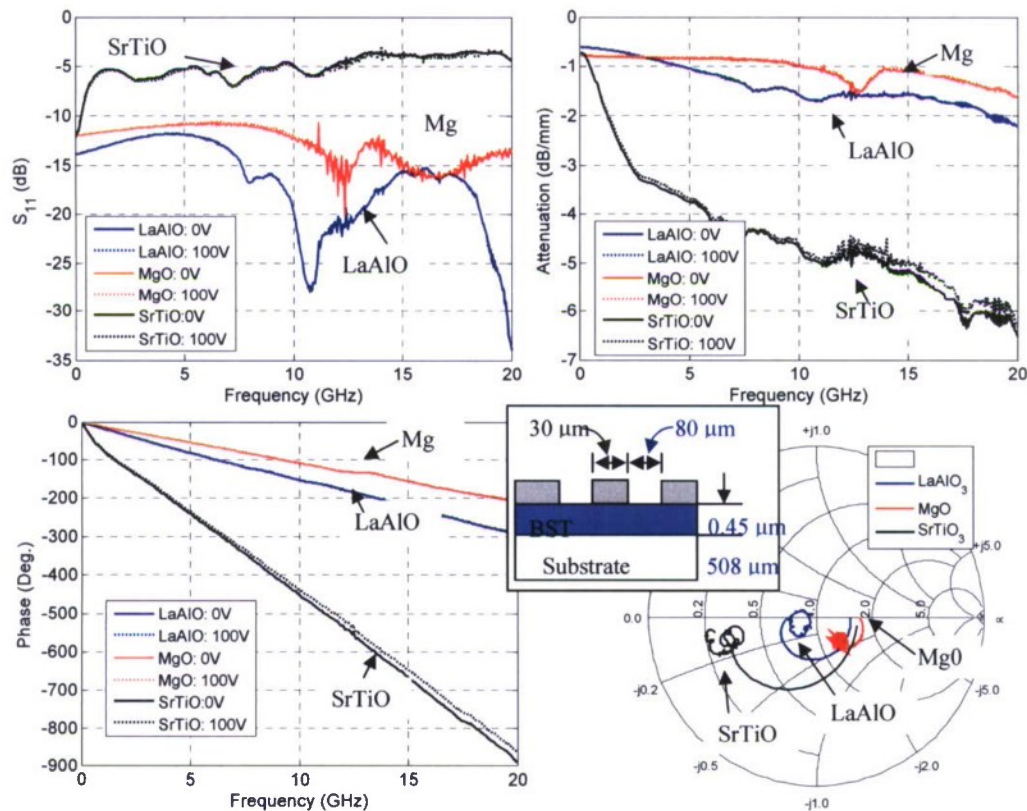
Figure 17. RF performance of phase shifters with different base substrates.
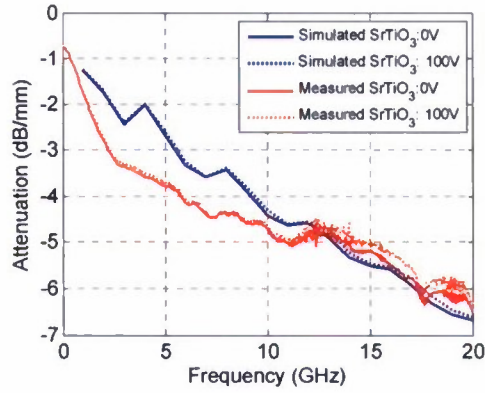
Figure 18. Simulated and Measured attenuation of SrTiO₃ based phase shifter for biased and unbiased cases.
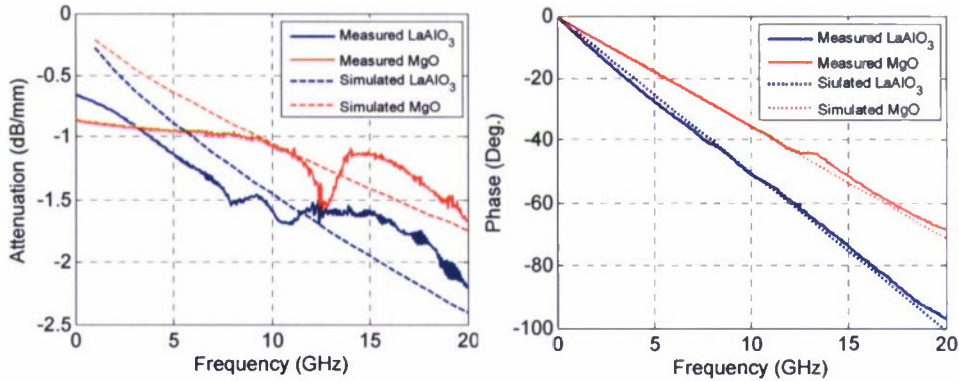
Figure 19. Comparison between simulation and measurement attenuation and phase for MgO and LaAlO₃

6. Conclusion and summary

In this report, we mainly focused on fabrication and experiments of the tunable ferroelectric phase shifter. Numerical simulation methods utilized in the preliminary studies were also verified with experimental results. During BSTO deposition process, sputtering parameters including the substrate temperature, oxygen gas flow, and chamber pressure determine the quality of BSTO thin films. Studies for optimizing the sputtering parameters were conducted to obtain high

quality of BSTO films. Optimal sputtering conditions for BSTO deposition were determined based on epitaxial qualities characterized by the RBS-channeling spectrometry. The optimized parameters were suggested in this report. Using the optimized sputtering parameters, various sets of BSTO films have been deposited with different thicknesses on different substrates and various size of CPW phase shifters have been fabricated on these substrates. The RF performances of the developed phase shifters were characterized from 40 MHz to 20 GHz by the on-wafer probe station and measurement results were compared with those from simulations using WIPL-D software. Good agreement was observed between simulations and measured results and this provides high confidence in the developed fabrication process. The comparison results also validate the accuracy of the modeling and simulation tools and their invaluable input into the design and optimization process. Based on these results, it is essential to further purse the studies of the innovative phased antenna array technology, fully develop fundamental understanding of its basic characteristics and establish a reliable process for prototyping various options of its designs. Multilayer approach, and a variety of designs of the phase shifter (straight, meander line, etc) are a good candidate to improve performance of the ferroelectric RF devices and need to be studied as a future work. For these studies, the fabrication effort will be significant and many challenges are expected to be faced along the way. The obtained results, however, will be unique and very important in leading the way towards the development of high performance low cost phased array antennas with beam steering capabilities.

References

[1] M. F. Iskander, Z. Zhang, Z. Yun, and R. Isom, "Coaxial Continuous Transverse Stub (CTS) Array." *IEEE Micro. Wireless. Lett.,* vol. 11, no. 12, pp. 489-491, Dec. 2001.

[2] R. Ison, M. Iskander, Z. Yun, and Z. Zhang, " Design and Development of Multiband Coaxial Continuous Transverse Stub (CTS) Antenna Arrays," IEEE Trans. on Antennas and propagation, vol. 52, no.8, pp. 2180-2184, Aug. 2004

[3] W. Kim, M.F. Iskander, "A new Coplanar Waveguide Continuous Transverse Stub (CPW-CTS) Antenna for Wireless Communications." *IEEE Ant.. & Prop. Lett.,* vol. 4, pp. 172-174, 2005.

[4] W. Kim and M. F. Iskander,"A new Coplanar Waveguide Continuous Transverse Stub (CWP-CTS) antenna for wireless communications," U.S. Patent 7,079,082, Jul. 18, 2006

[5] W. Kim, M. Iskander, and C. Tanaka, "High-performance Low-Cost Phase-Shifter Design Based on the Ferroelectric Materials Technology," Elelctronics Letters, Vol. 40, no. 21,pp. 1345-1347, Oct. 2004.

[6] W. Kim, M. Iskander, C. Krowne, "Modified Green's Function and Spectral-Domain Approach for Analyzing Anisotropic and Multidielectric Layer Coplanar Waveguide Ferroelectric Phase Shifters,*" EEE Transactions on Microwave Theory and Techniques,"*vol. 55, pp. 402-409, 2007

[7] W. Kim, M. Iskander, "Novel High performance Low Cost Phase-Shifter Design Based on the Ferroelectric Materials Technology Using the WIPL-D Code," Applided Computational Elelctromagnetics Society, Syracuse, NY, 2004.

[8] W. Kim and M. Iskander, "Integrated Phased Array Antenna Design Using Ferroelectric Materials and the Continuous Transverse Stub Technology," IEEE Trans. on Antennas and propagation, vol. 54, no. 11, pp. 3095-3105, 2006

[9] F. W. Van Keuls, C. H. Mueller, F. A. Miranda, R. R. Romanofsky, C. L. Canedy, S. Aggarwal, T. Venkatesan, R. Ramesh, J. S. Horwitz, W. Change, and W. J. Kim, "Room temperature thin film BaxSr1-xTiO3 Ku- band coupled microstrip phase shifters: Effects of film thickness, doping, annealing and substrate choice," in *IEEE MTT-S Int. Microwave Symp.* Vol. 2, pp. 737-740, Jun. 1999.

[10] S.W. Kirchoeferm J. M. Pond, H. S. Newman, W. J. Kim and J. S. Horwitz, "Ferroelectric/ferrite tunable phase shifters," in IEEE MTT-S Int. Microwave Symp. Vol. pp. 1359-1362, Jun. 2000.

[11] C. M. Krowne, S. W. Kirchofer, J. M. Pond, "Anisotropic Permittivity and Attenuation Extraction From Propagation Constant Measurements Using an Anisotropic Full-Wave Green's Fuction Solver for Coplanar Ferroelectric Thin-Film Devices," *IEEE Trans. MTT.* Vol. 50, pp. 537-548, Feb. 2002.

[12] C. Krowne, "Fourier transformed matrix method of finding propagation characteristics of complex anisotropic layered media: Application to Isotropic and Anisotropic Substrates," IEEE trans. On Microwave theory and techniques, vol. 35, no 12, pp. 1399-1407, Dec 1987

[13] G.L. Matthaei, K. Kiziloglu, N. Dagli, and S. Long, "The nature of the charges, currents, and fields in and about conductors having cross-sectional dimensions of the order of a skin depth," IEEE trans. On Microwave Theory and Techniques, vol. 38, no. 8, pp. 1031-1036, Aug. 1990

[14] E. Carlsson and S. Gevorgian, "Effect of enhanced current crowding in a CPW with a thin ferroelectric film," *Electronic Letters*, vol. 33, no. 2, pp. 145-146, 1997

Appendix A

Copies of Published Work

Coaxial Continuous Transverse Stub (CTS) Array

Magdy F. Iskander, *Fellow, IEEE*, Zhijun Zhang, *Member, IEEE*, Zhengqing Yun, *Member, IEEE*, and
Robert Isom, *Student Member, IEEE*

Abstract—A new coaxial continuous transverse stub (CTS)
array is proposed, designed, constructed, and tested. It is an
omni-directional low cost antenna array which provides good
impedance matching characteristics and good tolerance to manu-
facturing errors. It can be simply fed by a coaxial connector and is
particularly suitable for millimeter wave personal communication
systems (PCS). It is shown that this type of radiating element pro-
vides high percentage of radiation, and for the simulated design
of single- and multiple-element arrays, S_{11} was below -10 dB
across a 6 GHz frequency span at the Ka band. A three-element
prototype Coaxial CTS antenna array was designed, constructed,
and tested in the X-band. Experimental results were in good
agreement with the simulated performance. Potential application
of this new antenna array in multiband operation is also described.

Fig. 1.   Coaxial CTS array segment with two elements.

I. INTRODUCTION

THE planar CTS was originally invented at Hughes Aircraft
Company in 1991. It represents a unique class of low-cost
antenna array, exploiting the low-loss, low-dispersion, dimen-
sional robustness, and design flexibility of an open parallel-plate
structure as both its transmission line and radiator bases [1]–[3].

The coaxial Continuous Transverse Stub array described in
this paper, however, provides an alternative design that may pro-
vide additional advantages in feeding, impedance matching, and
radiation characteristics [4]. It consists of a coaxial structure
as its transmission line feed and parallel plate subs as the ra-
diating elements. The difference between the coaxial CTS and
the planar version is their array structure in the form of an-
nular or sectoral stubs and the resulting omnidirectional radia-
tion pattern. As in the case of planar CTS, beam steering may be
achieved mechanically or by using Ferroelectric materials [4],
[5].

II. COAXIAL CTS DESIGN

Fig. 1 shows a two-element coaxial stub CTS antenna array,
where it may be seen that it consists of a cascaded section of
standard coaxial transmission lines and open-ended coaxial ra-
diating stubs. Similar to the planar CTS case, short-circuited
stubs may also be used and the coaxial CTS arrangement may
be used as a filter in this case.

Design procedures for a coaxial CTS array include the deter-
mination of the following parameters: (1) width of stub segment
$L1$; (2) length of transmission line segment $L2$; (3) dielectric
constant of filler dielectric material: ε_r; (4) diameter of inner
conductor $D1$; (5) diameter of outer conductor $D2$; and (6) di-
ameter of stub $D3$.

For the purpose of an illustrative design, the width of stub
segment $L1$ was selected to be a half wavelength in dielectric
material that fills the stub. The length of the transmission line
segment $L2$ and dielectric constant of dielectric material ε_r can
be chosen to fulfill distance and phase demands between stubs.
The diameters of the inner and outer conductors $D1$ and $D2$ of
the coaxial transmission line can be adjusted to form the desired
value of impedance, such as 50 Ω or 75 Ω in the case of a coaxial
transmission line. The ratio between $D3$ and $D2$ determines the
radiation pattern, voltage across, and the radiated power from
each stub. Small values of $D3/D2$ tend to lead to increased
radiation, but more care must be taken to achieve impedance
matching. Also, $D3$ must be chosen so as to limit the level of
mutual coupling between the stub elements in the Coaxial CTS
array. Control of mutual coupling between elements in the array
can be generally achieved by meeting the condition $D3 > L1$.

Clearly, the diameters of the inner and outer conductors $D1$
and $D2$ do not need to be uniform along the transmission line.
Instead, they can be changed periodically to adjust the matching
and phase relationship between elements. Actually, the coaxial
CTS is an excellent self-matching structure. By properly con-
trolling the ratio of $D3$ and $D2$ and the ratio of $D3$ and $L1$,
it is possible to achieve low reflection stub elements. As one
might expect, the design parameters $D2, D3, L1$, and $L2$ im-
pact various aspects of the characteristics of the array including
impedance matching (S_{11}), percentage of power radiated out,
and radiation pattern. Detailed design curves will be developed
and reported in a separate publication.

III. SIMULATION RESULTS

Three different (three dimensional) 3-D electromagnetic
simulation software packages (IE3D®, HFSS, and in-house
FDTD codes) were used to simulate Coaxial CTS antenna
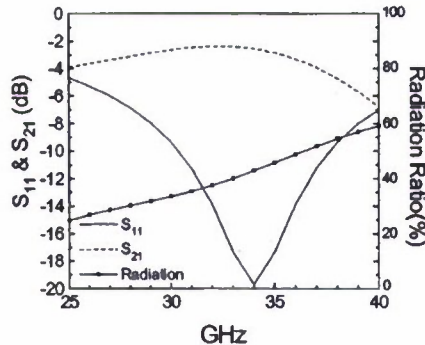
Fig. 2. S_{11}, S_{21}, and radiation of Coaxial CTS segment.

Fig. 3.   Radiation patterns of single stub (dashed line) and a Coaxial CTS array (solid line).

Fig. 4.   Multiband CTS antenna array.

Fig. 5. S_{11} and S_{21} of transmission stub. At 4 GHz, $S_{11} < -19$ dB, $S_{21} = -0.24$ dB, $D1 = 1$ mm, $D2 = 2.3$ mm, $D3 = 20$ mm, $L1 = 5$ mm.

array structures. Fig. 2 shows the reflection S_{11} and coupling S_{21} of a one-element Coaxial CTS antenna. The coaxial fill material is air, $\varepsilon_r = 1$, $D1 = 1$ mm, $D2 = 2.3$ mm, $D3 = 10$ mm, $L1 = 5$ mm. The impedance of the air filled coaxial transmission line segment ($D2/D1 = 2.3$) is 50 Ω. As may be seen from Fig. 2, the bandwidth of $S_{11} < -10$ dB is more than 6 GHz. In this bandwidth, the radiation power ratio [(Total Power $-$ Reflected Power $-$ Transferred Power)/(Total Power) $* 100\%$] from the single stub is more than 30%, which supports the claim of a highly radiating structure. In the above equation, the total power was considered to include radiated power and the "transferred power" term represents the amount of power coupled to the load (end of the array). The numerator in the equation therefore quantifies the amount of radiated power from one specific stub.

Similar to the case of the planar CTS array, the coaxial CTS array is a traveling-wave-type array; so the farther the stub is from the array input port the less power it will receive. This aspect of the array design may be adjusted depending on the location of each stub and the dimension of the stubs' lengths and widths dimensions. If the array was designed such that each stub radiates a larger amount of power, then the array will effectively include a reduced number of stubs and the array will be used as a low gain antenna. On the other hand, if each stub was designed to radiate less power, more stubs can be used and a high gain antenna array may be designed.

The radiation pattern was calculated at the frequency of minimum S_{11} (34 GHz) and was found to be split at broadside. Although this may be explained in terms of the excessively wide electrical width of the stub at this frequency ($L1/\lambda = 0.57$), it is often desirable to achieve a radiation pattern with single main lobe. This was found to be possible to achieve at the slightly lower frequency of 30 GHz, which is still within the same operating frequency band of the array ($S_{11} < -9$ dB).

The radiation pattern at 30 GHz is shown in Fig. 3. The dotted line in Fig. 3 shows the radiation pattern of a one coaxial CTS stub segment with the same dimension and design parameters as described above. The solid line in Fig. 3 shows the radiation pattern at 30 GHz of a Coaxial CTS array formed by eight-stub elements. Here, $L2 = 3$ mm and it fulfills the demand of co-phase between stubs. Each stub radiates 33% power; hence, neglecting the mutual coupling effects, eight elements will be needed to radiate more than 95% of the incident power at a rate of 33% radiation from each stub.
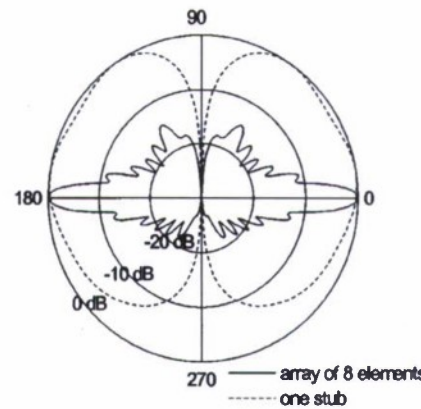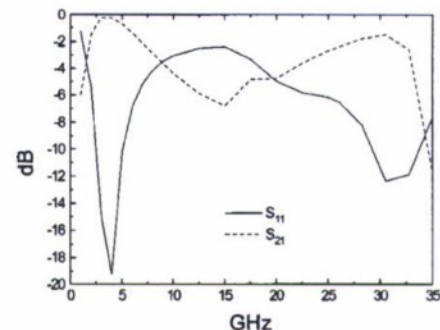
It is also of interest to examine the potential operation of such an array structure at multiband frequency ranges. A design that includes efficient radiators at higher frequencies near the antenna feed, and relatively lower frequency radiating stubs at the end, is shown in Fig. 4. To help examine the feasibility of this procedure two coaxial stubs were designed. The first is a high frequency radiating stub and is expected to exhibit a virtual short at the stub-coaxial line junction at the lower operating frequency. This means that the high frequency stubs will provide good transmission along the main coaxial line at the lower operating frequency. The design and the calculated S-parameters for this design is shown in Fig. 5. As it may be seen, almost perfect transmission and low reflection ($S_{11} = -19$ dB) were possible to achieve at 4 GHz. Fig. 5 also shows that this high frequency stub would radiate 29% of the power at 30 GHz. Alternatively, the stub dimension may be designed so as to enhance radiation at a lower frequency band. Such a design was simulated and the S-parameters results are shown in Fig. 6. Each stub can radiation 17% power at 4 GHz. Clearly combining these designs in a
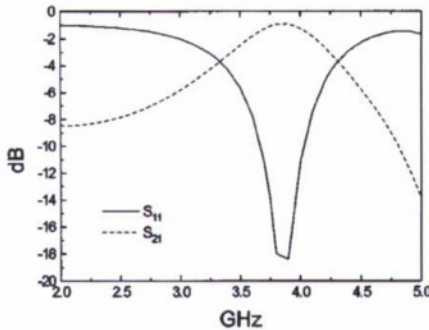
Fig. 6. S_{11} and S_{21} of radiation stub. At 4 GHz, $S_{11} < -11$ dB, $S_{21} = -1.24$ dB. $D1 = 1$ mm, $D2 = 2.3$ mm, $D3 = 90$ mm, $L1 = 40$ mm.
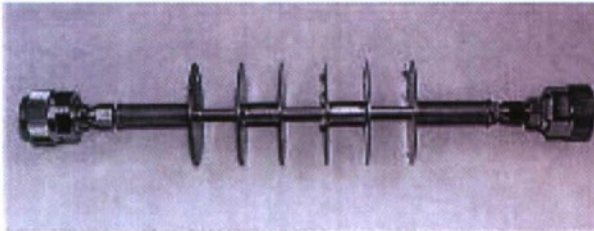
Fig. 7. Photograph of the prototype X-band three-element Coaxial CTS array.

single array will achieve the proposed multiband operation at 4 GHz and 30 GHz. This design may be varied and other possible frequency bands may be achieved.

IV. EXPERIMENTAL VERIFICATION

It is critically important to verify the simulation results of the Coaxial CTS design with experimental measurements. For this reason, a three-element X-band Coaxial CTS antenna array was designed, fabricated, and tested at the University of Utah. A picture of the three-element array is shown in Fig. 7. The simulation was performed using an FDTD code and the design specifications are given as follows: $L1 = 18$ mm, $L2 = 17$ mm, $D1 = 3$ mm, $D2 = 6.9$ mm, $D3 = 40$ mm, and $\varepsilon_r = 1$. Nylon rings that were between the inner and outer conductors of the coaxial feed line for support were included in the FDTD model. This initial design was not synthesized for a particular radiation pattern with the simulation data, but instead for instead for S-parameter measurements and comparison.

S-parameter measurements of the three-element X-band coaxial CTS antenna array were taken using an HP-8510B Network Analyzer. The obtained experimental results (solid line) are shown in Fig. 8, together with the simulated data (solid line with $+$s). As may be seen from Fig. 8, excellent agreement may be observed, particularly in the operating frequency band of the array in the range from 9.2–10.3 GHz. One may also observe a sharp dip in the measured S_{21} curve at about 10.2 GHz. This was attributed to the presence of a discontinuity in the junction at one of the end connectors. Much improvement was realized when the connectors were soldered to the antenna, but some discontinuity effects may be still be seen in Fig. 8.
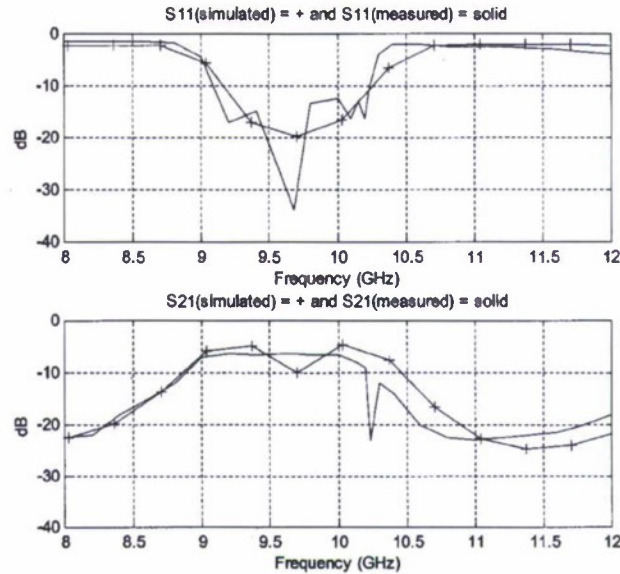
Fig. 8. Measured and calculated S-parameters of the prototype X-band three-element array.

V. CONCLUSION

A New Coaxial CTS antenna array design was proposed. Unlike the planar CTS arrays, it provides significant impedance matching advantage and an omni-directional radiation pattern. Furthermore, by adjusting the dimensions of the center and outer conductors along the coaxial transmission line, significant impedance matching advantage may be achieved. The proposed low-cost coaxial CTS antenna array provides an excellent potential design for base stations for wireless communication systems at millimeter waves (LMDS). The potential use of this antenna array in multiband operation was also discussed.

Verification of the simulated results was obtained through simulating, building, and testing a three-element X-band Coaxial CTS antenna array. Good agreement was obtained between measured and simulated results from 8–12 GHz. Future work will include building and testing of a multiband design, the design of dielectrically loaded Coaxial CTS structures, and the use of ferroelectric materials to realize one-dimensional beamsteering [5].

REFERENCES

[1] W. W. Milroy, "Continuous transverse stub element devices for flat plate antenna arrays," U.S. Patent 5 488 248.
[2] V. P. Matterer, "Phase tuning technique for a continuous transverse stub antenna arrays," U.S. Patent 5 604 505.
[3] R.-S. Chu, "Analysis of continuous transverse stub (CTS) array by floquet mode method," presented at the *1998 IEEE Int. Antennas Propagat. Symp. USNC/URSI Nat. Radio Sci. Meeting*, vol. 2, Atlanta, GA, June 21–26, 1998.
[4] Z. Zhang, M. Iskander, and Z. Yun, "Coaxial continuous transverse stub element device antenna array and filter," U.S. Patent 6 201 509.
[5] M. Iskander, Z. Zhang, and Z. Yun, "Low cost low losses antenna array with beam steering capability," U.S. Patent Application.
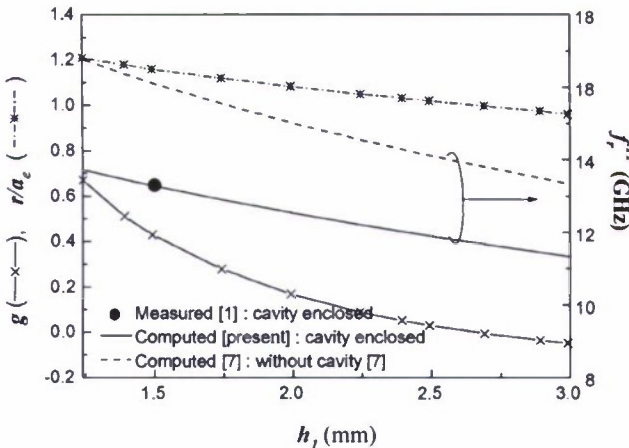
Fig. 3. Resonant frequency of IMCP antenna with and without cavity enclosure and corresponding cavity factors g and r/a_e versus h_1. $r = 6.35$ mm, $h_2 = 1.524$ mm, $\varepsilon_r = 2.3$, $a = 4.0$ mm

for comparison. The increase in h_1 causes decrease in both r/a_e and g values revealing the increasing cavity-effect on the IMCP. The resonant frequency also decreases with the increase in h_1 for both cavity enclosed and open type IMCPs. However, the effect of the cavity enclosure in diminishing the resonant frequency is significant over a considerable range of h_1 values, particularly at the lower values of h_1. Only a single measured value is available [1] to compare with the theoretical curve in Fig. 3 and this value shown by a solid circle corresponds to $g < 0.5$. Excellent agreement between the experiment and the present theory is also revealed.

The present studies show that a cavity enclosure influences the resonance of an IMCP under limited conditions resulting in lower resonant frequency. However, its effect on the radiation characteristics of an IMCP is not significant to that extent as reported in [1]. Uniform radiation patterns with acceptable cross polarization level and 6.65 dBi gain were reported [1] from the measurements of a typical cavity enclosed probe fed IMCP antenna.

IV. CONCLUSION

The inverted microstrip patches in open or cavity enclosed configuration are attractive for integrating with active devices below it. The change in resonance condition under the influence of a cylindrical cavity enclosing an IMCP has been thoroughly investigated both theoretically and experimentally. If different patches are examined in a same cylindrical enclosure, all are not affected by the cavity and a factor determining that dependence has been examined with the help of the new and previous data. A simple analytical formulation is proposed to predict the resonant frequency of cavity enclosed patches so far those are under the influence of the cavity. The theory is compared with different measurements resulting in very close approximation between them. The studies in this paper thus should guide a designer in choosing proper cavity and IMCP dimensions for a specified frequency within approximately 0.5% accuracy.

ACKNOWLEDGMENT

The authors would like to thank Dr. P. K. Saha and Dr. P. K. Basu of the University of Calcutta for their interest in the work and constant encouragement.

REFERENCES

[1] J. A. Navarro, L. Fan, and K. Chang, "Active inverted stripline circular patch antennas for spatial power combining," *IEEE Trans Microwave Theory Tech.*, vol. 41, pp. 1856–1863, Oct. 1993.
[2] ——, "Novel FET integrated inverted stripline patch," *Electron. Lett.*, vol. 30, no. 8, pp. 655–657, 1994.
[3] R. A. Flynt, L. Fan, J. A. Navarro, and K. Chang, "Low cost and compact active integrated antenna transceiver for system applications," *IEEE Trans. Microwave Theory Tech.*, vol. 44, pp. 1642–1649, Oct. 1996.
[4] C. M. Montiel, L. Fan, and K. Chang, "A novel active antenna with self-mixing and wideband varactor-tuning capabilities for communication and vehicle identification applications," *IEEE Trans Microwave Theory Tech.*, vol. 44, pp. 2421–2430, Dec. 1996.
[5] J. A. Navarro and K. Chang, "Active microstrip antenna," in *Advances in Microstrip and Printed Antennas*, K. F. Lee and W. Chen, Eds. New York: Wiley, 1997, ch. 8.
[6] J. A. Navarro, J. McSpadden, and K. Chang, "Experimental study of inverted microstrip for integrated antennas applications," in *IEEE Antennas Propagat. Int. Symp. Proc.*, Seattle, WA, 1994, pp. 920–923.
[7] D. Guha and J. Y. Siddiqui, "A new CAD model to calculate the resonant frequency of inverted microstrip circular patch antenna," *Microwave Opt. Technol. Lett.*, vol. 35, no. 6, Dec. 20, 2002.
[8] C. A. Balanis, *Advanced Engineering Electromagnetics*. New York: Wiley, 1989, ch. 9.
[9] I. Wolff and N. Knoppik, "Rectangular and circular microstrip disk capacitors and resonators," *IEEE Trans Microwave Theory Tech*, vol. 22, pp. 857–864, Oct. 1974.
[10] D. Guha, "Resonant frequency of circular microstrip antennas with and without air gaps," *IEEE Trans. Antennas Propaga.*, vol. 49, pp. 55–59, Jan. 2001.

Design and Development of Multiband Coaxial Continuous Transverse Stub (CTS) Antenna Arrays

Robert Isom, Magdy F. Iskander, Zhengqing Yun, and Zhijun Zhang

Abstract—Continuous transverse stub (CTS) technology has been adapted to use with coaxial lines to produce effective microwave antenna structures that radiate omnidirectionally, with high efficiency, low reflection, and useful radiation patterns. In this paper, we describe the design, construction, and testing of a new type of antenna arrays, that is, a six-element multiband (4.2 and 19.4 GHz) CTS antenna array. The design of the CTS array was optimized through simulation using finite-difference time-domain and then built and tested using both S-parameters and radiation pattern measurements. Simulation results agreed very well with measured data. These simple and low cost coaxial CTS structures could be adapted for base station applications in wireless communication, for satellite communication systems, and Identification Friend-or-Foe systems for the military.

Index Terms—Antenna array, coaxial continuous transverse stub (CTS), continuous transverse stub (CTS), multiband array.

I. INTRODUCTION

Continuous transverse stub (CTS) technology developed in the early 1990s at Hughes Aircraft Company [1] has attracted research attentions recently [2], [3]. This technology offers advantages over traditional approaches to antenna design at microwave frequencies. Benefits of CTS
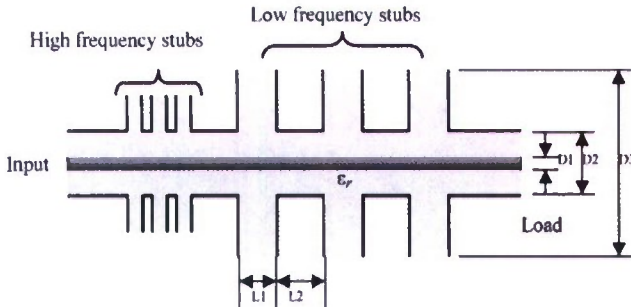
Fig. 1. Schematic of a six-element multiband coaxial CTS antenna array. First set of stubs from input are high-frequency stubs. Second set of stubs from input are low-frequency stubs.

Fig. 2. Photograph of fabricated multiband six-element coaxial CTS antenna array designed to operate at 4.2 and 19.4 GHz: angled view.

structures include compact size, lightweight, low loss, and high directivity. Parallel-plate CTS arrays have achieved average gains of 39.7 dB over a handwidth of 37–40 GHz [2]. This high gain is achieved along with relative dimensional insensitivity, thus reducing fabrication costs.

CTS technology also offers greater tunable bandwidth than waveguide or patch antennas, higher efficiencies, and polarization isolation of 25–50 dB. It is desired to apply the advantages of the presently available planar CTS technology to a new design that incorporates coaxial geometries. Such a process has been successfully implemented and some of the obtained results for a new coaxial CTS antenna were reported elsewhere [4], [5].

Coaxial CTS structures offer several additional advantages over planar CTS. They provide an omni-directional radiation pattern in the plane of the radiating stubs (perpendicular to the transmission line) as there is no azimuthal dependence in the designed cylindrical stubs. Secondly, coaxial structures are inherently easier to impedance match, thus providing higher efficiency and facilitate system integration with other coaxial structures.

In this paper, a two-band coaxial CTS is designed by simulating different structures using the two-dimensional finite-difference time-domain (2-D-FDTD) code. A prototype antenna is then constructed and tested. The measured S-parameters and radiation patterns agree well with the simulated results.

II. COAXIAL CTS DESIGN PROCEDURE

Design procedures for a coaxial CTS array include choosing the following parameters for both of the high- and low-frequency sections (see Fig. 1): 1) width of stub segment: L1; 2) length of transmission line between stubs: L2; 3) dielectric constant of fill material: ε_r; 4) diameter of inner conductor: D1; 5) diameter of outer conductor: D2; and 6) diameter of radial stub: D3. To help characterize the antenna performance as we vary some or all of these design parameters, a 2-D axially symmetric cylindrical FDTD code was used to simulate the performance and characterize the many tradeoffs involved in the design of these antennas. For the arrays we designed in this paper, we first designed two separated three-element arrays one at the lower frequency (4.2 GHz) while the other was designed at 19.4 GHz. The two sections were then joined and the entire six-element array was optimized to achieve the desired S-parameters and radiation pattern characteristics. The design of each of the two sections follows a procedure similar to that described in an earlier paper [5], and the discussion in this paper will focus on the design of the six-element multiband array.

III. DESIGN OF A MULTIBAND COAXIAL CTS ANTENNA ARRAY

The multiband array is a six-element coaxial CTS array with three elements designed to operate at 4.2 GHz and the other three elements at
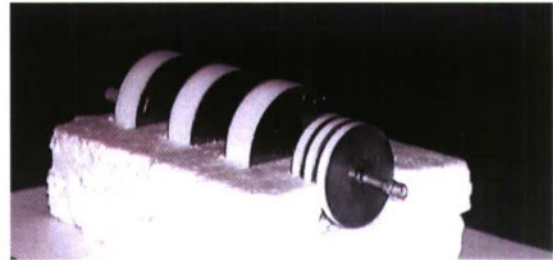
19.4 GHz. This array was designed to provide low reflection, high-radiation efficiency, and a broadside radiation pattern at two frequencies, 4.2 GHz (C-band) and 19.4 GHz (K-band). In designing this array, we used dielectric loading (Teflon and polyethylene) to improve the performance and reduce the overall size of the array.

As mentioned earlier, two sets of stubs were designed: one that was nonradiating (full transmission) at lower frequencies and radiates effectively at higher frequencies (high-frequency stubs), and a second set of stubs that radiate at the lower frequency (low-frequency stubs). The two sets need to be arranged in tandem with the high-frequency stubs near the input. This way, high-frequency signals would radiate from the high-frequency stubs before reaching the low-frequency stubs at the end, and the low-frequency signal, on the other hand, would efficiently pass through the high-frequency stubs connected to the input, and the input low-frequency signal will radiate when reaching the low-frequency stubs at the end of the array.

To accomplish this, it was necessary to know the electrical dimensions that would produce full transmission for the high-frequency stubs at the lower frequency. For this purpose, structures with narrow gaps and long stub diameters were simulated. It was found that narrow gap ($\ll \lambda$) stubs with a stub diameter of approximately $\lambda/3$ (12 mm at 8 GHz) or longer will produce close to full transmission at the lower frequencies. At higher frequencies, however, the same physical dimensions of the stubs were found to radiate efficiently. It is therefore possible to design a coaxial CTS structure that produces efficient radiation at a high frequency and appears almost transparent at lower frequencies.

Using this approach, we simulated a coaxial CTS array with multiband performance. The designed array was dielectrically loaded with Teflon and polyethylene to help improve impedance matching and reduce the size. Further performance enhancements for the multiband array were achieved by controlling design parameters such as the stub gap, stub height, and stub spacing of both the high-and low-frequency stubs. The entire multiband array was further optimized to account for the mutual coupling effects.

Following a manual optimization using inhouse FDTD codes [5], a multiband coaxial CTS antenna array design was achieved that produced low reflection and good radiation characteristics at both the upper and lower frequency bands. The dimensions of the high-frequency stubs were L1 = 5.2 mm, L2 = 3.8 mm, D1 = 1.12 mm, D2 = 3.6 mm, and D3 = 44.4 mm. The dimensions of the low-frequency stubs were L1 = 18.9 mm, L2 = 29.6 mm, D1 = 1.12 mm, D2 = 3.6 mm, and D3 = 61.2 mm. The spacing between the last high-frequency stub and the first low-frequency stub in the tandem connection of the two arrays was 21.6 mm. The radial waveguide stubs were dielectrically loaded with Teflon rings. The coaxial line of the multiband array was filled with polyethylene. The Teflon (stubs) and polyethylene (coaxial line) were both simulated with $\varepsilon_r = 2.2$ and $\tan \delta \sim 0$ (negligible dielectric losses). Fig. 1 shows a schematic of the designed multiband six-element array, and Fig. 2 shows a photograph of the fabricated and tested array.

S11(dB)

S21(dB)

Frequency (GHz)
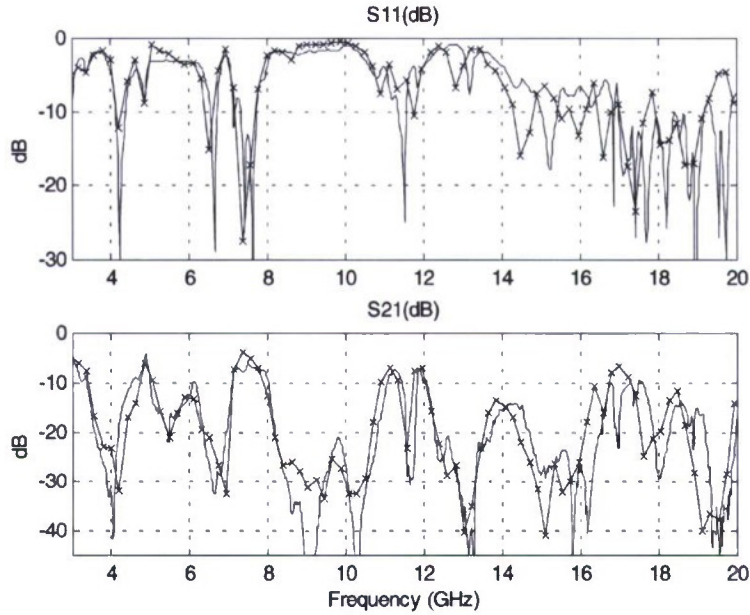
Fig. 3.   Comparison of simulated (solid with +) and measured (solid) S-parameter performance for six-element multiband coaxial CTS antenna array. Design frequencies are 4.2 GHz (C-band) and 19.4 GHz (K-band).

Following fabrication of the six-element multiband coaxial CTS antenna array, the physical dimensions of the structure were measured and found to be in accord with the design parameters. There was a slight air gap between the machined Teflon rings and the polyethylene-filled coaxial transmission line at the base of the stub. A new FDTD model that matched these measured physical dimensions and included the deviations from the initial design was then simulated. Simulations results were then compared with the measured S-parameters and radiation patterns for the fabricated prototype array.

Measurements of the coaxial CTS array were taken using the HP 8510B Network Analyzer. The S-parameters were characterized across 3–20 GHz band. These experimental results are shown along with the simulation S-parameter results obtained using FDTD in Fig. 3. As may be noted, there is a good agreement of resonant frequency performance between measurement and simulations. The multiband array was found to possess $S_{11} = -33$ dB and 98% radiated power ($S_{21} < -20$ dB) in the lower band at 4.2 GHz. The multiband array was found to possess S_{11} over -60 dB and 98% radiated power in the upper band at 19.4 GHz. The 10-dB bandwidth (where $S_{11} < -10$ dB, VSWR < 2) was found to be 6% (~ 250 MHz) in lower band and 12% (~ 2.2 GHz) in the upper band.

The radiation pattern of the six-element multiband coaxial CTS antenna array was also measured at 4.2 GHz (see Fig. 4). The measured radiation pattern produced broadside patterns, useful for many applications. There was a slight rotation in the radiation pattern away from the source ($\theta = 180°$). This deviation from the simulated results was small and did not change the broadside nature of the pattern or produce significant changes in the side lobe levels. The radiation pattern at 19.4 GHz was also measured in anechoic chamber (see Fig. 5) and found to be in agreement with simulation results. Increased side lobe levels in the 19.4 GHz pattern are seen toward endfire (at 180°) due to the effect of the feed cable and connectors. This effect was not significant enough to change the main broadside nature of the pattern or the maximum side lobe level as shown in Fig. 5.

Good agreement between simulated and measured results was seen for both S-parameter and radiation performance. For both simulated and measured results, the multiband coaxial CTS antenna array was seen to produce low reflection ($S_{11} < -20$ dB) and good radiation
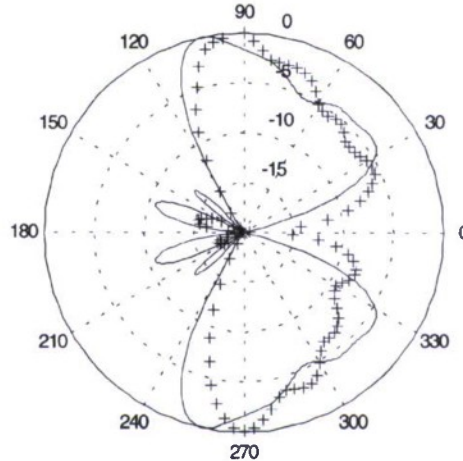
Fig. 4.   Comparison of measured (+s) and simulated (solid) radiation pattern at 4.2 GHz for the six-element multiband coaxial CTS antenna array. Feed is from 0°. Displayed on a dB-scale normalized to 0 dB.

characteristics (98% power radiated) at both 4.2 and 19.4 GHz. This validates the multiband design and illustrates the usefulness of the two-dimensional FDTD axially symmetric code as a design tool for coaxial CTS structures.

IV. TOLERANCE ANALYSIS

Planar CTS technology allows for relatively large tolerances in fabrication without significant alteration in the antenna performance. This dimensional insensitivity is critical to achieving low cost fabrication. It was important to determine if coaxial CTS structures possessed the same relative dimensional insensitivity.

Small changes were made in the simulation models, representing deviations from the design dimensions, and FDTD simulations were run with these changes included both as increases and decreases from the design dimensions. These changes were performed on all physical dimensions at the same time. S-parameter results were compared to original design results. It was found that even by allowing for a large tolerance as 5–10 mils, coaxial CTS structures maintained their antenna
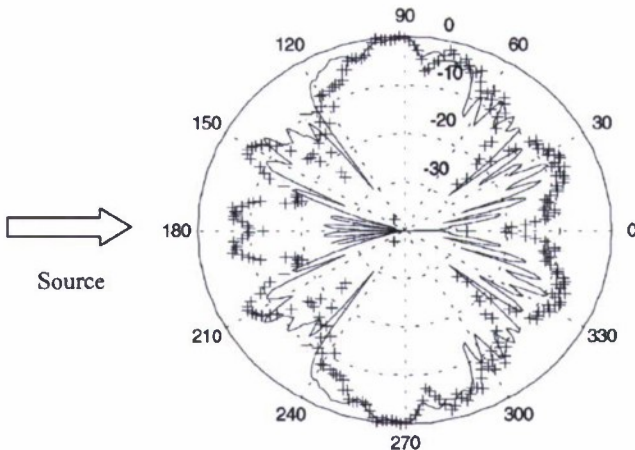
Fig. 5. Comparison of measured (+s) and simulated (solid) radiation pattern at 19.4 GHz for the six-element multiband coaxial CTS antenna array. Feed is from 180°. Displayed on a dB-scale normalized to 0 dB.
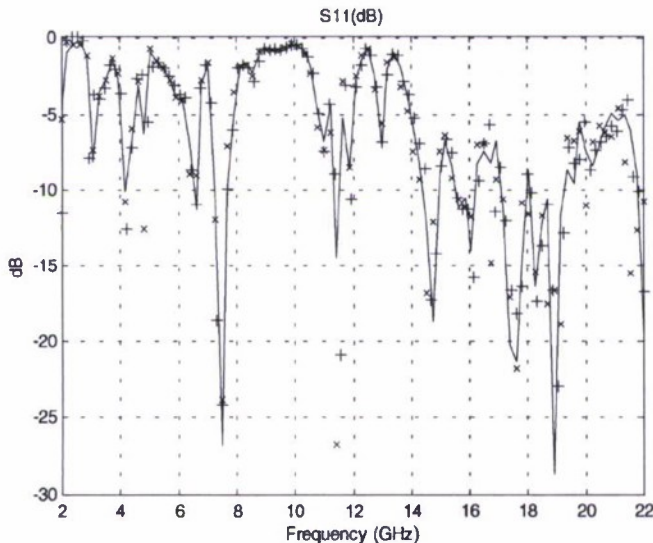

Fig. 6. Plot showing change in S_{11} for small changes in the physical dimensions of the six-element multiband coaxial CTS array. The solid line represents the original simulation. The +s represent a decrease in size from the original dimensions. The Xs represent an increase in size from the original dimensions.

performance and impedance matching characteristics at the design frequencies.

Specifically, FDTD simulation tests were run on three cases for the six-element multiband array. These cases consisted of simulation at the design specifications, simulation at dimensions one cell size (.129 mm or 5 mils) larger than the design specifications, and simulation at dimensions one cell size smaller than the design specifications. The results of the simulations for S_{11} are shown in Fig. 6. These results show that despite some small variation in the S-parameter performance of the array, its overall antenna performance was maintained in the regions around the design frequencies.

We also simulated the effect of small variations in the dielectric constant of the Teflon-filled multiband antenna array on the antenna performance. A simulation was performed using the expected value of Teflon ($\varepsilon_r = 2.1$), while two others were made using somewhat smaller and larger values for Teflon ($\varepsilon_r = 2.0$ and 2.2, respectively). The variations represent a change in the dielectric constant of approximately 5%. The results of these simulations are shown in Fig. 7. As it may be
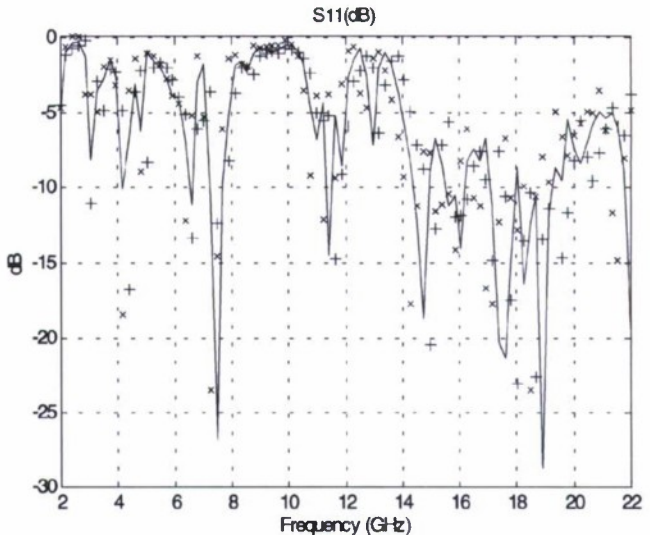
Fig. 7. Plot showing change in S_{11} for small changes in the dielectric constant of the six-element coaxial CTS array. The solid line represents $\varepsilon_r = 2.1$. The +s represent $\varepsilon_r = 2.0$. The Xs represent $\varepsilon_r = 2.2$.

seen, coaxial CTS array is also robust and relatively insensitive to small changes in the dielectric constant of filling material.

V. CONCLUSION

Coaxial CTS technology provides low cost, high-efficiency antenna arrays and with excellent radiation and S-parameter characteristics. The radial stubs of coaxial CTS arrays provide an omni-directional pattern in the plane perpendicular to the coaxial line. Coaxial CTS structures also possess the added advantages of ease of impedance matching, ease of feed, and maintains the insensibility to dimensional and dielectric constant tolerances.

In this paper, the design, construction and testing of a multiband antenna array was described. S-parameter performance from 3–20 GHz was measured using the HP8510B Network Analyzer. Good agreement was achieved between simulated S-parameter results obtained using FDTD and measured results, particularly at the desired multiband frequencies of 4.2 and 19.4 GHz. The measured and simulated results confirmed that it was possible to obtain low reflection, high-radiation efficiency, and good radiation pattern at frequencies in two different bands (C-band and K-band).

Radiation pattern measurements were also taken at 4.2 and 19.4 GHz and the broadside radiation pattern characteristic was verified. Several simulations were also performed to confirm the dimensional tolerance, and hence emphasize the low cost fabrication advantage of the coaxial CTS antenna design.

The excellent radiation performance shown by the coaxial CTS antenna arrays would enable many high-frequency communication applications for both military and commercial use. In particular, such high-efficiency antenna arrays would be useful for close range wireless connectivity (e.g., Bluetooth). Additionally, this technology has potential military application (e.g., Identification Friend-or-Foe (IFF) systems). They are compact in size and lightweight. Potentially, beam-steering capability can be accomplished in the same manner as planar CTS designs, either mechanically or using Ferroelectric materials.

REFERENCES

[1] W. W. Milroy, "The continuous transverse stub (CTS) array: Basic theory, experiment and application," in *Proc. Antenna Applications Symp.*, Allerton Park, IL, Sept. 25-27, 1991.

[2] ——, "Continuous transverse stub element devices and methods of making same," U.S. Patent 5 266 961, Aug. 29, 1991.

[3] M. F. Iskander, Z. Yun, Z. Zhang, R. Jensen, and S. Redd, "Design of a low-cost 2-D beem-steering antenna using ferroelectric material and the CTS technology," *IEEE Trans. Microwave Theory Tech.*, vol. 49, pp. 1000–1003, May 2001.

[4] Z. Zhang, M. F. Iskander, and Z. Yun, "Coaxial continuous transverse stub element device antenna array and filter," U.S. Patent 6 201 509, Nov. 5, 1999.

[5] M. F. Iskander, Z. Zhang, Z. Yun, and R. Isom, "Coaxial continuous transverse stub (CTS) array," *IEEE Microwave Wireless Component Lett.*, pp. 489–491, Dec. 2001.
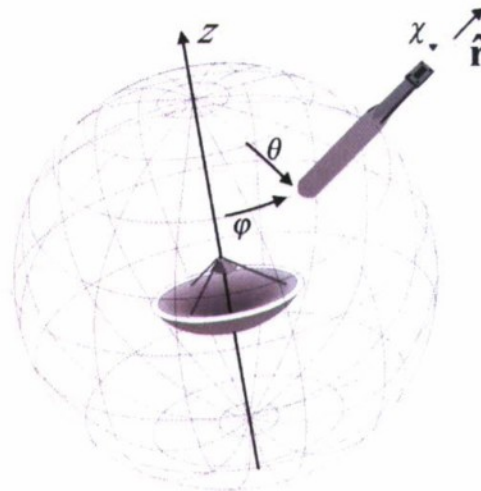
Near-Field, Spherical-Scanning Antenna Measurements With Nonideal Probe Locations

Ronald C. Wittmann, Bradley K. Alpert, and Michael H. Francis

Abstract—We introduce a near-field, spherical-scanning algorithm for antenna measurements that relaxes the usual condition requiring data points to be on a regular spherical grid. Computational complexity is of the same order as for the standard (ideal-positioning) spherical-scanning technique. The new procedure has been tested extensively.

Index Terms—Near-field measurements, probe-position correction, spherical scanning.

I. INTRODUCTION

As frequency increases and wavelength decreases, it becomes difficult to maintain mechanical tolerances in near-field scanning antenna measurements. Therefore, the paradigm shifts from taking measurements at predefined locations to accurately determining the positions where measurements are actually made. Standard algorithms for transformation from near-field to far-field require that data points lie on a regular grid. Our goal is to relax this condition without increasing computational complexity or sacrificing accuracy. Previously, we have dealt with planar near-field scanning [1]. Here, we turn our attention to spherical near-field scanning [2] . Although the details are different, the basic approach is the same: The technique relies on efficient linear transformation between spherical-mode coefficients and probe response at actual measurement locations. The conjugate-gradient method is applied to determine the coefficients that produce a weighted-least-squares match to the measured probe response. In the following, we sketch the theory and demonstrate the algorithm through numerical simulation.

II. THEORY

The electric field of an antenna, operating at frequency $f = \omega/2\pi$, may be expressed as an expansion of spherical waves

$$\mathbf{E}(\mathbf{r}) = \sum_{n=1}^{N} \sum_{m=-n}^{n} \left[b_{nm}^1 \mathbf{m}_{nm}(\mathbf{r}) + b_{nm}^2 \mathbf{n}_{nm}(\mathbf{r}) \right] \qquad (1)$$

where the vector modal (Hansen) functions $\mathbf{m}_{nm}$ and $\mathbf{n}_{nm}$ are described in [3, Ch. 7], for example, and the coefficients b_{nm}^1 and b_{nm}^2 completely characterize the radiated electromagnetic fields of the test

Fig. 1. Spherical scanning geometry.

antenna. The time-dependent factor $\exp(-i\omega t)$ has been suppressed. Equation (1) is valid in free space outside the minimum sphere; that is, outside the smallest sphere centered on the coordinate origin that encloses the radiating structure. The summation over n must be truncated for practical reasons. Normally, it suffices to choose $N \sim ka$, where a is the radius of the minimum sphere and $k = 2\pi/\lambda = \omega/c$.

In spherical scanning, the probe is effectively moved over the surface of a sphere of radius r so that it always "points" in the radial direction $-\hat{\mathbf{r}}$. As shown in Fig. 1, the probe's position and orientation is described by the Euler angles (φ, θ, χ), where θ and φ are the usual spherical-coordinate angles that define the location of the probe. The angle χ measures rotation of the probe about $\hat{\mathbf{r}}$. We assume that the receiving pattern is broad enough that small pointing errors are unimportant. Although possible in principle, correcting for probe wobble would be costly in terms of measurement and processing time.

In order to simplify the collection and processing of measurement data, we follow common practice [4] and restrict our attention to special probes that have a response $w(r, \varphi, \theta, \chi)$ with a simple χ dependence

$$w(r, \varphi, \theta, \chi) = -w(r, \varphi, \theta, -\pi/2)\sin\chi + w(r, \varphi, \theta, 0)\cos\chi. \qquad (2)$$

Such probes are not difficult to construct [5, Ch. 1]. They are called $\mu = \pm 1$ probes for reasons that may not be clear in this context. An example is a probe that measures transverse components of the electric field with, say, $E_\varphi = w(r, \varphi, \theta, 0)$ and $E_\theta = w(r, \varphi, \theta, -\pi/2)$. Any practical probe will approach a $\mu = \pm 1$ probe as r is increased.

The Jensen transmission formula [4] expresses the measurement vector $\mathbf{w}(\mathbf{r})$ as an expansion in spherical harmonics

$$\mathbf{w}(\mathbf{r}) \equiv w(r, \varphi, \theta, -\pi/2)\hat{\boldsymbol{\theta}} + w(r, \varphi, \theta, 0)\hat{\boldsymbol{\varphi}}$$
$$= \sum_{nm} \left[B_{nm}^1(kr)\mathbf{X}_{nm}(\hat{\mathbf{r}}) + B_{nm}^2(kr)\mathbf{Y}_{nm}(\hat{\mathbf{r}}) \right] \qquad (3)$$

where

$$\begin{pmatrix} B_{nm}^1 \\ B_{nm}^2 \end{pmatrix} = \mathbf{M}_n \begin{pmatrix} b_{nm}^1 \\ b_{nm}^2 \end{pmatrix}. \qquad (4)$$

In (4), $\mathbf{M}_n$ is a known 2×2 matrix depending on r and the probe receiving function. The vector spherical harmonics $\mathbf{X}_{nm}$ and $\mathbf{Y}_{nm} = i\hat{\mathbf{r}} \times \mathbf{X}_{nm}$ are defined by Jackson [6].

Using (2), (3), and (4), we write

$$\mathbf{W} = \mathbf{A}\mathbf{b}. \qquad (5)$$

(54) **COPLANAR WAVEGUIDE CONTINUOUS TRANSVERSE STUB (CPW-CTS) ANTENNA FOR WIRELESS COMMUNICATIONS**

(76) Inventors: **Magdy F. Iskander**, Honolulu, HI (US); **Wayne C. Kim**, Mililani, HI (US); **Jodie M. Bell**, Honolulu, HI (US)

Correspondence Address:
LEIGHTON K. CHONG
GODBEY GRIFFITHS REISS & CHONG
1001 BISHOP STREET, PAUAHI TOWER
SUITE 2300
HONOLULU, HI 96813 (US)

(57) **ABSTRACT**

An improved continuous transverse stub (CTS) antenna has coplanar waveguide (CPW) feed elements spaced apart aligned in parallel and mounted perpendicular to a planar substrate base made of a low dielectric material. A continuous transverse stub extends perpendicularly through a clearance gap in the CPW feed elements on the ground plane of the substrate base. The antenna is fed with a simple coplanar waveguide transmission line formed by the parallel CPW elements. The antenna employs the coplanar waveguide with CTS technology, preferably in a planar microstrip configuration, to produce a broadside radiation pattern with a maximum in the +z direction, perpendicular to the plane of the antenna. The CPW-CTS antenna offers the advantages of a broadside radiation pattern, low input impedance, high radiation efficiency, low fabrication cost, use of simple coaxial or microstrip transmission line feed, and simple integration with microstrip circuitry in a transceiver front-end. The CPW-CTS antenna may be integrated in a single frequency band or in multiband arrays and could provide radiation beam steering capability when integrated with a substrate of tunable dielectric material such as BSTO.

FIG. 1(a)

FIG. 1(b)

FIG. 2(a)

Measured and Predicted Return Loss

FIG. 2(b)

Measured and Predicted Insertion Loss
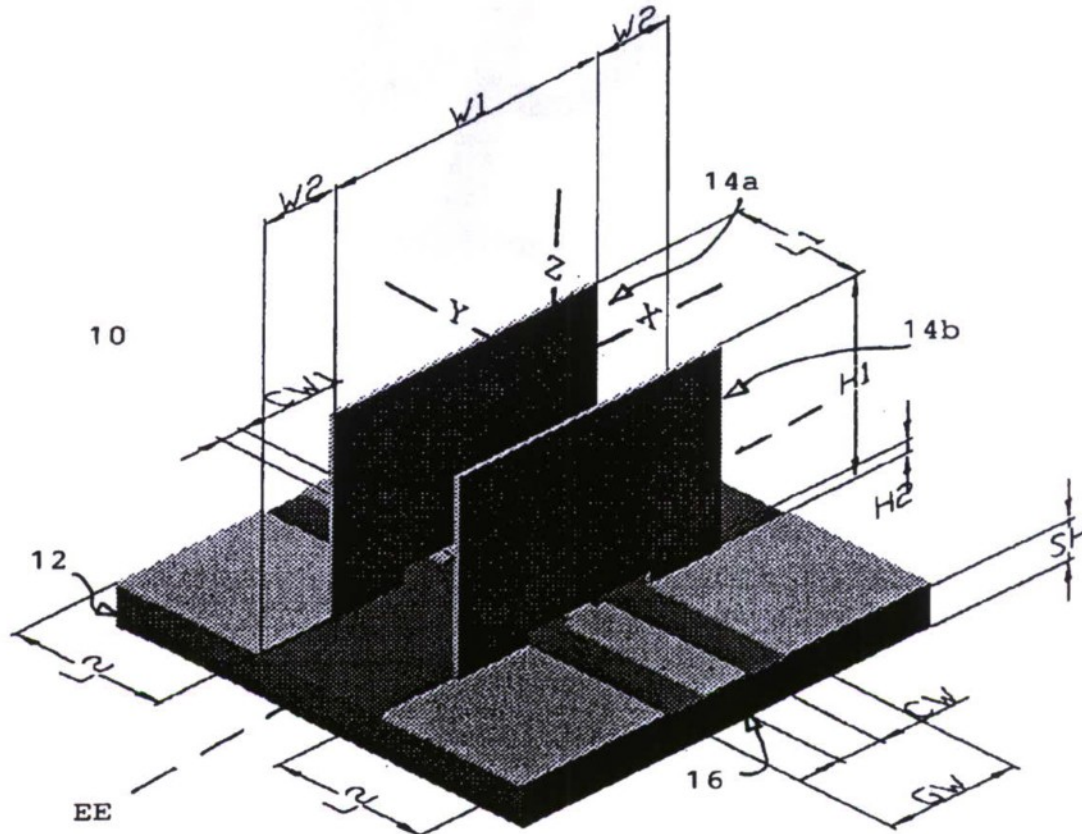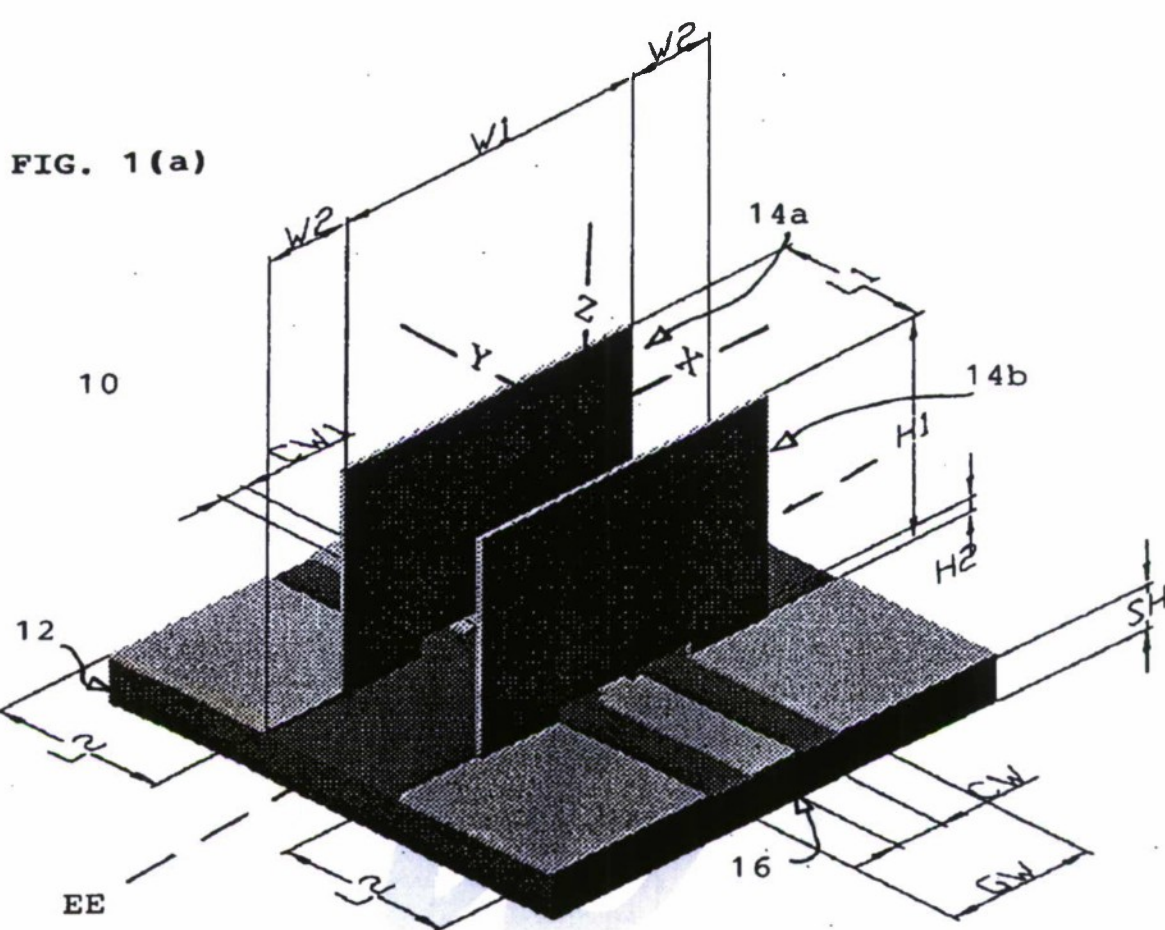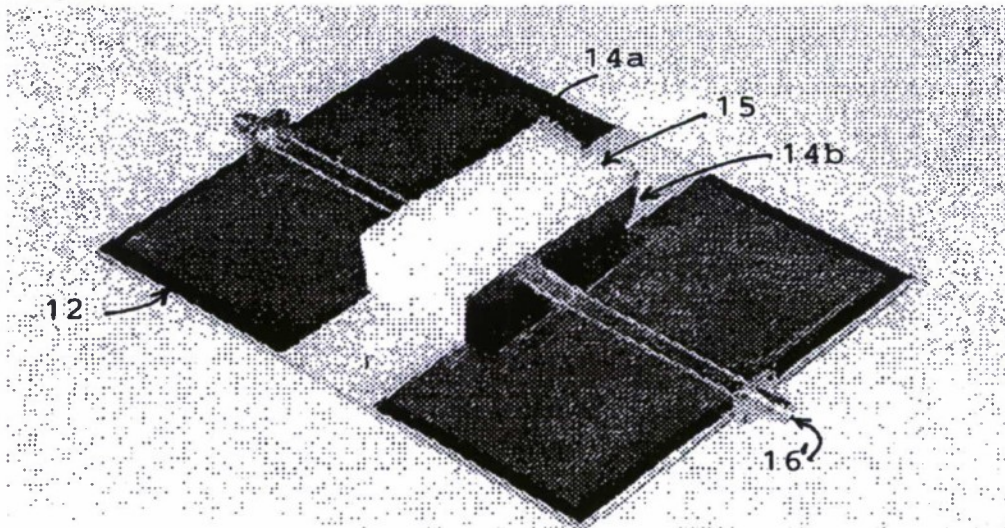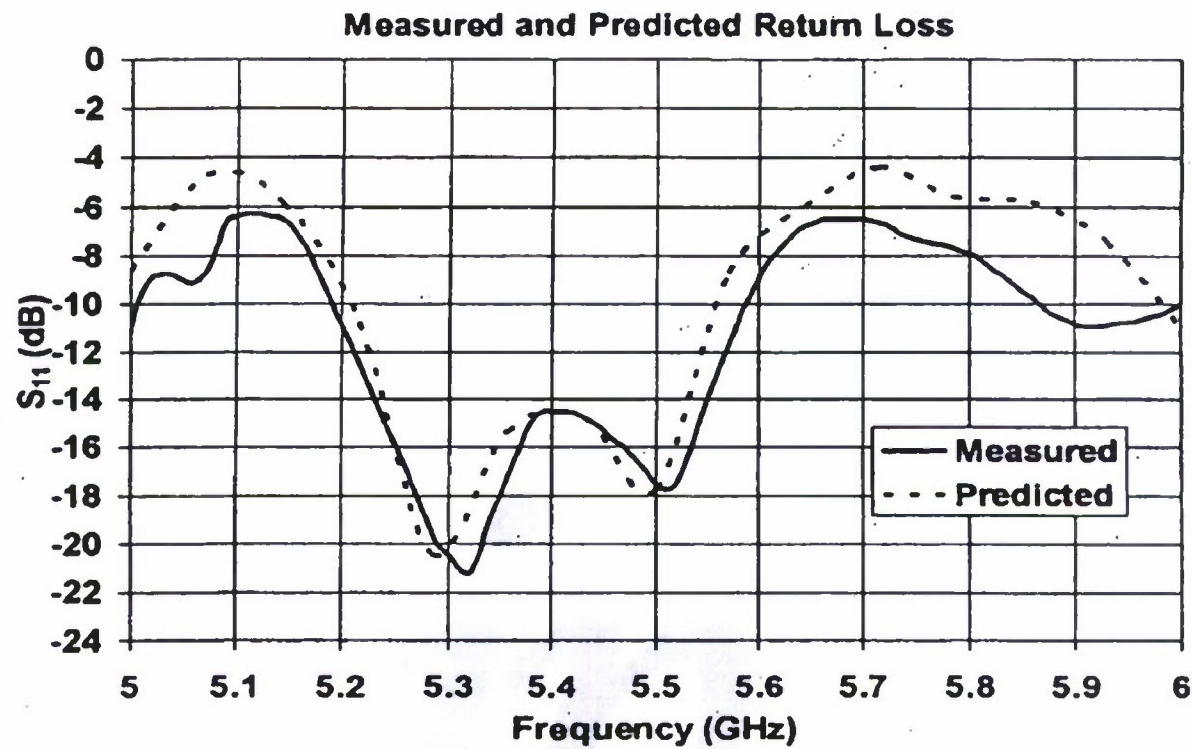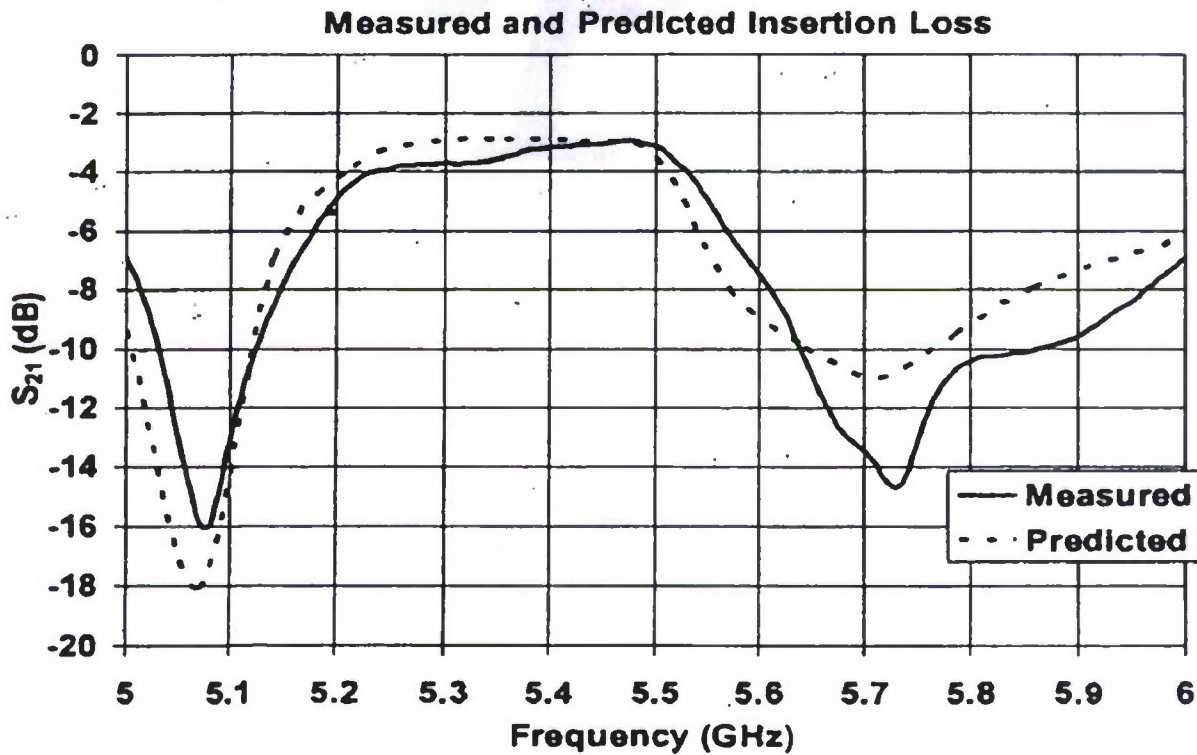
FIG. 3(a)   E-Plane Radiation Pattern
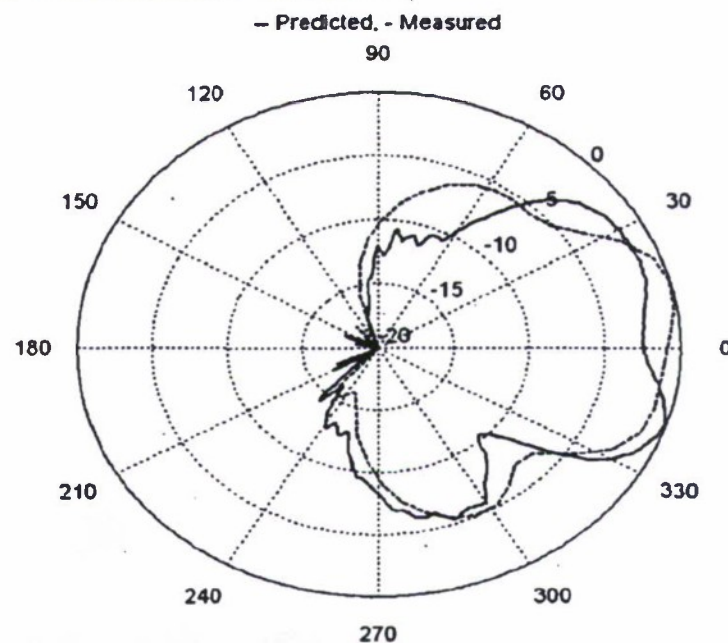
FIG. 3(b)   H-Plane Radiation Pattern

Figure 4

Z

X

High Frequency
Low Frequency

Substrate, ε_r

Load

y

X

s

Low Frequency
Radiating Stubs

High Frequency
Radiating Stubs

Feed

Figure 5

θ2

θ1

z

y

Low Loss ε_r

Tunable ε_r

Substrate
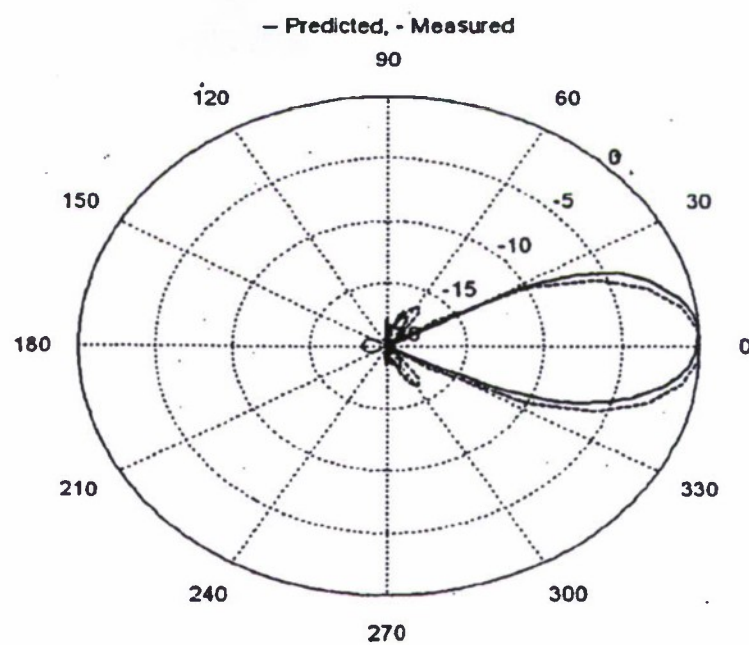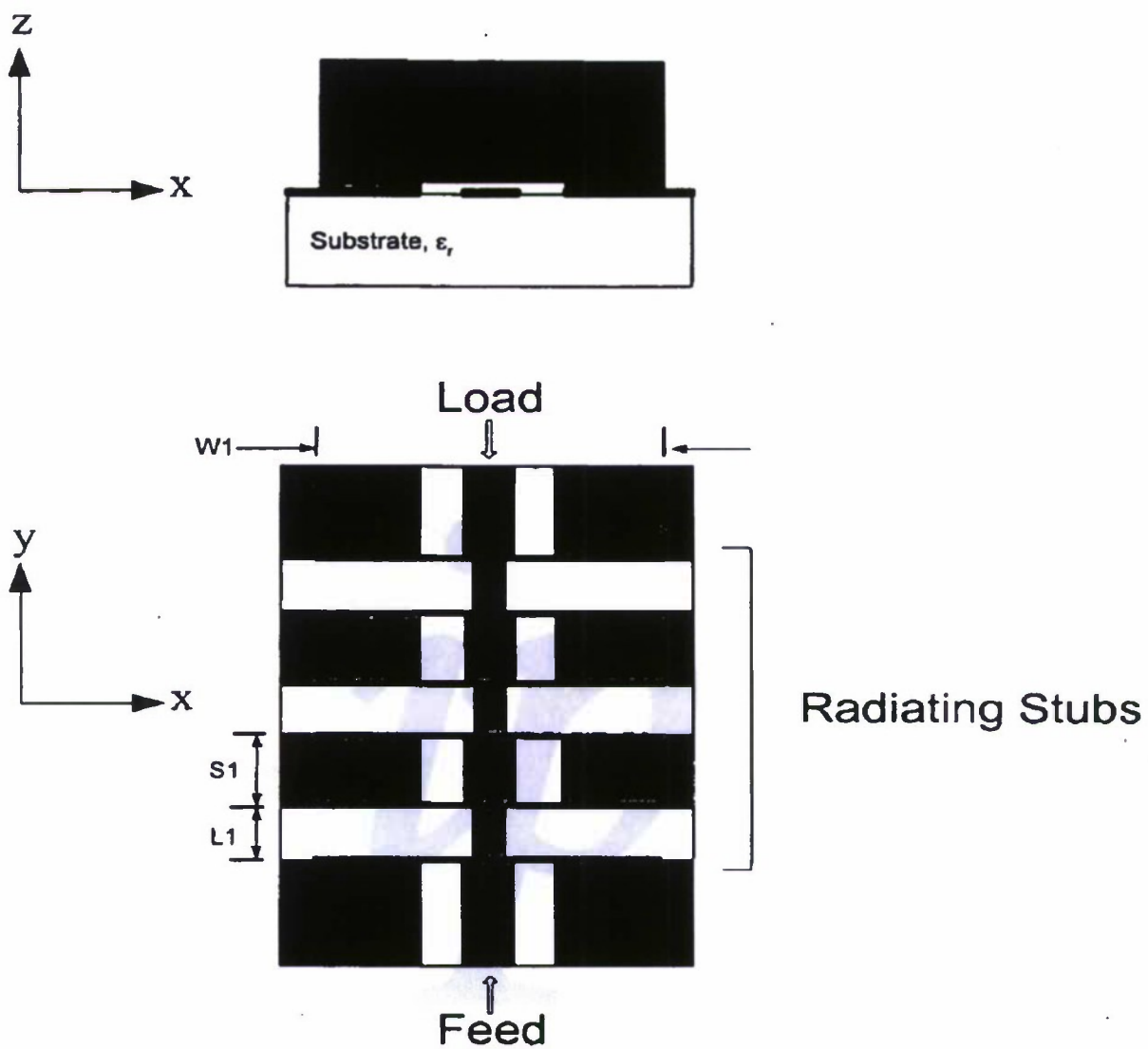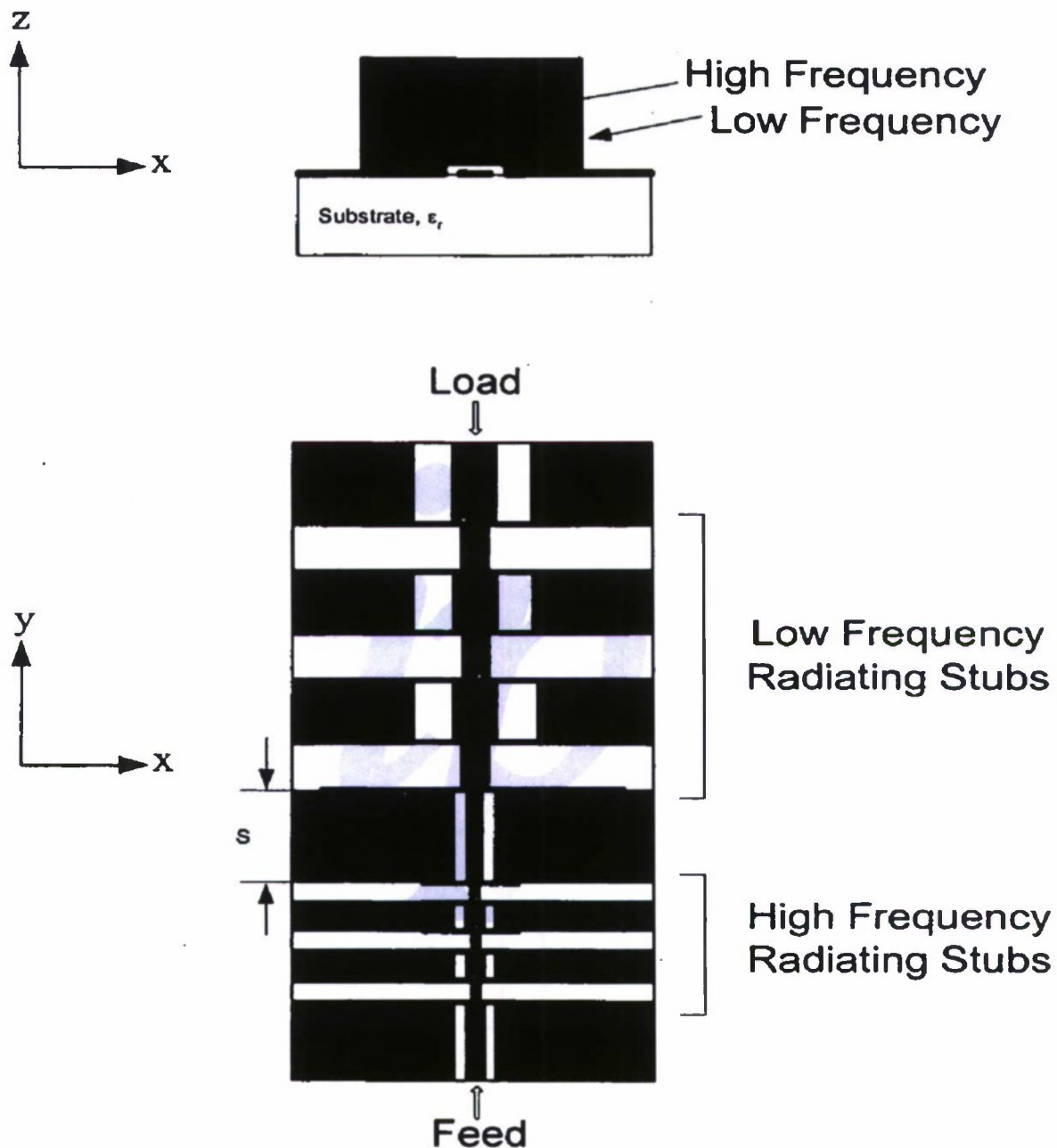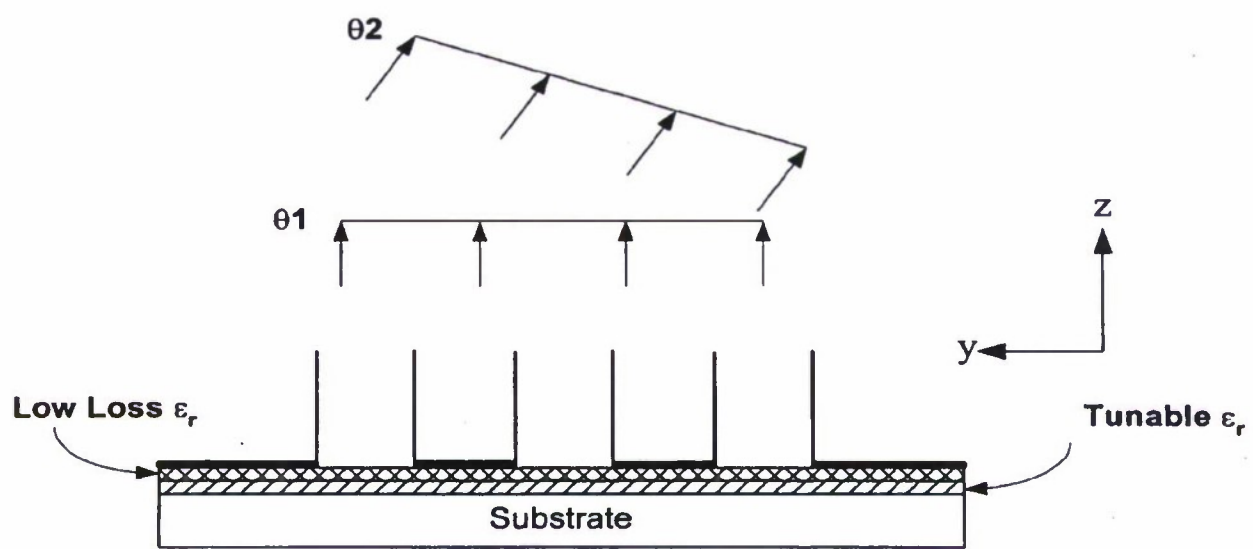
Figure 6

COPLANAR WAVEGUIDE CONTINUOUS TRANSVERSE STUB (CPW-CTS) ANTENNA FOR WIRELESS COMMUNICATIONS

[0001] This U.S. patent application claims the priority of U.S. Provisional Application No. 60/558,592 filed on Mar. 31, 2004, entitled "Coplanar Continuous Transverse Stub (CTS) Antennas", by the same inventors.

TECHNICAL FIELD

[0002] This invention generally relates to continuous transverse stub (CTS) antennas, and more particularly, to an improved design that is mountable on a flat surface while being fed using a simple and low cost coaxial, microstrip, or coplanar transmission line and has multi-band capabilities and also low cost beam steering using ferroelectric technology.

BACKGROUND OF INVENTION

[0003] The planar continuous transverse stub (CTS) antenna and antenna array were originally invented and patented by Raytheon in the early 1990's, for example, in U.S. Pat. No. 5,266,961, by W. W. Milroy, issued 29 Aug. 1991, entitled "Continuous transverse stub (CTS) element devices and methods of making same". Benefits of the CTS antenna include compact size, lightweight, low cost, increased directive gain with increased radiating elements, and high efficiencies. The CTS antenna finds applications in the areas of mobile wireless and satellite communications and various military radar systems operating in the 500 MHz to 90 GHz frequency band.

[0004] A new coaxial version of the CTS technology with omni-directional radiation pattern is described in M. F. Iskander, Z. Zhang, Z. Yun, and R. Isom, "Coaxial Continuous Transverse Stub (CTS) Array,"*IEEE Microwave and Wireless Components Letters,* vol. 11, no. 12, pp. 489-491, 2001, and in U.S. Pat. No. 6,201,509, of inventors in common herewith. A coaxial version of the CTS technology for multiband operation was reported in R. Isom, M. F. Iskander, Z. Yun, Z. Zhang, "Design and Development of Multiband Coaxial Continuous Transverse Stub (CTS) Antenna Arrays,"*IEEE Trans. Antennas and Prop.,* vol. 52, no. 8, Aug. 2004. In particular, it was demonstrated that multiband performance at the 4.2 and 19.4 GHz frequency band with equivalent radiated power (~98%) and good impedance match is possible to achieve using this technology.

[0005] However, it is deemed desirable to improve the CTS antenna to be flat-mounted and have a broadside radiation pattern, low fabrication cost, simple coaxial, coplanar, or microstrip transmission line feed, and simple integration with microstrip circuitry in a transceiver front-end. With the flat implementation of the design, it is possible to provide beam steering capabilities through the integration of the antenna structure with a tunable dielectric substrate material as will be described in more details herein.

SUMMARY OF INVENTION

[0006] In accordance with the present invention, an improved continuous transverse stub (CTS) antenna has coplanar waveguide (CPW) feed elements spaced apart aligned in parallel with each other (x-directed) and mounted perpendicular to a planar substrate base made of a material of low dielectric constant. The CPW feed elements have associated with them quasi TEM modes which are interrupted by the presence of a continuous transverse stub on the ground plane of the substrate base. The presence of the purely reactive transverse stub elements couples a longitudinal, z-directed displacement current across the parallel plate transmission line and coplanar waveguide interface. This induced current excites z-directed EM waves where the electric field is linearly polarized in the transverse direction (y-directed) to the stub elements. The improved CPW-CTS antenna operates as a traveling-wave-fed antenna.

[0007] The transverse stub is preferably formed by a central portion of width (CW1) made of a conductive coating disposed on the ground plane surface with gap portions of width (CW) on each side thereof, providing a total stub gap width (GW). The CPW feed elements are preferably a pair of parallel plates spaced apart by a first length (L1) and having a width (W1) and height (H1) above the ground plane. The transverse stub extends perpendicularly through a clearance gap of height (H2) in the transverse direction across the ground plane. The clearance gap height (H2) is used to adjust the coupling capacitance to compensate the inductance of the purely reactive stub elements. The antenna is fed with a simple coplanar waveguide transmission line formed by the parallel CPW elements. The feed point (L2) is positioned away from the edge of the stubs to maintain a good impedance match. L2 is carefully chosen to obtain the desired radiation pattern as a result of the axis EE of the feed line being oriented in line with the E-Plane radiation pattern. The substrate height (SH) is chosen for structural integrity and for improving the directive gain.

[0008] In a preferred embodiment, the signal conductor width (CW), total stub gap width (GW), and dielectric constant ($\in_r$) were chosen to provide 50 ohms feed impedance. The length (L1), width (W1), and height (H1) of the parallel plates were selected to be approximately a half wavelength, one wavelength, and one-third wavelength, respectively. The values of CW and CW1 were carefully chosen and after extensive simulations to produce increased radiated power and at the same time maintain good impedance match. The width (W2) of the opposite outward portions from the plates is selected to reduce undesired back lobes, most notably in the H-Plane radiation measurements.

[0009] The CPW-CTS antenna of the present invention employs the coplanar waveguide with CTS technology, preferably in a planar microstrip configuration, to produce a broadside radiation pattern with a maximum in the +z direction, perpendicular to the plane of the antenna. The coplanar CTS offers the advantages over previous designs of a broadside radiation pattern, low input impedance, high radiated power, low fabrication cost, use of simple coaxial or microstrip transmission line feed, and simple integration with microstrip circuitry in a transceiver front-end.

[0010] Other objects, features, and advantages of the present invention will be explained in the following detailed description having reference to the appended drawings.

BRIEF DESCRIPTION OF DRAWINGS

[0011] FIG. 1(*a*) shows a schematic of a coplanar waveguide continuous transverse stub (CPW-CTS) antenna,

and FIG. 1(*b*) shows a fabricated prototype example of the CPW-CTS antenna in accordance with the present invention.

[0012] FIG. 2(*a*) is a chart showing measured to predicted values for return loss, and FIG. 2(*b*) is a chart showing measured to predicted values for insertion loss.

[0013] FIG. 3(*a*) is a chart showing measured to predicted values for E-Plane radiation pattern, and FIG. 3(*b*) is a chart showing measured to predicted values for H-Plane radiation pattern.

[0014] FIG. 4 shows an example of a coplanar waveguide continuous transverse stub array.

[0015] FIG. 5 shows an example of a multiband coplanar waveguide continuous transverse stub.

[0016] FIG. 6 shows an example of a CPW-CTS array with beam steering capabilities.

DETAILED DESCRIPTION OF INVENTION

[0017] The present invention provides an improvement upon previously known CTS technology, for example, as described in U.S. Pat. No. 6,201,509, to a named inventor in common herewith, which is incorporated by reference in its entirety herein. The CTS antenna employs a continuous transverse stub to form reactive or radiating elements for microwave, millimeter-wave, and quasi-optical filters and antennas. Purely reactive elements are formed by leaving a conductive coating on the surface of the stub elements to form radiating elements. The conductive material may be a ferroelectric material. The stub may be formed with individual stub elements separated from each other by air gaps or an appropriate material.

[0018] Referring to FIG. 1(*a*), a schematic diagram illustrates a co-planar waveguide, continuous transverse stub (CPW-CTS) antenna 10 in accordance with the present invention. The CPW-CTS antenna 10 has a planar substrate base 12 made of a material with a low dielectric constant, and a pair of coplanar waveguide (CPW) feed elements 14*a*, 14*b* extending longitudinally in the X-direction aligned in parallel with each other and mounted perpendicular to the plane of the substrate base 12. The CPW feed elements 14*a*, 14*b* have associated with them quasi TEM modes which are interrupted by the presence of a continuous transverse stub element 16 formed on the ground plane. The presence of the purely reactive transverse stub elements couples a longitudinal, z-directed displacement current across the parallel plate transmission line and coplanar waveguide interface. This induced current excites z-directed EM waves where the electric field is linearly polarized in the transverse direction (Y-direction) to the stub elements, so that the CPW-CTS antenna operates as a traveling-wave-fed antenna.

[0019] The coupling values from the CPW elements to the stub radiating elements are primarily dependent on the following dimensional parameters:

[0020] Height (H1) of the top of the CPW feed elements above the ground plane

[0021] Gap clearance height (H2) of the CPW feed elements over the ground plane

[0022] Width (W1) of CPW elements across the ground plane

[0023] Width (W2) on each side externally from the width of CPW elements

[0024] Distance (L1) between parallel CPW elements

[0025] Distance (L2) on each side externally from the CPW elements

[0026] Central portion width (CW1) between stub radiating elements

[0027] Signal conductor width (CW) of stub radiating elements

[0028] Total stub gap width (GW) of central portion and stub radiating elements

[0029] Dielectric constant ($\in_r$) of conductive material for transverse stub

[0030] Substrate height (SH)

[0031] The transverse stub is preferably formed by a central portion of width (CW1) made of a conductive coating disposed on the ground plane surface with gap portions of width (CW) on each side thereof, providing a total stub gap width (GW). The CPW feed elements are preferably a pair of parallel plates spaced apart by a first length (L1) and having a width (W1) and height (H1) above the ground plane. The transverse stub extends perpendicularly through a clearance gap of height (H2) in the transverse direction across the ground plane. The clearance gap height (H2) is used to adjust the coupling capacitance to compensate the inductance of the purely reactive stub elements. The antenna is fed with a simple coplanar waveguide transmission line formed by the parallel CPW elements. The feed point (L2) is positioned away from the edge of the stubs to maintain a good impedance match. L2 is carefully chosen to obtain the desired radiation pattern as a result of the axis EE of the feed line being oriented in line with the E-Plane radiation pattern. The substrate height (SH) is chosen for structural integrity and for improving the directive gain.

[0032] In a preferred embodiment, the signal conductor width (CW), total stub gap width (GW), and dielectric constant ($\in_r$) were chosen to provide 50 ohms feed impedance. The length (L1), width (W1), and height (H1) of the parallel plates were selected to be approximately a half wavelength, one wavelength, and one-third wavelength, respectively. The values of CW and CW1 were carefully chosen and after extensive simulations to produce increased radiated power and at the same time maintain good impedance match. The width (W2) of the opposite outward portions from the plates is selected to reduce undesired back lobes, most notably in the H-Plane radiation measurements.

[0033] For simulation testing of the operating characteristics of the CPW-CTS antenna, a WIPL-D electromagnetic modeling program was used. It is a full 3-D electromagnetic simulation based on the method of moments, e.g., as described by Kolundzija, B., Ognjanovic, J. and Sarkar, T., *WIPL-D: Electromagnetic Modeling of Composite Wire and Plates Structures—Software and User's Manual*, Artech House, Boston, 2000. An antenna operating at 5.3 GHz was designed and desired features include low input impedance, high radiated power, and a broadside radiation pattern. The

design dimensions obtained after extensive simulations were as follows:

[0034] H1=18.2 mm

[0035] H2=1.5 mm

[0036] W1=54.5 mm

[0037] W2=28.3 mm

[0038] L1=27.3 mm

[0039] L2=54.5 mm

[0040] CW=CW1=4.7 mm

[0041] GW=5.97 mm

[0042] Dielectric constant $\in_r$=2.94 (RT/Duroid 6002)

[0043] SH=3.01 mm.

[0044] A prototype of the CPW-CTS antenna was fabricated using the above simulation-designed parameters, as shown in FIG. 1(b). A coaxial tube type of transverse stub 16' (as described in U.S. Pat. No. 6,201,509) was used in this prototype. In the figure, a styrofoam spacer 14 is shown inserted over the radiating stub 16' between the CPW elements 14a, 14b to accurately maintain the radiating dimensions of the design distance between elements.

[0045] Referring to FIGS. 2(a) and 2(b), the charts of frequency (GHz) to signal (dB) show good agreement between the measured and the predicted (simulated) return and insertion losses, respectively. As can be seen, S_{11} was better than −10 dB between 5.2 and 5.6 GHz with a radiated power ratio greater than 40%, where the radiated power ratio is given by:

$$Pwr_{rad} \approx \frac{Pwr_{rad} - Pwr_{refl} - Pwr_{trans}}{Pwr_{tot}} * 100\% \tag{1}$$

[0046] The term transferred power is used to account for the amount of power received at the end of the antenna and after the radiating stub.

[0047] FIGS. 3(a) and 3(b) shows good agreement between the measured and the predicted E-Plane and H-Plane radiation patterns at 5.3 GHz, respectively. The measured E-Plane beam peak was −18° and the measured 3-dB beam width was 74.8°. The maximum back lobe was −14 dB from the maximum beam peak. The maximum back lobe of the measured H-Plane was −17 dB down from the maximum beam peak. The good agreement between predicted and measured results validates the predictability of the performance of this new antenna design.

[0048] Other design selections and modifications may be made to optimize the dimensions, characteristics, and/or performance of the CPW-CTS antenna. For example, the square stubs of the CPW-CTS antenna shown in FIG. 1(a) may be replaced with semi-circular stubs in order to form a low profile antenna with radial dimensions equivalent to the height (H1). Simulated results of such a configuration showed identical results.

[0049] Example of CPW-CTS Antenna Array

[0050] The invented continuous transverse stub design can be integrated in an array arrangement as shown in FIG. 4 to increase the gain and narrow the beam width of the overall antenna. Increased gain may be achieved by increasing the amount of stub elements. Accomplishing this using a single feed in the antenna arrangements provides a significant advantage in simplicity of implementation and low cost of fabrication. The coupling from the microstrip to the radiating elements is primarily dependent on the parallel plate spacing (L1) and width (W1). The element to element spacing (S1) controls the amount of mutual coupling between each element. Element spacings are chosen to be approximately equal to an integral number of wavelengths (typically one) within the coplanar waveguide region. With increased elements, appropriate variation of the plate spacing (L1) and element to element spacings (S1) are required to achieve the desired radiated power based on the series nature of the array.

[0051] Example of CPW-CTS Multiband Array

[0052] A multiband planar array for microwave and millimeter wave applications may be constructed through appropriate selection of inter-element spacings and continuous transverse stub parameters. The selected frequency bands may be well separated due to the dispersionless nature of the air filled parallel plate transmission line structure and the frequency independent orthogonality of the coplanar waveguide modes. A six element multiband (two bands in this case with three elements array in each band) coplanar waveguide continuous transverse stub is shown in FIG. 5. Periodically-spaced continuous transverse stub elements designed to operate at the appropriate frequency bands are arranged with the high frequency radiators closest to the feed and low frequency radiators farthest from the feed. In this case the first three elements radiate at high frequency and last three radiate at lower frequencies. Typical planar array developments require the design of separate subarrays for each frequency band then merged to form the multiband array. Appropriate multiband performance is achieved with proper selection of the sub array spacing (S). Based on the wavelength dependence of the parallel plate elements and inter-element spacings, the subarray designed for higher frequencies will be relatively smaller compared with those for lower frequencies. Extended frequency bands may be realized using the aforementioned techniques.

[0053] Example of CPW-CTS Array With Beam Steering Capabilities

[0054] The coplanar implementation of the continuous transverse stub technology also lends itself to effective and low cost designs of antenna arrays with beam steering capabilities. As shown in FIG. 6, by including a layer of tunable dielectric materials such as Barium Strontium Oxide (BSTO), and providing the necessary biasing arrangement required to provide proper modulation of the dielectric constant, the radiation pattern of the array may be steered along the axis of the array. To help with the reduction of the insertion loss of the developed devices, a multilayer arrangement including a low loss dielectric between the conductors and the Barium Strontium Oxide layer (as shown in FIG. 6) may be implemented. For more details on BSTO technology for CTS antenna arrays, see W. Kim, M. Iskander, and C. Tanaka, "High-performance low-cost phase-shifter design

based on ferroelectric materials technology", *IEE Electronic Letters,* 2004, vol. 40, no. 21, pp. 1345-1347.

[0055] The coplanar waveguide continuous transverse stub array has many performance, reproducibility, and application advantages over conventional slotted waveguide array, printed patch array, and reflector and lens antenna approaches in applications for which planar arrays have been inappropriate due to traditional bandwidth and/or cost limitations. Producibility advantages include considerable insensitivity to dimensional and limited material properties variations and simplified fabrication and processing procedures and ease of integration in the transceiver systems. This all leads to the low cost advantage of this technology. Making antenna components with BSTO ceramics with reliable dimensions in cylindrical geometries is currently achievable, and the planar structure of this CPW-CTS antenna configuration will facilitate this with ease.

[0056] In summary, a new coplanar waveguide CTS (CPW-CTS) antenna has been described. Advantages of this new design include low cost, low profile, light weight, and a very simple planar microstrip feed configuration. The design was validated by comparing measured results of a designed prototype against simulation results for a single element CPW-CTS design in the 5.2 to 5.6 GHz band. Both S-parameters and radiation pattern results were examined and good agreement between the experimental and simulation data were illustrated. Specifically, the designed one-element antenna exhibited a well-formed broadside main beam at the 5.3 GHz and good 50 ohms impedance match (−10 dB) from 5.2 to 5.5 GHz.

[0057] For further development, the coplanar waveguide CTS antenna design can be loaded with multiple elements to form a series array for improved directive gain and narrow beam widths. A multiple element array could also be formed with frequency selective sections to enable multiband operation. The planar design could be integrated with tunable ferroelectric materials to introduce multiband, electronic beam scanning capabilities, for example, as discussed in M. Iskander, Z. Zhang, Z. Yun, R. Isom, M. Hawkins, R. Enrick, B. Bosco, J. Synowczynski, and B. Gersten, "New phase shifters and phased antenna array designs based on ferroelectric materials and CTS technologies,"*IEEE Trans. Microwave Theory Tech.,* vol. 49, no. 12, December 2001, and W. Kim, M. F. Iskander, "High Performance Low Cost Phase Shifters Design Based on the Ferroelectric Materials Technology,"*IEE Electronic Letters,* 2004, vol. 40, no. 21, pp. 1345-1347.

[0058] It is understood that many modifications and variations may be devised given the above description of the principles of the invention. It is intended that all such modifications and variations be considered as within the spirit and scope of this invention, as defined in the following claims.

1. An improved continuous transverse stub (CTS) antenna comprising:

(a) a planar substrate base made of material of a low dielectric constant;

(b) a pair of coplanar waveguide (CPW) feed elements spaced apart by a given distance aligned in parallel with each other and mounted perpendicularly on a ground plane surface of the substrate base, wherein said CPW

feed elements form a parallel feed transmission line through a coplanar waveguide interface; and

(c) a continuous transverse stub disposed on the ground plane surface of the substrate base extending in a transverse direction perpendicularly through a clearance gap formed through the CPW feed elements, wherein said transverse stub acts as a reactive, radiating member in conjunction with the feed transmission line of the coplanar waveguide interface for operation as a traveling-wave-fed antenna.

2. An improved continuous transverse stub (CTS) antenna according to claim 1, wherein the CPW feed elements have a first height (H1) above the ground plane surface and a first width (W1) across the ground plane surface, a gap height (H2) of the clearance gap above the ground plane surface, a second width (W2) of opposite outward portions on the ground plane surface on each outward side of the CPW feed elements, a first length (L1) between the parallel CPW feed elements, and a second length (L2) of opposite outward portions on the ground plane surface on each outward side of the CPW feed elements.

3. An improved continuous transverse stub (CTS) antenna according to claim 2, wherein the clearance gap height (H2) is used to adjust a coupling capacitance to compensate for inductance of the reactive transverse stub.

4. An improved continuous transverse stub (CTS) antenna according to claim 2, wherein the second length (L2) of the outward portions from the CPW feed elements is selected to maintain a good impedance match.

5. An improved continuous transverse stub (CTS) antenna according to claim 2, wherein the preferred first length (L1), first width (W1), and first height (H1) are selected to be approximately a half wavelength, one wavelength, and one third wavelength of a traveling wave sent on the feed transmission line.

6. An improved continuous transverse stub (CTS) antenna according to claim 2, wherein the CPW feed elements are a pair of rectangular plates in parallel having the first length (L1) between them and each having the first width (W1) and first height (H1).

7. An improved continuous transverse stub (CTS) antenna according to claim 2, wherein the CPW feed elements are a pair of semi-circular plates in parallel having the first length (L1) between them and each having the first width (W1) and first height (H1) at its apex.

8. An improved continuous transverse stub (CTS) antenna according to claim 2, wherein the width (W2) of the opposite outward portions on each side of the first width (W1) of the CPW feed elements is preferably one third wavelength of a traveling wave sent on the feed transmission line to reduce undesired back lobes.

9. An improved continuous transverse stub (CTS) antenna according to claim 1, wherein the transverse stub is formed by a central portion of width (CW1) made of a conductive coating extending longitudinally in the transverse direction on the ground plane surface through the clearance gap formed through the CPW feed elements, and a pair of stub gaps of width (CW) on each side of the central portion separating it from opposite outward portions on the ground plane surface on each outward side of the pair of gaps.

10. An improved continuous transverse stub (CTS) antenna according to claim 9, wherein the central portion width (CW1), signal conductor width (CW) of the pair of

stub gaps, total stub gap width (GW), and dielectric constant ($\in_r$) of the stub material are chosen to provide 50 ohm feed impedance.

11. An improved continuous transverse stub (CTS) antenna according to claim 1, wherein the CPW feed elements have a first height (H1) above the ground plane surface and a first width (W1) across the ground plane surface, a gap height (H2) of the clearance gap above the ground plane surface, a second width (W2) of opposite outward portions on the ground plane surface on each outward side of the CPW feed elements, a first length (L1) between the parallel CPW feed elements, a second length (L2) of opposite outward portions on the ground plane surface on each outward side of the CPW feed elements, and wherein the transverse stub is formed by a central portion of width (CW1) made of a conductive coating extending longitudinally in the transverse direction on the ground plane surface through the clearance gap formed through the CPW feed elements, and a pair of stub gaps of width (CW) on each side of the central portion separating it from opposite outward portions on the ground plane surface for a total stub gap width (GW), said antenna being designed for operating at 5.3 GHz and having the following approximate values selected to provide for low input impedance, high radiated power, and a broadside radiation pattern:

H1=18.2 mm

H2=1.5 mm

W1=54.5 mm

W2=28.3 mm

L1=27.3 mm

L2=54.5 mm

CW=CW1=4.7mm

GW=5.97 mm

Dielectric constant ($\in_r$)=2.94 (RT/Duroid 6002)

SH=3.01 mm.

12. An improved continuous transverse stub (CTS) antenna according to claim 1, formed as a coplanar waveguide continuous transverse stub array.

13. An improved continuous transverse stub (CTS) antenna according to claim 1, formed as a multiband coplanar waveguide continuous transverse stub antenna.

14. An improved continuous transverse stub (CTS) antenna according to claim 1, formed as a CPW-CTS array with beam steering capabilities.

* * * * *

High Performance Low Cost Ferroelectric Phase Shifters Designed for Simple Biasing

Wayne Kim[1]*, Magdy F. Iskander[1], and Clifford Tanaka[2]

[1]Hawaii Center for Advanced Communications, University of Hawaii, Honolulu, HI.

[2]Trex Enterprises, Inc., Kauai, HI.

kimwayne@hawaii.edu, iskander@spectra.eng.hawaii.edu, and ctanaka@trexhawaii.com

Abstract: A novel approach in ferroelectric phase shifters design using $Ba_xSr_{1-x}TiO_3$ (BSTO) films in a multilayer dielectric coplanar waveguide structure is described. By including a low loss dielectric layer (SiO_2) between the coplanar waveguide conductors and the ferroelectric material in conjunction with a via to allow the signal conductors to contact the ferroelectric layer to employ biasing, significant reduction in insertion loss can be achieved in conjunction with a three fold increase in figure of merit (°/dB) compared to the case with direct metallization on the ferroelectric layer.

I. Introduction

To enable and fully develop next generation of integrated (terrestrial wireless, satellite, and GPS) and broadband wireless communications technology and realize its much anticipated benefits in commercial and military applications, it is critically important that low cost and high gain phased antenna arrays with beam steering capability be developed. These antennas may require thousands of phase shifters and hence some focus needs to be placed on exploring new and innovative designs for low cost and high performance microwave and millimeter wave phase shifters. Specifically, low-cost, compact phase shifters are required that can provide the full 360° range of phase shift while minimizing the associated insertion and mismatch losses.

The proposed approach for developing low cost and high performance tunable microwave devices and phase shifters is based on the utilization of ferroelectric materials. These materials are characterized by change in permittivity with an applied dc-bias voltage. This change in permittivity can be used to change the electrical length of a transmission line and, hence, in the design of low-cost phase shifters. $Ba_xSr_{1-x}TiO_3$ (BSTO) is commonly used, and recent advances in the development of these materials have resulted in lowering the dielectric constant ($\varepsilon_r \sim 100$), decreasing the loss tangent ($\tan \delta \sim 0.0009$), increasing the tunability ($\sim 20\%$), and in reducing the sensitivity of the material properties to temperature variations. It was, however, generally felt that phase-shifter designs based on this technology, although low cost, still exhibited unacceptably high insertion losses and impractical low input impedance values. Even with the implementation of the multi-dielectric layers designs in a microstrip transmission line arrangement [1], the resulting input impedance of microstrip and parallel plate type structures were unacceptably low.

A multilayer coplanar waveguide (CPW) with a thin low loss SiO_2 ($\varepsilon_r \sim 3.8$, $\tan \delta \sim 1e-4$) layer separating the conductors from the ferroelectric material was developed in [2]. The simulation results showed an improvement in insertion loss of up to 5 dB in conjunction with an improvement in return loss of up to 15 dB at 10 GHz for the unbiased state ($\varepsilon_r \sim$

723) compared to the direct metallization approach described in [3]. The multilayer design in [2] produced a figure of merit (FOM) of over 25 °/dB at 10 GHz for line length of 10 mm, where FOM is defined as the amount of phase shift (°) per decibel of insertion loss. The multilayer combination resulted in an overall reduced loss tangent without loss of tunability and phase shifting capabilities.

As may be expected, the inclusion of the multilayer dielectrics would complicate the implementation of the biasing circuit [2]. For the direct metallization approach the ferroelectric can be tuned using a simple bias tee arrangement. However, in the multilayer design the inclusion of the low-loss, low dielectric layer effectively "shorts out" the potential distribution and virtually eliminates the normal electric field component in the ferroelectric layer resulting in impractical biasing capabilities.

In this paper, we describe an alternative CPW phase shifter design approach that will enable biasing of the ferroelectric material using a simple bias tee. A via through the SiO_2 layer is employed to allow the conducting strip to contact the ferroelectric material without disrupting the crystal structure of the material. The signal conductor via approach is particularly well-suited in such applications due to its ease in fabrication and low cost design. The SiO_2 layer under the ground plane conductors maintains the overall low loss tangent without loss of tunability, input impedance, and FOM.

II. Simulated Models and Numerical Results

The multilayer CPW illustrated in Fig. 1 shows the cross section of the signal conductor in contact with the ferroelectric layer. For simulation purposes, WIPL-D [4] and LINPAR [5] were used to develop design curves for the aforementioned phase shifter.
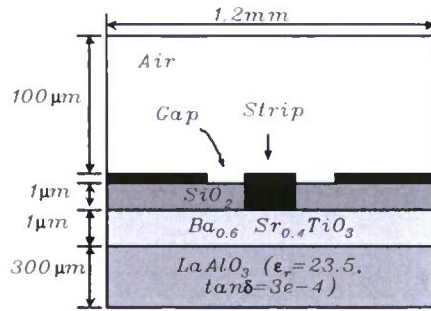
Fig. 1. Schematic of multilayer CPW where a via is formed in the SiO_2 (ε_r=3.8) layer to allow the conducting strip to contact the ferroelectric layer. The conductor thickness is 0.1 μm.

The characteristic impedance, attenuation, phase shift and FOM were simulated for the multilayer CPW at a frequency of 10 GHz for various strip widths and gap widths, exhibiting well-behaved design curves at this frequency. Fig. 2 depicts simulated data for the multilayer CPW with a dielectric constant of 700 (average between bias and unbiased states) and tan δ of 0.0075. Large strip and gap widths showed characteristics of high FOM, low attenuation, and 50 Ω characteristic impedance, and constitutes an improvement in attenuation of up to 0.7 dB/mm and a three fold improvement in FOM over the multilayer approach described in [3].

Increased phase shift may be realized by increasing the ferroelectric thickness; however, at the expense of increased attenuation. The 1μm BSTO and SiO₂ thicknesses were chosen based on the optimal tradeoff between phase shift and attenuation, or in other words for maximum FOM. The attenuation constant was further broken up into its associated dielectric and conductor losses (see Fig. 2c) where it was found that the conductor loss was the dominant contributor, and that minimal conductor losses may be achieved by increasing the signal conductor strip and gap widths. Furthermore, the conductor losses may be improved by increasing the conductor thickness.

(a)

(b)

(c)
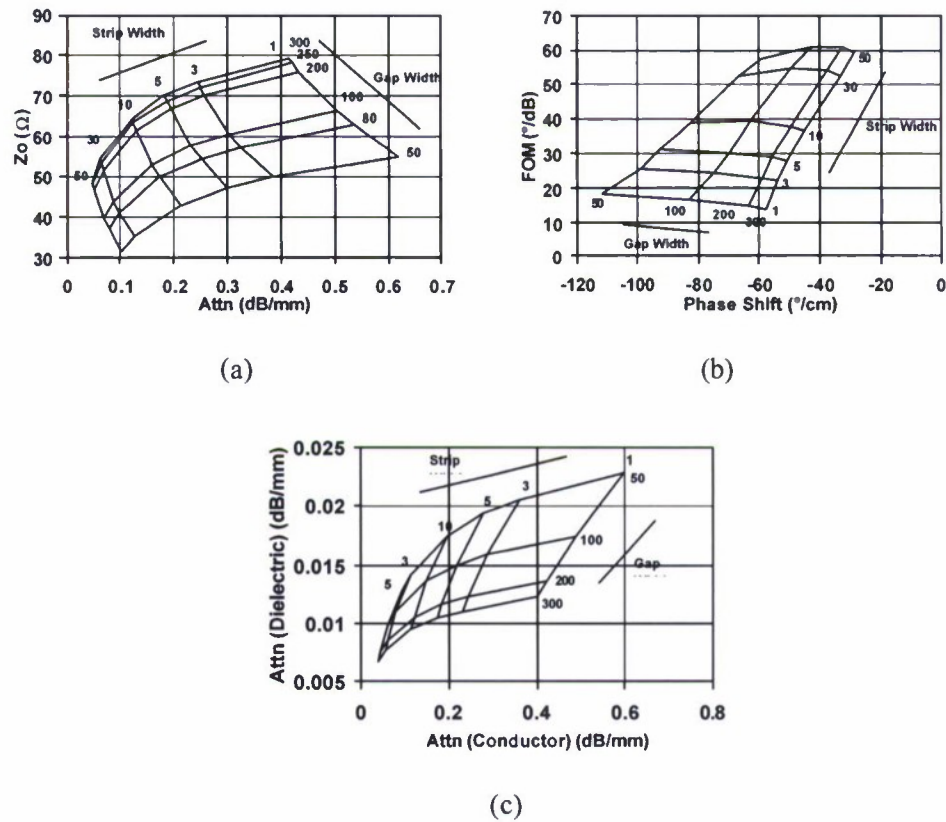
Fig. 2. (a) Impedance and attenuation, (b) FOM and phase shift, and (c) Dielectric and conductor attenuation at 10 GHz for various strip widths and gap widths, where $SiO_2 =$ BSTO = 1um.

Theoretical normal electric field (E_z) distributions were simulated for the phase shifter depicted in Fig. 1 with a strip width of 20 μm and gap width of 100 μm at a frequency of 10 GHz, exhibiting consistent normal field components over the entire cross section of the BSTO layer. The field distributions near the edge of the conducting strip depend exclusively upon the width of the conducting strip in conjunction with the BSTO layer thickness. Adequate polarization of the BSTO material was achieved with larger strip widths and 1 μm thick BSTO layer. As discussed previously the dimensions required for enhanced RF performance is consistent with those required for sufficient ferroelectric biasing.

III. Conclusion

A novel, high performance, and low cost multilayer ferroelectric phase shifter design where a via was formed in the SiO_2 layer to allow the conducting strip to contact the ferroelectric layer for simple ferroelectric biasing was proposed and its performance was simulated and numerically evaluated. It is shown that by including a low loss thin dielectric layer (SiO_2) between the coplanar conductors and the ferroelectric materials, significant reduction in insertion loss can be achieved (up to 0.7 dB/mm for unbiased case) and as high as three fold increase in the figure of merit ($^{\circ}$/dB) is possible compared with direct metallization approach. It was also found that the dimensions required for optimal RF performance is consistent with those required for sufficient ferroelectric biasing. This, in conjunction with the relative simplicity of the design and fabrication of the CPW phase shifter, makes it an ideal candidate for low-cost and high performance communication applications.

IV. References

[1] M. Iskander, Z. Zhang, Z. Yun, R. Isom, M. Hawkins, R. Emrick, B. Bosco, J. Synowczynski, and B. Gersten, "New phase shifters and phased antenna array designs based on ferroelectric materials and CTS technologies", *IEEE MTT*, vol.49, no. 12, pp. 2547-2553, Dec. 2001.

[2] W. Kim, M. Iskander, and C. Tanaka, "High-performance low-cost phase-shifter design based on the ferroelectric materials technology", *Electronics Letters*, vol. 40, no. 21, pp. 1345-1347, Oct. 2001.

[3] C. Krowne, M. Daniel, S. Kirchoefer, J. Pond, "Anisotropic Permittivity and Attenuation Extraction From Propagation Constant Measurements Using an Anisotropic Full-wave Green's Function Solver for Coplanar Ferroelectric Thin- Film Devices", *IEEE MTT*, vol. 50, no. 2, pp. 537-548, Feb. 2002.

[4] B. Kolundzija, J. Ognjanovic, and T. Sarkar, "WIPL-D: Electromagnetic Modeling of Composite Metallic and Dielectric Structures," Artech House, Norwood, MA., 1999.

[5] A. Djordjevic, M. Bazdar, T. Sarkar, and R. Harrington, "LINPAR for Windows," Artech House, Norwood, MA., 1999.

Modified Green's Function and Spectral-Domain Approach for Analyzing Anisotropic and Multidielectric Layer Coplanar Waveguide Ferroelectric Phase Shifters

Wayne Kim, *Member, IEEE*, Magdy F. Iskander, *Fellow, IEEE*, and Clifford M. Krowne, *Senior Member, IEEE*

Abstract—Phase-shifter design based on ferroelectric materials technology has shown promising performance characteristics and the potential for achieving the long standing goal of realizing high performance, low-cost microwave phase shifters, and phased-array antennas. In this paper, we present a unifying spectral-domain approach and a newly derived Green's function that provide a "first principles" method for the design and analysis of ferroelectric material based coplanar waveguide phase shifters. The modified Green's function not only accounts for the finite thickness of the conductors, but also for the "current crowding" phenomena that results from using the very high dielectric constant ferroelectric film. Both isotropic and anisotropic effects were analyzed and the developed theoretical results were in excellent agreement with measured data. It is also shown that the multidielectric layer-based design of these phase shifters may provide nearly threefold increase in the figure-of-merit compared with the direct metallization case. A new biasing approach is proposed to achieve effective biasing of the ferroelectric layer and without excessive field concentration in the overlaying low dielectric layer. The formulation, procedure for the calculation of the current and charge distributions, and comparison between simulation and experimental results are described and presented in detail.

Index Terms—Anisotropic, coplanar waveguide (CPW), ferroelectric, Green's function, phase shifter, spectral domain.

I. INTRODUCTION

MODELING ferroelectric coplanar waveguide (CPW) phase shifters has been and continues to be a computationally challenging endeavor because of the very thin layers (around 0.5–2 μm) in conjunction with possessing large dielectric-constant materials ranging from 100 to several thousand, depending on composition, applied voltage, operating temperature, and more importantly, the crystalline quality. In addition to the challenge of modeling these thin-film devices, the ability to accurately predict and identify the various loss mechanisms become computationally intensive as the device structures become increasingly complex. Losses in ferroelectric coplanar devices have consistently shown to be dominated by ohmic (conductor) losses associated with the guiding coplanar metal, as compared to other possible loss mechanisms [1], [2], particularly with recent advances in producing low-loss tangent ferroelectric materials. The attenuation due to ohmic losses may contribute up to 90% of the total loss budget [1].

In [1], the self-consistent dyadic Green's function contained in the spectral matrix method automatically calculates the substrate and ferroelectric material bulk losses. The ohmic (conductor loss), on the other hand, was treated in an alternative fashion. To model attenuation due to conductor losses, the self-consistent Green's function was modified to take into account both the intrinsic and extrinsic parameters of the coplanar device. The modified term was found to simultaneously model the attenuation and propagation characteristics with excellent accuracy. Although this method was effective, the extrinsic parameters were selected to fit measured data and did not allow the user to model the attenuation performance toward a desired goal.

In [2], the attenuation in ferroelectric coplanar devices is modeled based on the current crowding depth or the depth from the center and ground conductor edges at which 63% of the current flows. The current density was translated from the charge distribution on the electrodes by means of the quasi-TEM approximation [3]. It was found that the charge distribution was very high near the edges of the electrodes as the permittivity of the ferroelectric film increased in conjunction with implementation in thin-film technology. In terms of coplanar devices, these effects were considered extrinsic parameters. Although this method was effective, it will not accurately calculate the attenuation when the frequency increases significantly if the ferroelectric exhibits a high degree of anisotropy or if the ferroelectric device demonstrates multimode propagation.

In this paper, we combine the two models described above [1], [2] to form a new modified dyadic Green's function term that includes both the intrinsic and extrinsic parameters and develop a "first principles" approach to device modeling. The "first principles" approach refers to the ability to effectively design ferroelectric coplanar devices with prior knowledge of only a few measurements based on information such as basic materials properties and deposition techniques. The new Green's function will then be compared with measured results for verification. There are several available design options in the literature [4]–[6] and we have applied the new Green's function approach to the design in [1].
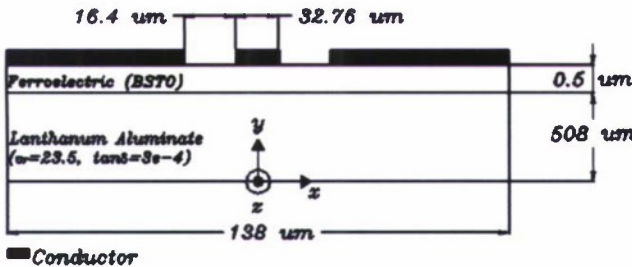
Fig. 1. Cross section of ferroelectric CPW phase shifter employing thin-film ferroelectric technology over lanthanum–aluminate substrate.

Following the development of the modified dyadic Green's function term, a study on the effects of the anisotropic and isotropic permittivity representations of the ferroelectric thin-film material will be presented. It would be beneficial to gain physical insight into which the tensor component dominates the overall device performance. The anisotropic and isotropic models will be compared with the measured results presented in [1].

The coplanar ferroelectric phase shifter exhibited high ohmic losses and could be deemed undesirable for implementation in practical wireless communication systems particularly in phased-array antennas. In an attempt to reduce the associated losses, the newly developed spectral matrix method will be used to effectively model a novel multidielectric design that will reduce the attenuation constant and improve the figure-of-merit (FoM). The multidielectric phase shifter employs a layer of low loss, nontunable dielectric material placed in between the ferroelectric material [$Ba_xSr_{1x}TiO_3$ (barium–strontium–titanate)], and the coplanar electrodes. Although this design has been described earlier [7], in this paper, we present a first attempt to fully analyze its performance using the spectral-domain approach together with the newly developed Green's function formulation.

II. FERROELECTRIC COPLANAR DEVICE MODELING

Fig. 1 illustrates the geometry of the thin-film ferroelectric coplanar phase shifter [1]. The structure uses barium–strontium–titanate ($Ba_xSr_{1x}TiO_3$) with a compositional ratio of $x = 0.6$ over a lanthanum–aluminate ($LaAlO_3$) substrate.

The total device width was 138 μm, the ferroelectric layer thickness was 0.5 μm, and the $LaAlO_3$ substrate layer thickness was 508 μm. The relative dielectric constant for the $LaAlO_3$ substrate was $\varepsilon_r = 23.5$ with $\tan \delta = 3e - 4$. The $\tan \delta_{fe}$ for the $Ba_{0.6}Sr_{0.4}TiO_3$ material was 0.01. The center strip width was 32.76 μm, the gapwidth was 16.4 μm, and the conductor thickness was 1.5 μm and was made of pure silver with resistivity $\rho = 1.629 \times 10^{-6} \Omega \cdot$ cm.

For the coplanar device, which was modeled as two coupled slots, with the fields in the slot locations expanded in a complete set of basis functions, the dyadic Green's function in admittance form is given by [1], [8]

$$G'_{ad} = \frac{1}{\det G'} \begin{bmatrix} G'_{zz} & -G'_{xz} \\ -G'_{zx} & G'_{xx} \end{bmatrix} \qquad (1)$$

where

$$\det G' = G'_{xx}G'_{zz} - G'_{xz}G'_{zx}. \qquad (2)$$

The Green's function in (1) is used in a system of homogenous equations to compute the propagation constant in the coplanar device as a function of frequency [8].

For modeling attenuation, it is important to note that in the spectral-domain approach described in [1], it was necessary to modify the self-consistent admittance Green's function terms in (1) to account for extrinsic parameters such as the finite thickness of the conductors and to account for the substantial amount of field lines that couple between and penetrate laterally into the coplanar arrangement. This modification was implemented to the diagonal elements of (1) and is given by

$$G'_{zz} = G_{zz} - \frac{1}{\sigma w_{\text{eff}}} \left\{ (1+j)\frac{t}{4\delta} + c(f)\frac{w_{cs}}{w_{cs} + 2w_{\text{slot}}} \right.$$
$$\left. \cdot \left[\frac{\frac{(1+j)w_{cs}}{\delta}}{\tanh\left[\frac{(1+j)w_{cs}}{\delta}\right]} \right] \right\} \qquad (3)$$

where

$$c(f) = \left(\frac{f}{f_o}\right)^k \qquad \delta = \frac{1}{\sqrt{\pi f \mu_o \sigma}} \qquad (4)$$

and where w_{cs} is the center conductor strip width, w_{slot} is the gapwidth of the CPW device, and w_{eff} is the newly quantified term, defined as the summation of the current crowding depths of the center and ground conductors [2]. A similar expression may also be used to modify the second diagonal term G'_{xx}.

The relation between current and charge density distributions may be given by

$$j_s(x) = qn_s(x)v = \rho_s v \qquad (5)$$

where $n_s(x)$ is the surface charge concentration and q is the electronic charge. Based on a study on the applicability of using a quasi-TEM approximation [3], we can assume no transverse currents in the CPW device; hence, the charge velocity v has only a longitudinal component and, therefore, the charge and current distributions are identical [2].

To calculate the charge/current distributions and, hence, to quantify w_{eff} in the two layer substrate illustrated in Fig. 1, we have employed the method of the finite-difference numerical method for multilayered structures. Since the finite-difference method is widely used and its derivation may be found elsewhere [9], [10], it will not be derived here. Considering computational efficiency, an unequal arm grid was employed taking into account the estimated concentration of charges, as shown in Fig. 2.

Shorter grids were implemented in regions where charges undergo rapid changes and wider grids in regions where the charges are relatively uniformly distributed or where the absolute value of the charge density is expected to be small. Along the x-direction, a fine grid was formed near the conductor–gap
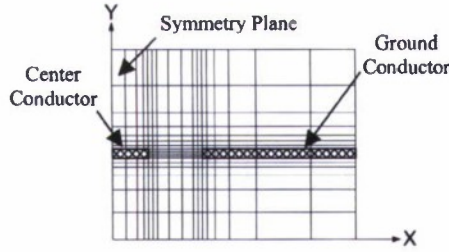
Fig. 2. Unequal arm grid illustrating the grid spacing with a high confinement of cells near the conductor to gap interface (x-direction) in conjunction with high confinement of cells near the conductor to substrate interfaces (y-direction). Symmetry was employed to further improve computation efficiency.

interfaces with a relatively coarser grid formed away from these regions. Along the y-direction, a fine grid was formed near the conductors and substrate interfaces and a relatively coarser grid further away. If N segments are taken for the number of cells in a specified region, then the cell spacings may be mapped according to the relation

$$\begin{pmatrix} x_i \\ y_i \end{pmatrix} = -a\cos\frac{i\pi}{N}, \qquad i = 0,\dots,N; \qquad \begin{pmatrix} -a < x < a \\ -a < y < a \end{pmatrix} \tag{6}$$

where x_i and y_i are the local coordinates.

To quantify the effect of current crowding, a current crowding depth (δ_{cc}), defined as the depth from the conductor edges at which 63% of the current is concentrated, may be defined as [2]

$$\int_{s-\delta_{cc}}^{s} j_s(x)dx = \left(1 - \frac{1}{e}\right)\int_0^s j_s(x)dx \tag{7}$$

where $j_s(x)$ is the surface current density, s is the width of the conductor, and $e = 2.718$.

Based on the current crowding expression in (7), the effective width w_{eff} in the modifying Green's function term (3) may be expressed by

$$w_{\text{eff}} = \delta_s + \delta_g \tag{8}$$

where w_{cs} is the width of the center strip, δ_s is the current crowding depth of the center strip, w_{gp} is the width of the ground plane, and δ_g is the current crowding depth of the ground plane.

III. CHARGE DISTRIBUTIONS

The charge/current distribution of the coplanar electrodes is illustrated in Fig. 3 for the center conductor and Fig. 4 for the ground-plane conductor. The charge distribution is evaluated by multiplying the normal component of the electric field with the equivalent permittivity surrounding the electrodes and is given by

$$\varepsilon_o\varepsilon_r E_{\text{norm}} = \rho_s. \tag{9}$$

The permittivity for the ferroelectric unbiased case was set to $\varepsilon_r\,(V_{\text{dc}} = 0\text{ V}) = 440 - j440\tan\delta_{\text{fe}}$, and the permittivity for the biased case was set to $\varepsilon_r(V_{\text{dc}} = 40\text{ V}) = 187.4 - j187.4\tan\delta_{\text{fe}}$, as was reported in [1], to satisfy both α and β simultaneously. The current crowding effect may be explained
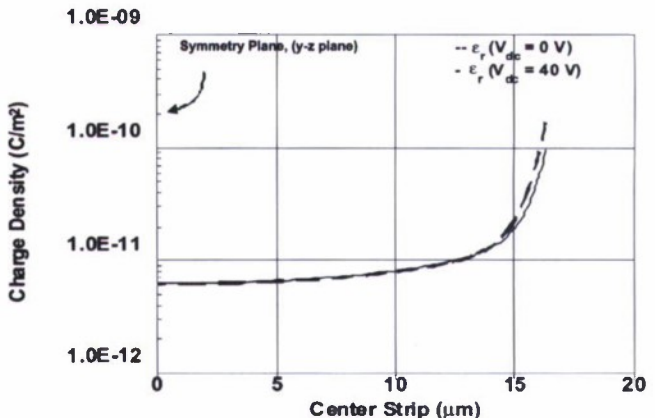
Fig. 3. Charge distributions on the center strip conductor for both biased and unbiased cases. Taking symmetry into account (see Fig. 1), only one-half of the center strip (from $x = 0$ to $x = 16.38\ \mu$m) is illustrated.
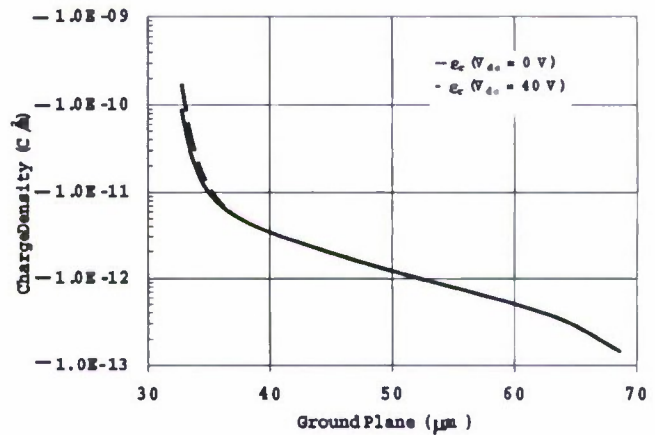
Fig. 4. Charge distributions on the ground-plane conductor for both biased and unbiased cases. Taking symmetry into account (see Fig. 1), only one side of the ground plane (from $x = 32.78$ to $x = 69\ \mu$m) is illustrated.

by the extremely high field confinement in the ferroelectric material as a result of the increase in permittivity. With increased film permittivity, the electric field is forced towards the edges of the electrodes, thus increasing the current crowding near the edges.

IV. ANISOTROPIC AND ISOTROPIC PERMITTIVITY COMPARATIVE STUDY

In [1], the unbiased ferroelectric case was modeled using a scalar permittivity given by $\varepsilon_r(V_{\text{dc}} = 0\text{ V}) = 440 - j440\tan\delta_{\text{fe}}$, and the biased ferroelectric case was modeled using a tensor permittivity given by

$$\varepsilon_r(V = 40\text{ V}) = \begin{bmatrix} 187.4 & 0 & 0 \\ 0 & 440 & 0 \\ 0 & 0 & 440 \end{bmatrix}$$
$$-j\begin{bmatrix} 187.4 & 0 & 0 \\ 0 & 440 & 0 \\ 0 & 0 & 440 \end{bmatrix}\tan\delta_{\text{fe}}. \tag{10}$$

The anisotropic values were determined based on a permittivity extraction algorithm described in [1]. Basically, the permittivity

values were iterated until the theoretical phase propagation constant agreed with the experimental results. We compare the tensor permittivity in (10) for the biased case to a scalar representation given by

$$\varepsilon_r(V = 40 \text{ V}) = \begin{bmatrix} 187.4 & 0 & 0 \\ 0 & 187.4 & 0 \\ 0 & 0 & 187.4 \end{bmatrix}$$
$$-j \begin{bmatrix} 187.4 & 0 & 0 \\ 0 & 187.4 & 0 \\ 0 & 0 & 187.4 \end{bmatrix} \tan \delta_{\text{fe}}. \quad (11)$$

V. RESULTS AND DISCUSSIONS

w_{eff} is determined by first calculating δ_s and δ_g by substituting (9) into (5) and using (7). w_{eff} is then determined using (8). With $f_o = 10$ GHz, $w_{\text{eff}} = 2.2 \ \mu\text{m}$, and $k = 0.373$ for the unbiased case and with $f_o = 10$ GHz, $w_{\text{eff}} = 2.9 \ \mu\text{m}$, and $k = 0.3428$ for the biased case, Fig. 5(a) and (b) shows the attenuation constant for the unbiased and biased cases, respectively, comparing measurement to theoretical results based on the above calculations. In matching the theoretical results to measurements, it was suggested in [1] that the excessive measured data excursions between approximately 5 and 10 GHz were questionable due to experimental errors, as well as device mismatches. Therefore, this data was not considered in the comparison. Similarly the presented simulation results ignored these questionable data. Fig. 5(c) depicts the measured phase shift compared to theory. The attenuation and phase shift show very good agreement between the experimental data and the presented theoretical results.

Fig. 5(b) and (c) also illustrates the comparison between anisotropic and isotropic ferroelectric permittivity models for the biased case.

It can be seen in Fig. 5(a) that the tensor and scalar representation of the ferroelectric permittivity are in exact agreement (same curve) and both are in good agreement with measured results.

The phase shift changes by up to $\sim 1.1°/\text{mm}$ at 20 GHz and is not considered a significant difference. Additional simulation results in which elements of the tensor dielectric matrix were changed one element at a time showed that the lateral tensor element (ε_{xx}) dominate the performance of the coplanar device as compared to the other tensor elements.

It should be noted that different ferroelectric film properties, as well as coplanar geometry may not result in such a strong ε_{xx} dependence. For the case of gap/ferroelectric film thickness ratio less than unity, it is expected that the rather strong transverse electric field components will be inhomogeneous with variations that are coordinate dependent and, hence, the need for a more careful anisotropic analysis. For example, results in which the gap/ferroelectric film thickness ratio was decreased to below unity demonstrates that the attenuation may change by up to ~ 0.75 dB/mm and that the phase shift may change by up to $\sim 20°/\text{mm}$ at 20 GHz, respectively, as a result of the large dependence on the perpendicular tensor components. These results are considered significant and would require anisotropic modeling. However, for the aforementioned coplanar geometry,

(a)

(b)

(c)
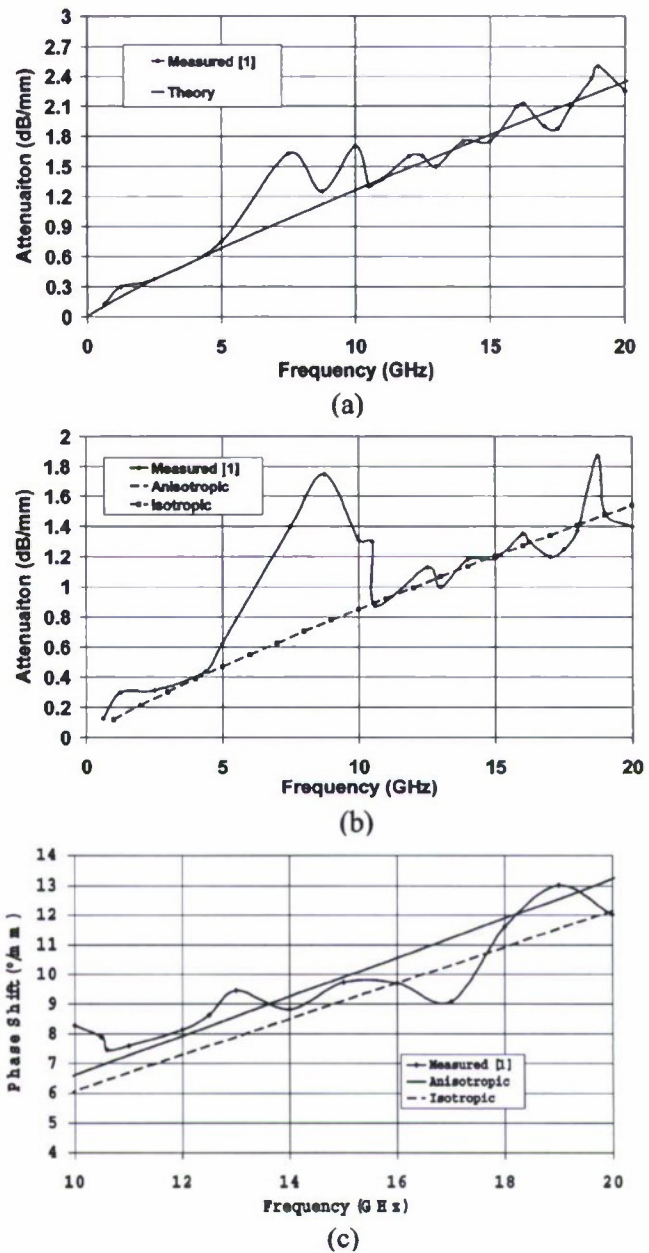
Fig. 5. (a) Attenuation constant for the unbiased case ε_r ($V_{\text{dc}} = 0$ V). (b) Attenuation constant for the biased case ε_r ($V_{\text{dc}} = 40$ V). (c) Phase shift versus frequency comparing experimental data to theory. The results also illustrate a comparison between anisotropic and isotropic ferroelectric permittivity representations.

the degree of anisotropy under biased conditions does not cause significant deviation from the isotropic model.

Both the spectral matrix and the method of finite difference were formulated in MATLAB. For the spectral matrix code, the number of basis functions used to expand the x and z components of the electric field in the CPW slots were set to $n_x = n_z = 3$, and the number of Fourier spectral terms was set to $n = 200$.

VI. MULTIDIELECTRIC COPLANAR PHASE SHIFTER

The attenuation constant illustrated in Fig. 5 may be considered too high for implementation in phased-array antenna

(a)

(b)
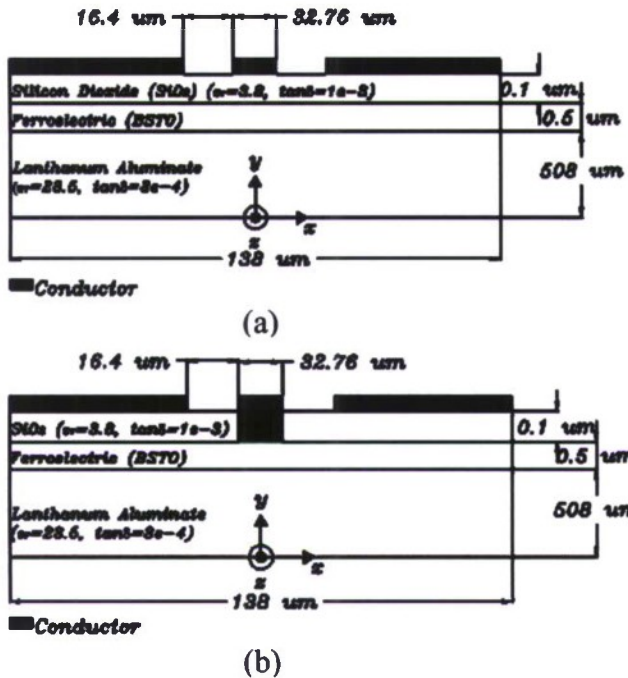
Fig. 6. Cross section of: (a) multidielectric ferroelectric CPW phase shifter employing very thin low-loss nontunable layer between the ferroelectric film and the coplanar electrodes and (b) multidielectric employing a via through the silicon–dioxide layer for simple ferroelectric biasing.

systems due to the anticipated high scan loss in conjunction with low radiation efficiencies. In an attempt to improve the phase-shifter performance, an alternate multidielectric layers design was proposed in [7]. Fig. 6(a) depicts a multidielectric ferroelectric phase-shifter design that employs the placement of a low-loss nontunable dielectric layer in between the ferroelectric material [$Ba_xSr_{1x}TiO_3$ (barium–strontium–titanate)] and the coplanar electrodes to reduce the attenuation constant and improve the FoM. The FoM is defined as the amount of phase shift per decibel loss, where the loss is calculated based on the unbiased condition. This new design was modeled in this paper using the method of finite differences and newly developed spectral matrix method.

The charge/current distribution on the coplanar electrodes is illustrated in Fig. 7 for the center conductor and Fig. 8 for the ground-plane conductor. Both Figs. 7 and 8 show results that compare the direct metallization case with the multidielectric case. The permittivity for the unbiased case was ε_r ($V = 0$ V) $= 440 - j440 \tan \delta_{fe}$, and the permittivity for the biased case was ε_r ($V = 40$ V) $= 187.4 - j187.4 \tan \delta_{fe}$.

For direct metallization, the charge distribution is forced towards the edges of the electrodes with increasing permittivity, thus increasing the current crowding near the edges. For the multidielectric situation [see Fig. 6(a)], the charge distribution is spread out across the electrodes and, hence, not highly concentrated near the edges and, thus, significantly reducing the current crowding effect.

Based on the charge distribution profiles and (8), with $f_o = 10$ GHz, $w_{eff} = 12.4$ μm, and $k = 0.373$ for the unbiased case and with $f_o = 10$ GHz, $w_{eff} = 10\mu$m, and $k = 0.3428$ for the
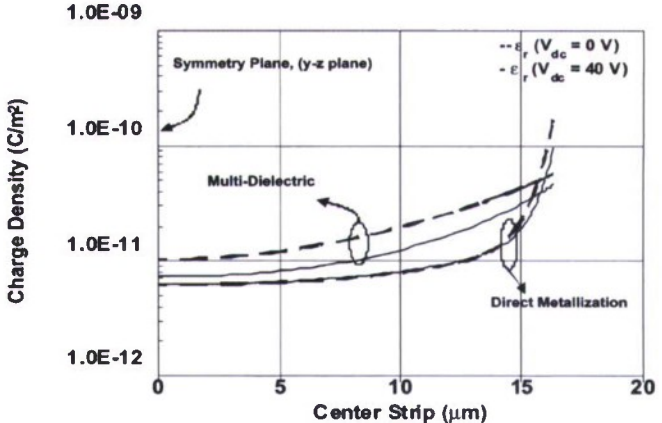
Fig. 7. Charge distributions on the center strip conductor for both biased and unbiased cases comparing the multidielectric and direct metallization cases. Taking symmetry into account (see Fig. 1), only one-half of the center strip (from $x = 0$ to $x = 16.38$ μm) is illustrated.
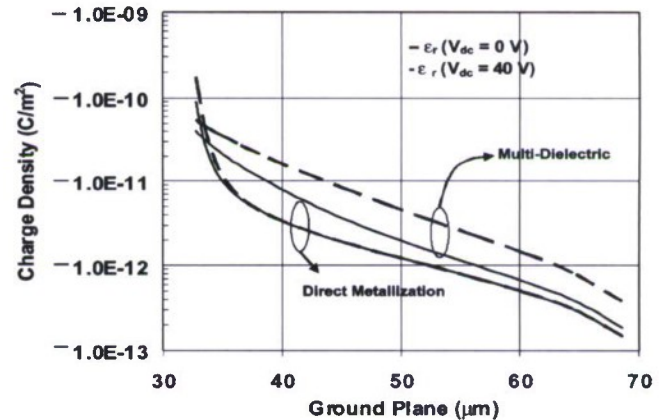
Fig. 8. Charge distributions on the ground-plane conductor for both biased and unbiased cases comparing the multidielectric and the direct metallization cases. Taking symmetry into account (see Fig. 1), only one side of the ground plane (from $x = 32.78$ to $x = 69$ μm) is illustrated.

biased case, Fig. 9 compares the attenuation constant of the direct metallization design illustrated in Fig. 1 to the multidielectric approach illustrated in Fig. 6(a) for the unbiased and biased cases. The attenuation constant decreased by ~1.85 dB/mm at 20 GHz for the unbiased case and decreased by ~1.07 dB/mm at 20 GHz for the biased condition.

The FoM results in Fig. 10 demonstrate a significant increase when using the multidielectric approach. The overall phase shift for the multidielectric design decreased by only ~ 3.6°/mm at 20 GHz compared to the direct metallization case, while there was a large decrease in the attenuation constant, and this is what resulted in the significant overall increase in the FoM ($^\circ$/dB). The FoM improved from ~ 6°/dB to ~ 20°/dB at 20 GHz and illustrates that the multidielectric design improves the overall phase-shifter performance.

As expected, the inclusion of the low-loss SiO_2 layer would complicate the implementation of the biasing circuit. For the direct metallization approach, the ferroelectric may be tuned using a simple bias-tee arrangement. However, in the multidielectric
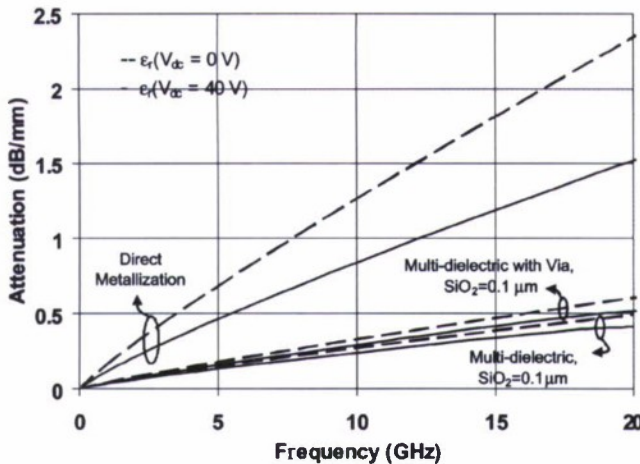
Fig. 9. Attenuation constant α for the unbiased $\varepsilon_r(V_{dc} = 0$ V) and biased ε_r $(V_{dc} = 40$ V) cases, comparing the direct metallization design shown in Fig. 1, the multidielectric design shown in Fig. 6(a), and the multidielectric with via design shown in Fig. 6(b).

Fig. 11. Characteristic impedance Z_o for the unbiased $\varepsilon_r(V_{dc} = 0$ V) case comparing the direct metallization design shown in Fig. 1, the multidielectric design shown in Fig. 6(a), and the multidielectric with via design shown in Fig. 6(b).

Fig. 10. FoM comparing the direct metallization design shown in Fig. 1, the multidielectric design shown in Fig. 6(a), and the multidielectric with via design shown in Fig. 6(b).

Fig. 12. Characteristic impedance Z_o for the biased case $\varepsilon_r(V_{dc} = 40$ V), comparing the direct metallization design shown in Fig. 1, the multidielectric design shown in Fig. 6(a), and the multidielectric with via design shown in Fig. 6(b).

design with a low-permittivity layer between the signal conductors and ferroelectric film, it is expected that the low-permittivity layer would effectively "short out" and E-field in the ferroelectric layer [11], [12]. It is important, therefore, that we address appropriate dc biasing for the ferroelectric material layer.

The multidielectric case in Fig. 6(b), which includes the formation of a via through the silicon–dioxide layer, was analyzed to determine the feasibility of effectively polarizing the ferroelectric substrate [11]. In this case, biasing would involve the use of a bias tee. As may be seen from Figs. 9 and 10, even with the new biasing approach, the proposed multidielectric phase-shifter design continues to provide reduced attenuation as well as increased FoM.

The characteristic impedance is illustrated in Fig. 11 for the unbiased and Fig. 12 for the biased case for each of the three phase-shifter designs. The increase in characteristic impedance observed for the multidielectric designs is a result of the decrease in distributed capacitance based on the inclusion of the silicon dioxide layer.

The increase in characteristic impedance allows for improved impedance match and, hence, is expected to result in fewer oscillations in the reflection coefficient response.

The multidielectric with a via possessed an increase in attenuation, decrease in FoM, and decrease in characteristic impedance compared to the multidielectric design without a via; however, the via design still presents a substantial improvement (nearly a threefold increase in FoM) over the direct metallization case. If one is willing to reduce the complexity of ferroelectric biasing, then the multidielectric with a via phase shifter is an attractive alternative for phased-array antenna systems.

VII. CONCLUSION

A modified Green's function term for modeling ferroelectric CPW devices was presented. The previously unknown extrinsic parameter, w_{eff}, as reported in [1], has been quantified as the sum of the current crowding depths of both the signal

and ground-plane conductors [2]. The newly derived Green's function provides a "first principles" approach to allow user the ability to accurately model high-permittivity ferroelectric CPW phase shifters.

Based on the observed results comparing the anisotropic and isotropic representation of the ferroelectric material, it was found the lateral component of the permittivity tensor, namely, the ε_{xx} component, dominated the device performance. The attenuation constant demonstrated no difference, while the phase shift displayed a slight difference of $\sim 1.1°/\text{mm}$ at 20 GHz. These results indicate that the ferroelectric material may be modeled using either tensor or scalar representations without significant inaccuracies.

The coplanar ferroelectric design employing direct metallization of the electrodes with the ferroelectric material resulted in unacceptably high attenuation constant. To improve the device performance, we have introduced a multidielectric design that incorporated a thin layer of low-loss nontunable dielectric between the electrodes and ferroelectric layer. The developed "first principles" approach was used to model the multidielectric design. To improve the ferroelectric biasing capabilities, the multidielectric design was modified to include a via through the low-loss nontunable layer [11]. It should be noted that as the voltage drop across the capacitor stack under the ground planes of the CPW is much smaller than that under the signal conductor, the designs in Figs. 1 and 6(b) are similar from the dc biasing point-of-view, and that the significant microwave improvement was achieved without compromising biasing. The new via design demonstrated nearly a threefold increase in the FoM over the direct metallization case and, hence, presents itself as being attractive for implementation in phased-array antenna systems.

REFERENCES

[1] C. M. Krowne, M. Daniel, S. W. Kirchoefer, and J. M. Pond, "Anisotropic permittivity and attenuation extraction from propagation constant measurements using an anisotropic full-wave Green's function solver for coplanar ferroelectric thin-film devices," *IEEE Trans. Microw. Theory Tech.*, vol. 50, no. 2, pp. 537–548, Feb. 2002.

[2] E. Carlsson and S. Gevorgian, "Effect of enhanced current crowding in a CPW with a thin ferroelectric film," *Electron. Lett.*, vol. 33, no. 2, pp. 145–146, 1997.

[3] G. L. Matthaei, K. Kiziloglu, N. Dagli, and S. Long, "The nature of the charges, currents, and fields in and about conductors having cross-sectional dimensions of the order of a skin depth," *IEEE Trans. Microw. Theory Tech.*, vol. 38, no. 8, pp. 1031–1036, Aug. 1990.

[4] F. Deflaviis, N. Alexopoulos, and O. Stafsudd, "Planar microwave integrated phase-shifter design with high purity ferroelectric material," *IEEE Trans. Microw. Theory Tech.*, vol. 45, no. 6, pp. 963–969, Jun. 1997.

[5] A. Kozyrev, A. Ivanov, A. Prudan, O. Soldatenkov, E. Hollman, V. Loginov, D. Ginley, and T. Rivkin, "Microwave phase shifter employing $SrTiO_3$ ferroelectric varactors," *Integr. Ferroelect.*, vol. 24, pp. 287–295, Mar. 1999.

[6] F. V. Keuls, R. Romanofsky, N. Varaljay, F. Miranda, C. Canedy, S. Aggarwal, T. Venkatesan, and R. Armes, "A Ku-band gold/$Ba_xSr_{1-x}TiO_3$/$LaAlO_3$ conductor/thin-film ferroelectric microstrip line phase shifter for room-temperature communications applications," *Microw. Opt. Technol. Lett.*, vol. 20, no. 1, pp. 53–56, 1999.

[7] W. Kim, M. Iskander, and C. Tanaka, "High-performance low-cost phase shifter design based on ferroelectric materials technology," *Electron. Lett.*, vol. 40, no. 21, pp. 1345–1347, 2004.

[8] A. A. Mostafa, C. M. Krowne, and K. A. Zaki, "Numerical spectral matrix method for propagation in general layered media: Application to isotropic and anisotropic substrates," *IEEE Trans. Microw. Theory Tech.*, vol. MTT-35, no. 12, pp. 1399–1407, Dec. 1987.

[9] M. Iskander, *Electromagnetic Fields and Waves*. New York: Waveland Press, 1992.

[10] N. Alexopoulos, "Integrated-circuit structures on anisotropic substrates," *IEEE Trans. Microw. Theory Tech.*, vol. MTT-33, no. 10, pp. 847–881, Dec. 1985.

[11] W. Kim and M. Iskander, "An integrated phased array antenna design using ferroelectric materials and the continuous transverse stub technology," *IEEE Trans. Antennas Propag.*, vol. 54, no. 11, pp. 3095–3105, Nov. 2006.

[12] D. Chase, L. Chen, and R. York, "Modeling the capacitive nonlinearity in thin-film BST varactors," *IEEE Trans. Microw. Theory Tech.*, vol. 53, no. 10, pp. 3215–3220, Oct. 2005.

[13] K. C. Gupta, R. Garg, and I. J. Bahl, *Microstrip Lines and Slotlines*, 2nd ed. Norword, MA: Artech House, 1996.

Wayne Kim (A'05–M'05) received the B.S. degree from the University of Hawaii at Manoa, in 1998, the M.S. degree from the University of California at Los Angeles (UCLA), in 2001, both in electrical engineering, and is currently working toward the Ph.D. degree at the University of Hawaii at Manoa.

From 1998 to 2001, he was with TRW Space and Electronics (now Northrop Grumman), where he was involved in the development of indium phosphide bipolar transistors, as well as monolithic-microwave integrated-circuit (MMIC) design including high efficient power amplifiers. He holds several patents. His current research interests include developing phased-array antennas, smart antenna systems, and associated microwave components for wireless communications.

Mr. Kim was the second place recipient of the Student Paper Contest award of the 2004 Applied Computational Electromagnetics Society (ACES) Conference. He was also a recipient of the 2006 Achievement Rewards for College Scientists (ARCS).

Magdy F. Iskander (S'72–M'76–SM'84–F'93) is currently the Director of the Hawaii Center for Advanced Communications (HCAC), University of Hawaii at Manoa. He is a Co-Director of the National Science Foundation (NSF) Industry/University Joint Cooperative Research Center between the University of Hawaii, University of Arizona, Arizona State University, Rensselaer Polytechnic Institute (RPI), and more recently, The Ohio Sate University. Prior to joining the University of Hawaii at Manoa, he was the Engineering Clinic Endowed Chair Professor of the university. From 1997 to 1999, he was a Program Director of the Electrical and Communication System Division, National Science Foundation. He coedited a special issue on wireless communications of the *IEICE Journal* (Japan). He authored the textbook *Electromagnetic Fields and Waves* (Prentice-Hall, 1992; Waveland Press, 2001). He has authored or coauthored over 180 papers in journals. He holds seven patents. He has made numerous presentations at conferences. He is the founding editor of *Computer Applications in Engineering Education* (CAE) (Wiley).

Dr. Iskander was the 2002 president of the IEEE Antennas and Propagation Society (IEEE AP-S), the 2001 IEEE AP-S vice president, and a 1997–1999 and 2001–2006 Administrative Committee (AdCom) member. He was also a Distinguished Lecturer for the IEEE AP-S (1994–1997). He coedited two special issues devoted to wireless communications of the IEEE TRANSACTIONS ON ANTENNAS AND PROPAGATION. He was the recipient of the 1985 Curtis W. McGraw American Society for Engineering Education (ASEE) National Research Award, the 1991 ASEE George Westinghouse National Education Award, the 2000 University of Utah Distinguished Teaching Award, and the 2002 Kuhina (Ambassador) Award, University of Hawaii at Manoa.

Clifford M. Krowne (S'73–M'74–SM'83) has been professionally affiliated with the Microelectronics Division, Lockheed Missiles and Space Company, Sunnyvale, CA, and the Watkins-Johnson Company, Palo Alto, CA. He was a faculty member with the Department of Electrical Engineering, North Carolina State University, Raleigh, and an Adjunct Professor of electrical engineering with the University of Maryland at College Park. Since 1982, he has been with the Microwave Technology Branch, Electronics Science and Technology Division, Naval Research Laboratory, Washington, DC. He has authored or coauthored approximately 190 or more conference and journal papers in solid-state electronics, microwave circuits, electromagnetics, and physics. He holds several patents. He has also authored major portions of four books for Academic Press in the Advances in Imaging and Electron Physics Series, as well as having contributed two chapters to Wiley's *Electrical and Electronics Engineering Encyclopedias.*

An Integrated Phased Array Antenna Design Using Ferroelectric Materials and the Continuous Transverse Stub Technology

Wayne Kim, *Member, IEEE*, Magdy F. Iskander, *Fellow, IEEE*, and W. Devereux Palmer, *Senior Member, IEEE*

Abstract—In this paper, a new integrated phased array antenna system employing the ferroelectric materials technology for electronic beam steering capabilities is described. The design integrates a ferroelectric coplanar waveguide phase shifter with the continuous transverse stub (CTS) array. The phase shifter employs a multi-dielectric substrate and includes a thin layer of silicon dioxide between the signal conductors and the ferroelectric material to reduce the insertion losses and produce good impedance matching. The coplanar waveguide-based multi-dielectric layer design demonstrated an effective ferroelectric biasing architecture and exhibited an increase in figure of merit by up to 8 °/dB from that of the direct metallization approach. An integrated two elements phased array antenna is developed and demonstrates linearly polarized radiation with $+/-20°$ of beam scanning between the unbiased and biased states of the ferroelectric phase shifter.

Index Terms—Continuous transverse stub (CTS) antenna, coplanar waveguide, ferroelectric, low cost, multiband antenna array, phase shifter.

I. INTRODUCTION

PHASED array antennas have and will continue to play critical roles in the development of wireless and satellite communications systems. The advancement of future wireless and radar applications requires the use of phased array antennas that are low cost and exhibit high efficiencies. In spite of the significant advances in the phased array antennas technologies, there has always been a significant need for developing high performance phased array antennas with beam steering capabilities. In this paper we describe a design towards achieving this goal. It involves the integrated use of ferroelectric materials and the CTS antenna array technology.

The coplanar waveguide fed continuous transverse stub antenna (CPW-CTS) was first demonstrated in [1], and advantages of this new design include low cost, light weight, low profile (compared to reflector and lens antenna systems), and a very simple planar microstrip feed configuration. The low cost design is achieved through the use of printed circuit technologies as opposed to traditional waveguide methods used for the continuous transverse stub technology [2]. Furthermore, CTS technology is known to be tolerance insensitive and hence is also low cost in manufacturing.

Our group has also recently developed a technique that employs a novel multidielectric approach to coplanar waveguide ferroelectric phase shifters where a layer of low loss, non-tunable dielectric such as silicon dioxide (SiO_2) was placed in between the ferroelectric material ($Ba_xSr_{1-x}TiO_3$ (Barium Strontium Titanate) and the conductors. This approach significantly improved the insertion loss by nearly three fold in conjunction with maintaining significant fraction of the tunability [3].

In this paper, we describe an integrated phased array antenna approach that combines the multidielectric ferroelectric phase shifter design and the CTS antenna technology to form a phased array antenna with electronic beam scanning capabilities. Compared to other microstrip phased array antenna designs, the CPW-CTS has the advantage of low dispersion, being compact, and provides continuous analog beam steering [2]. In addition, the coplanar waveguide feed is easy to integrate with front-end receiver components.

A new approach for biasing the ferroelectric material in the coplanar multidielectric structure was developed and simulation results under dc bias conditions demonstrates that the potential distribution penetrates deep into the ferroelectric film and is fully pronounced under the signal conductor. This uniform distribution verifies that the dc voltage requirement for the multidielectric design is equivalent to the direct metallization architecture. In addition, the phase shifter performance under these new biasing arrangements was examined and an increase in the figure of merit (FOM) by up to 8°/dB above that of the direct metallization approach was achieved.

The paper is organized as follows: Section II describes the phase shifter design including the new biasing procedure and ways and means for accounting for current "crowding" and dielectric anisotropy when evaluating its performance. Section III focuses on the design of coplanar waveguide CTS array antennas and its integration with the ferroelectrics to achieve the desired beam steering capability. Section IV summarizes the findings and concludes the paper.

II. PHASE SHIFTER DESIGN

The use of ferroelectric materials was met with extreme challenges as the high value of the dielectric constant of these materials results in a significant reduction in the input impedance of the loaded devices; hence, unacceptably large values of ohmic losses. Our group has recently developed a technique to overcome this difficulty by employing a novel multilayer dielectric materials design that, while overcoming the return loss and insertion loss limitations of available designs, resulted in a challenging biasing arrangement [3]. If dc biasing is to be done
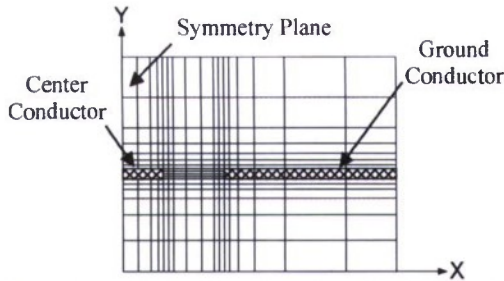
Fig. 1. Unequal arm grid showing grid spacing with a high confinement of cells near the conductor to gap interface (x-direction) in conjunction with high confinement of cells near the conductor regions (y-direction).
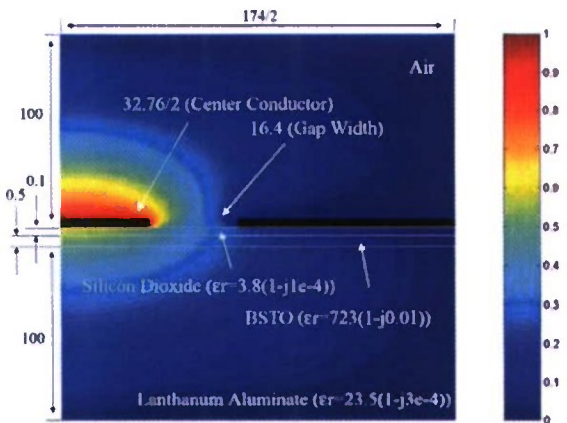

Fig. 2. Potential distribution over a cross section of the ferroelectric phase shifter where the phase shifter includes a thin layer of silicon dioxide between the conductors and the ferroelectric layer. The potential distribution employs symmetry, and the dimensions are given in microns.

through the regular biasing approach using a biasing tee, it is expected that much of the potential distribution will be concentrated in the SiO_2 layer above (rather than within) the ferroelectric layer. To help quantify the potential distribution across the ferroelectric substrate between bias states, and possibly lead to identifying a procedure for optimizing the biasing procedure, the method of finite differences was employed [4], [5].

Considering computational efficiency, an unequal arm grid was implemented taking into account the estimated concentration of charges. Shorter grids were used in regions where charges undergo rapid changes and wider grids in regions where the charges are relatively uniformly distributed or where the absolute value of the charge density is expected to be small. Along the x-direction in Fig. 1, a fine grid was formed near conductor-gap interfaces and a relatively coarser grid was formed away from these regions. Along the y-direction, a fine grid was formed near the conductors and substrate interfaces and a relatively coarser grid further away. If N segments are taken for the number of cells in a specified region, then the cell spacings may be mapped according to the relation

$$\begin{pmatrix} x_i \\ y_i \end{pmatrix} = -a\cos\frac{i\pi}{N}, \quad i = 0,\ldots,N, \quad \begin{pmatrix} -a < x < a \\ -a < y < a \end{pmatrix} \quad (1)$$

where x_i and y_i are the local coordinates running along the x- or y-directions, respectively. The unequal arm grid employing symmetry is illustrated in Fig. 1.

With a conductor thickness $= 1.5~\mu m$, and a ferroelectric permittivity of $\varepsilon_r = 723(1 - j0.01)$, Fig. 2 illustrates that
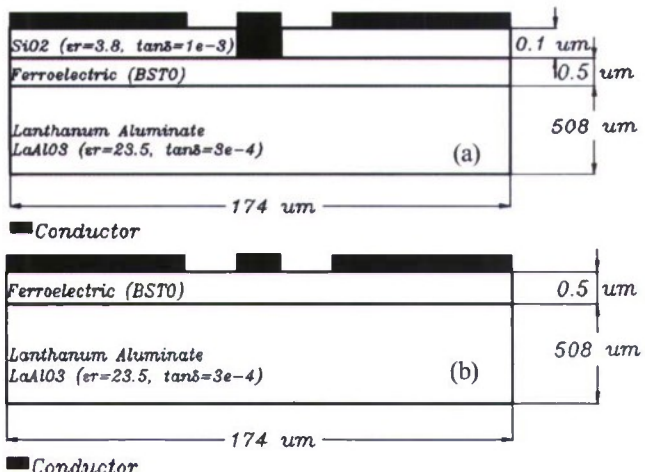
Fig. 3. (a) Cross section of ferroelectric phase shifter with the inclusion of a silicon oxide layer and the formation of a via hole under the signal conductor (b) phase shifter employing direct metallization. The metallization layers include: Cr/Ag/Au (250 Å, 14250 Å, 500 Å).

the potential distribution is primarily concentrated in the SiO_2 layer. Therefore, an alternative procedure is introduced to address the biasing issue as illustrated in Fig. 3(a). The new design includes the formation of a via through the silicon dioxide layer only under the center conductor while maintaining a thin layer of oxide under the ground plane regions. The direct contact between the center conductor and the ferroelectric layer allows for simple biasing. Simulation results of the potential distributions are shown in Fig. 4. These results compare the multidielectric design shown in Fig. 3(a) to the direct metallization design shown in Fig. 3(b) [6]. It can be seen that similar to the direct metallization case [6] with $V_{dc} = 1$ V, the potential distribution penetrates deeper into the ferroelectric material for the multilayer design. These results indicate that adequate polarization across ferroelectric material may be realized with the formation of a via through the silicon dioxide layer, under the center conductor. Because the multidielectric design possessed the same dimensions for coplanar center conductor width, gap width, and ferroelectric thickness as that of the direct metallization design presented in [6], the new multidielectric design will also require $V_{dc} = 40$ V [6] to properly polarize the ferroelectric film.

We next examined the microwave performance of the new design Fig. 3(a) of the coplanar phase shifter. For this purpose, we used three simulation codes and compared the results with experimental data for the special case of direct metallization of the ferroelectric material. Specifically, we used a method of moments based code (LINPAR) [7] to determine the per unit length transmission line parameters L, C, R, and G, a full 3-D method of moments code WIPL-D [8], and a spectral matrix based code [6], modified by our group. Results from these three codes were compared with the experimental measurements reported in [6].

It should be noted that WIPL-D [8] models 3-D composite metallic and dielectric structures using wires and plates. The finite conductor thickness is modeled using thin solid boxes. The distributed loading of the metallic plates may be given by the conductivity of the metal *or* as surface impedance given by [8]

$$Z_s = \frac{1}{t\sigma_m} \quad (2)$$

(a)

(b)
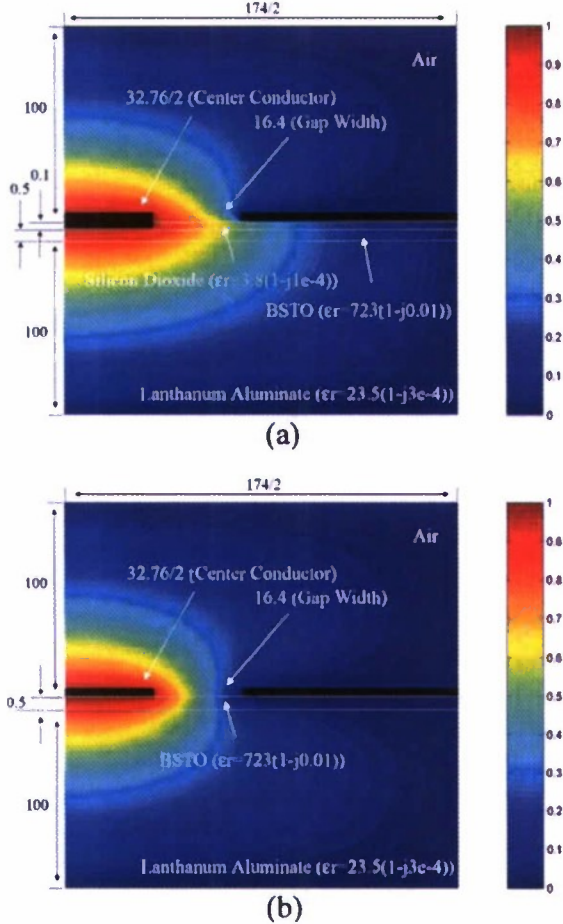
Fig. 4. Potential distribution over a cross section of the phase shifter for (a) multidielectric with via approach and (b) direct metallization approach. The potential distribution employs symmetry, and the dimensions are given in microns.
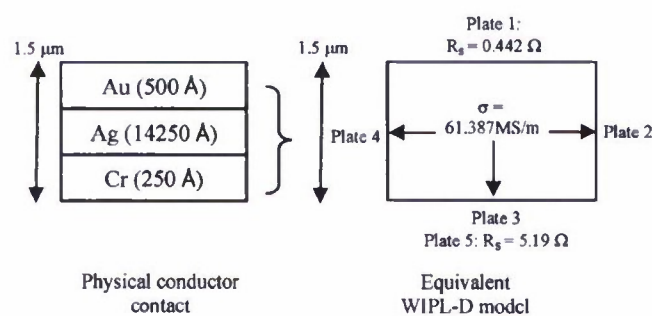
Fig. 5. Method for modeling metallization contacts in WIPL-D.

where t is the thickness of the metal and σ_m is the conductivity of the metal. The multiconductor combination which makes up the ohmic metal loss of the phase shifter device is modeled using metallic plates, each with a unique distributed loading depending on the layer it represents. Fig. 5 illustrates a method for modeling the metallic layer combination of Cr/Ag/Au (250 Å, 14250 Å, 500 Å). Plate 1 represents the gold (Au) metal layer, lies in the free space domain, and is assigned a surface impedance of 0.442 Ω where the conductivity is 45.21 MS/m. Plate 2 represents the silver (Ag) layer, plate 3 represents the silver (Ag) layer, and plate 4 represents the silver (Ag) layer.

Each of the aforementioned plates is assigned a conductivity of 61.387 MS/m and is in the free space domain. Plate 5 represents the chromium (Cr) layer and overlaps plate 3. Plate 5 is in the ferroelectric substrate domain and is assigned a surface impedance of 5.19 Ω where the conductivity is 7.714 MS/m.

The quick variations of the electromagnetic field at the interface between the microstrip conductor and the dielectric cannot be properly approximated by the low-order polynomial expansions associated with dielectric plates. This edge effect can be properly taken into account if the edge of a dielectric plate connected to the edge of a microstrip conductor is modeled by a separate narrow strip [8]. The length of the phase shifter is arbitrary since there is no variation in the z-direction. For our design the line length was kept short at 1 mm in order to keep the number of unknowns low while not generating any port-to-port coupling. A total of 299 unknowns were used in the model for good convergence.

LINPAR models 2-D multiconductor transmission line structures by defining node coordinates at the interface of two homogeneous boundaries. A pulse is then assigned between two adjacent nodes and the method of moments is employed using pulse basis functions. Higher concentration of nodes is employed where charges undergo rapid changes or where the absolute value of the charge distribution is expected to be high. The frequency dependent series resistance is modeled using the following relation [7]:

$$R(f) = R(f_{\text{ref}}) \left(\frac{f}{f_{\text{ref}}} \right)^{r_e} \tag{3}$$

where f_{ref} is the reference frequency, r_e is the exponential term defining the frequency variation of the series resistance, and $R(f_{\text{ref}})$ is the series resistance evaluated and the reference frequency given by

$$R(f_{\text{ref}}) = \sqrt{\frac{\pi \mu f_{\text{ref}}}{\sigma}} \tag{4}$$

where μ is the conductor permeability (in H/m), which is practically always equal to μ_o, and σ is the conductor conductivity given in S/m. For the device in Fig. 3(b), $f_{\text{ref}} = 0.1$ GHz, r_e is 0.917 for the unbiased case, $\varepsilon_r(V_{\text{dc}} = 0 \text{ V}) = 723(1 - j0.01)$ and r_e is 0.855 for the biased case, $\varepsilon_r(V_{\text{dc}} = 40 \text{ V}) = 441.2(1 - j0.01)$. The conductor was made of pure silver with a conductivity of 61.387 MS/m. A total of 982 nodes were used in the model to provide good convergence.

The spectral matrix code [6] was formulated in MATLAB and the number of basis functions used to expand the x and z components of the electric field in the coplanar waveguide slots were set to $n_x = n_z = 3$ and the number of Fourier spectral terms was set to $n = 200$. It is important to note that in the spectral domain approach described in [6], it was necessary to introduce the following modifying diagonal term in the admittance Green's function to account for the finite thickness of the conductors. This modification was also implemented in our code

$$Gs3 = \frac{1}{\sigma w_{\text{eff}}} \left\{ (1+j)\frac{t}{4\delta} + \text{c}(f)\frac{w_{cs}}{w_{cs} + 2w_{\text{slot}}} \right. $$
$$\left. \cdot \left[\frac{\frac{(1+j)w_{cs}}{\delta}}{\tanh\left[\frac{(1+j)w_{cs}}{\delta}\right]} \right] \right\} \tag{5}$$

where

$$w_{\text{eff}} = \delta_{\text{CentCond}} + \delta_{\text{GndCond}} \quad (6)$$

$$c(f) = \left(\frac{f}{f_o}\right)^v \quad \delta = \frac{1}{\sqrt{\pi f \mu_o \sigma}} \quad (7)$$

where w_{eff} is the summation of the current crowding depth of the center conductor (δ_{CentCond}) and the ground conductor (δ_{GndCond}) [9]. w_{cs} is the center conductor strip width and w_{slot} is the gap width of the coplanar waveguide device. $f_o = 10$ GHz, $w_{\text{eff}} = 1.98$ μm, and $v = 0.373$ for the unbiased case and $f_o = 10$ GHz, $w_{\text{eff}} = 2.97$ μm, and $v = 0.3428$ for the biased case. The values for w_{eff} obtained using the current crowding method [9] were in very good agreement with the values presented in [6] which were determined based on fitting measured data. The values determined in [6] were w_{eff} in [6] $= 2.004$ μm for the unbiased case and $w_{\text{eff}} = 3.021$ μm for the biased case. All simulations were performed using a Pentium 4 processor with 3.75 GB of RAM.

Fig. 6 compares the simulation results from the three simulation codes together with experimental data from [6].

As pointed out in [6], the experimental data between about 5 to 11 GHz was questionable and therefore should be ignored. In all models, the attenuation appeared to be dominated by ohmic losses. In addition to possessing high attenuation primarily due to ohmic losses, the direct metallization design also exhibited low characteristic impedance as shown in Fig. 6(d).

Fig. 6(a)-(c) show excellent agreement between simulation and experimental data. Although measured results for both S_{21} phase angle and the normalized propagation constant were also available in [6] it was found that it is possible to replicate the propagation constant and phase angle data above 10 GHz because the S_{21} phase angle data was presented with a jump at 7 GHz. Data for the normalized propagation constant was presented in [6] between 10–20 GHz and as a result, Fig. 6(c) shows measured results between 10–20 GHz. By multiplying the normalized propagation constant by k_o, in [6, Fig. 6] (free space propagation constant), the propagation constant of the coplanar waveguide could be obtained. In [6], the unbiased ferroelectric case was modeled using a scalar permittivity given by $\varepsilon_r(V_{\text{dc}} = 0$ V$) = 723(1 - j0.01)$, and the biased ferroelectric case was modeled using a tensor permittivity given by

$$\varepsilon_r(V_{dc} = 40 \text{ V}) = \begin{bmatrix} 441.2 & 0 & 0 \\ 0 & 723 & 0 \\ 0 & 0 & 723 \end{bmatrix}$$
$$- j \begin{bmatrix} 441.2 & 0 & 0 \\ 0 & 723 & 0 \\ 0 & 0 & 723 \end{bmatrix} 0.01. \quad (8)$$

We compare the tensor permittivity in (8) for the biased case to a scalar representation given by

$$\varepsilon_r(V_{dc} = 40 \text{ V}) = \begin{bmatrix} 441.2 & 0 & 0 \\ 0 & 441.2 & 0 \\ 0 & 0 & 441.2 \end{bmatrix}$$
$$- j \begin{bmatrix} 441.2 & 0 & 0 \\ 0 & 441.2 & 0 \\ 0 & 0 & 441.2 \end{bmatrix} 0.01. \quad (9)$$

(a)

(b)

(c)

(d)
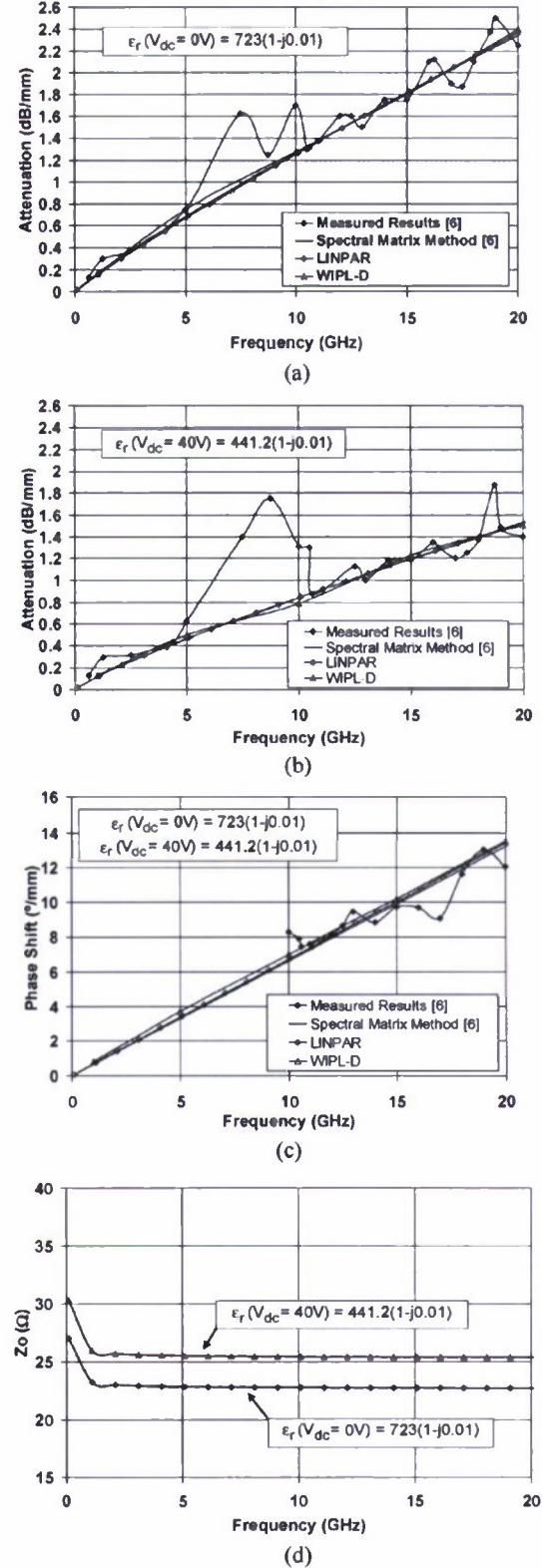
Fig. 6. Results of the direct metallization approach illustrated in Fig. 3(b), comparing measurement to the spectral matrix method [6], LINPAR, and WIPL-D: (a) attenuation for $\varepsilon_r(V_{\text{dc}} = 0$ V$) = 723(1 - j0.01)$, (b) attenuation for $\varepsilon_r(V_{\text{dc}} = 40$ V$) = 441.2(1 - j0.01)$, (c) phase shift, and (d) characteristic impedance.

Fig. 7(a) shows the attenuation constant and Fig. 7(b) shows the phase shift comparing the anisotropic and isotropic models. As
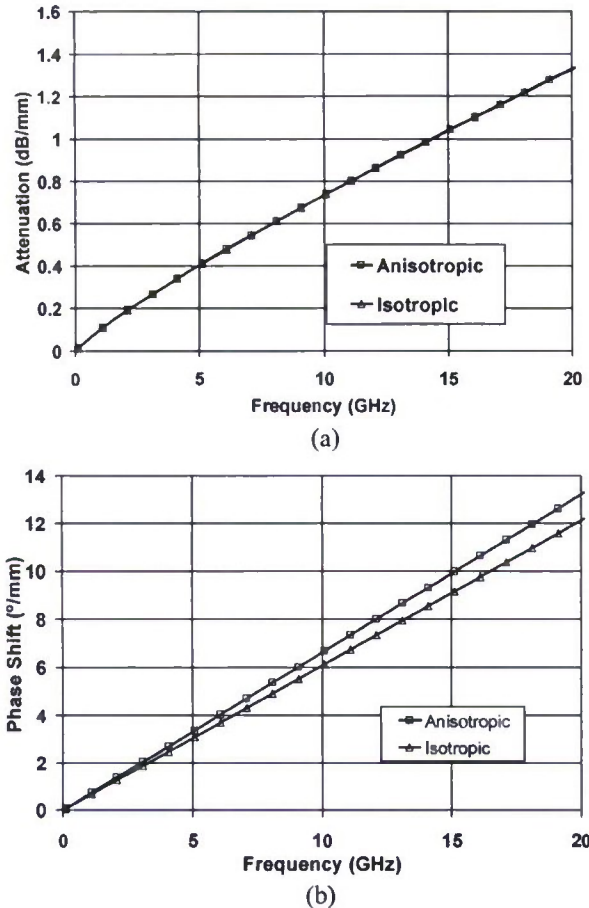
Fig. 7. (a) Attenuation and (b) phase shift versus frequency comparing the anisotropic and isotropic permittivity representations of the ferroelectric material.

can be seen in Fig. 7(a), the attenuation constant for the tensor and scalar representation of the ferroelectric permittivity are in exact agreement (same curve).

The phase shift data shown in Fig. 7(b) changes by up to $\sim 1.1°/\text{mm}$ at 20 GHz and is not considered a significant difference. Additional simulation results in which elements of the tensor dielectric matrix were changed one element at a time showed that the lateral tensor element (ε_{xx}) dominates the overall device operation as compared to the other tensor elements. The degree of anisotropy for the ferroelectric film under biased conditions is not substantial enough to cause significant deviation from the isotropic model and hence the device may be accurately modeled using the scalar representation.

With the validation of the simulation codes, it is important at this point to examine the phase shifter performance under this new biasing approach as shown in Fig. 3(a). For this purpose the new design with $\text{SiO}_2 = 0.1 \ \mu\text{m}$ was implemented and the simulation results were compared with the direct metallization approach shown in Fig. 3(b). WIPL-D was used to simulate the new phase shifter design. Fig. 8(a)–(d) show results of attenuation, characteristic impedance and figure of merit where WIPL-D was also used to model the direct metallization case. The ohmic metal loss was modeled according to the methods described in Fig. 5.
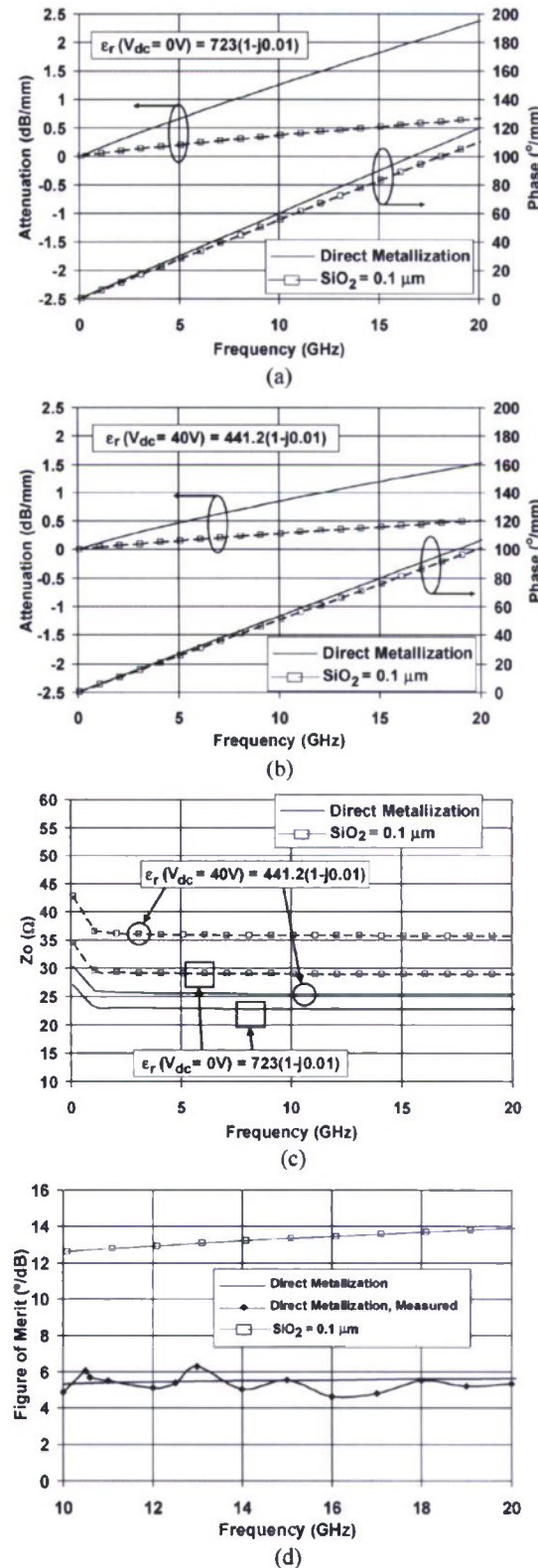
Fig. 8. Results of multidielectric design with 0.1 μm of silicon dioxide compared to the direct metallization case: (a) attenuation and phase for unbiased condition, (b) attenuation and phase for biased condition (c) characteristic impedance, and (d) figure of merit.

Fig. 8(d) shows that the figure of merit (FOM) improved by up to 8°/dB at 20 GHz, where the FOM is defined as the
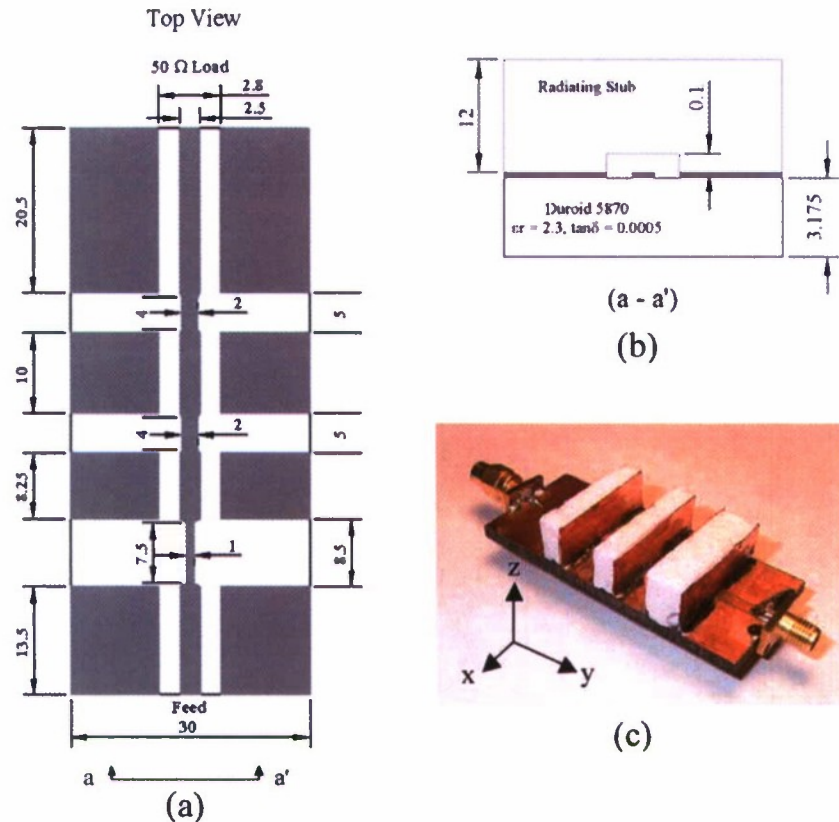
Top View

Fig. 9. Layout of the 3 elements CPW-CTS array, all dimensions in mm. (a) Top view, (b) front view and (c) fabricated prototype. Conductor thickness was 35 μm (1 oz.) electrodeposited copper with conductivity of 58.8 MS/m.

ratio between the amount of phase change and attenuation for the unbiased state. As it may be seen from Fig. 8, even with the new biasing approach (center conductor in contact with ferroelectric) the proposed multidielectric phase shifter design continues to provide reduced attenuation and increased characteristic impedance as well as an increase in the FOM. The increase in characteristic impedance is a result of the decrease in distributed capacitance with the inclusion of the SiO_2 layer. It may be noted that the phase for each ferroelectric state degraded slightly, resulting in a reduction in the overall phase shift. The overall FOM, however, is increased due to the relatively dominant decrease in attenuation.

III. CPW-CTS ARRAY AND PHASED ARRAY ANTENNA

First we extend the design of the single element coplanar waveguide continuous transverse stub (CPW-CTS) antenna presented in [1] to a traveling wave antenna with three series fed elements. The three element array was modeled using WIPL-D and a prototype was developed at X-band. Fig. 9(a)–(c) illustrate the dimensions of the array and show a photograph of the developed prototype. The dimensions of the coplanar waveguide feed and load lines were designed to provide 50 Ω impedance. The selected substrate was Duroid 5870 with a permittivity of 2.3 and tan δ of 0.0005. The center to center stub spacings were $\sim$ $\lambda_o/2$ and because of the low effective permittivity ($\varepsilon_{\mathrm{reff}} = 1.4$),

also $\sim \lambda_g/2$ for a design frequency of 10 GHz. The parallel plate stubs couple power from the microstrip transmission line feed and are carefully positioned in the areas of current maximums. Since this is a traveling wave antenna the first stub is designed to couple a small amount of power while the last stub couples relatively more. This is done by adjusting the width of each stub. The design was also implemented such that induced currents J_z on each stub are out of phase which is just the condition required for the electric field E_y radiated by each stub to be in phase in the direction of maximum radiation producing linear polarization and superb polarization purity.

The measured and simulated S_{11} of the CPW-CTS array is shown in Fig. 10(a). The 10-dB bandwidth of the CPW-CTS array was $\sim$4% and possesses narrow band characteristics, typical of resonant arrays with element spacing of $\sim \lambda_g/2$. The reflections from each stub combine in such a way as to cancel at the input of the array at only one frequency; hence the array has frequency dependent input impedance. The copolarized (E-plane, $y - z$ plane) and cross-polarized (H-plane, $x - z$ plane) radiation patterns are shown in Fig. 10(b) and illustrates that the linearly polarized array produced a broad side radiation pattern with a beam peak of 10.6 dBi at $-7.5°$ from broadside (towards feed direction) and a half power beam width of $\sim 36°$. The measured cross polarization level is below -20 dBi illustrating outstanding polarization purity. The slight deviation of the main beam from broadside towards the feed direction is a
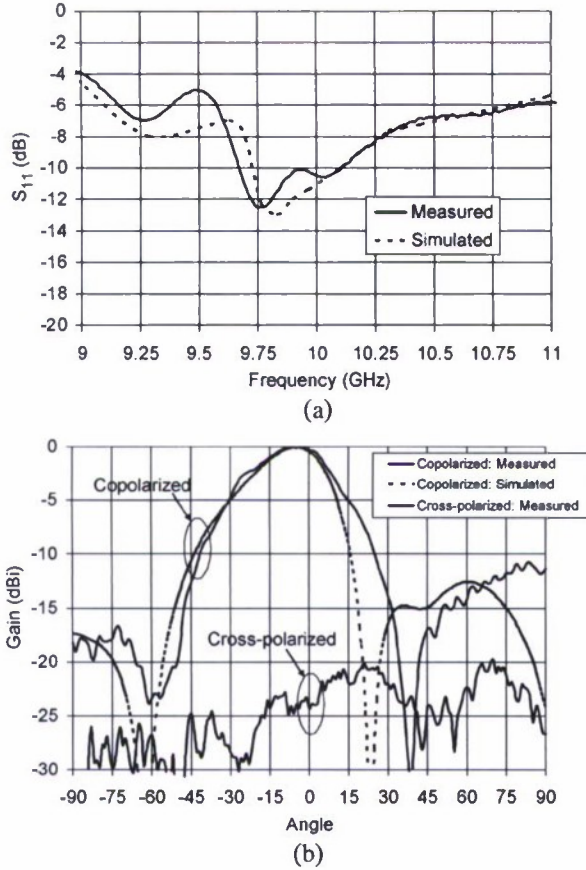
Fig. 10.   Measured results of (a) S_{11} versus frequency (b) copolarized (E-plane, $y - z$ plane) and cross-polarized (H-plane, $x - z$ plane) radiation patterns at 10 GHz versus angle.

result of the small increase in radiated power by the first stub element.

With this confidence and experimental validation of the simulation results for both the phase shifter and the multiele-ment CPW-CTS antenna array, we proceeded to simulate the desired integrated phased array antenna with beam steering capabilities. The newly designed ferroelectric phase shifter was integrated with the coplanar waveguide continuous transverse stub array to form a phased array antenna with electronic beam scanning capabilities. A detailed drawing of the devel-oped phased array antenna employing two radiating stubs is illustrated in Fig. 11(a)–(d). The multidielectric ferroelectric phase shifter allows appropriate tuning of the phase velocity, hence varying the guide wavelength enabling electronic beam steering capabilities. The multidielectric coplanar waveguide phase shifter described in Section II provides adequate tun-ability, good impedance matching, and low attenuation and is an attractive candidate for phased array applications.

To enhance coupling from the microstrip feed to the radiating stubs, the ferroelectric material is removed from under the radi-ating stubs as illustrated in Fig. 11(b). The section under the radiating stubs is filled with low permittivity SiO_2. Besides en-hancing the radiation from the stubs, this procedure is expected to further reduce the sensitivity of the integrated design to man-ufacturing tolerances. The radiating stub elements are also "V"

shaped which are narrow at the base and wider towards the top. The tapered geometry makes it possible to increase the distance and hence the phase shift between stubs. The narrow stub sec-tion couples power near the same current maximum on the trans-mission line feed. The center conductor of the coplanar wave-guide penetrates the silicon oxide layer and is in direct contact with the ferroelectric layer as shown in Fig. 11(b).

Simulations were performed using WIPL-D [8]. Due to the very thin layers of the SiO_2 as well as the ferroelectric layer, the computation "plates" run the risk of forming "non-convex" geometries where one dimension of the plate is much smaller than the other. This error can be overcome if the model contains plates with small dimensions, resulting in high concentration of plates in the ferroelectric sections and an overall increase in the number of unknowns. It was found that 12 plates for the multi-dielectric phase shifter provided the necessary convergence and accurate solution. Fig. 12 shows the WIPL-D model with a con-ductor thickness of 1.5 μm where the ohmic metal loss of the phase shifter is modeled according to the methods described in Fig. 5. The radiating stubs were made of copper foil with a conductivity of 58.8 MS/m. 5690 unknowns were used in the design.

Results in Fig. 13 show that with the center conductor width, $W = 13$ μm, gap width, $S = 300$ μm (to provide a 50 Ω transmission line impedance), $A = 9.8$ mm, $B = 13$ mm, and $C = 8.0$ mm, a ferroelectric thickness $T = 5$ μm, SiO_2 thickness of 0.1 μm, and a ferroelectric permittivity modula-tion between $\varepsilon_r(V_{dc} = 0 \text{ V}) = 723(1 - j0.01)$ and $\varepsilon_r(V_{dc} = 40 \text{ V}) = 441.2(1 - j0.01)$, approximately $+/- 20°$ of elec-tronic beam scanning is observed. The gain is ~ 5 dBi for the unbiased case and is ~ 2.8 dBi for the biased case resulting in ~ 2.2 dB of scan loss at 10 GHz. The half power beam width is $\sim 47°$ for the unbiased case and $\sim 46°$ for the biased case. As shown in Fig. 13(b), the cross polarization remains below -20 dBi for both ferroelectric conditions and demonstrates good po-larization purity, similar to that observed with the CPW-CTS array.

The CPW-CTS phased array is a non-resonant antenna array. The distance between radiating stub centers are not equal to $\lambda_g/2$ under either biased or unbiased ferroelectric states. It was designed to provide broadside radiation pattern at an interme-diate value of λ_g between the biased and unbiased cases. Thus a broadside radiation pattern is not observed under either the biased or unbiased ferroelectric cases. Based on the condition that the stubs are not spaced $\lambda_g/2$ apart the reflections from the different stubs do not add up in phase and the total reflection co-efficient at the input to the array is relatively small. Specifically, S_{11} for the unbiased case ($\varepsilon_r(V_{dc} = 0 \text{ V}) = 723(1 - j0.01)$) was -12 dB, and for the biased case ($\varepsilon_r(V_{dc} = 40 \text{ V}) = 441.2(1 - j0.01)$) was -18 dB.

While the above results illustrate the effectiveness of the pro-posed concept of integrated low cost phased array antenna, it should be noted that the proposed design provides ample op-portunity for alternatives and optimizations to fit specific appli-cations and needs. For example, a thinner ferroelectric substrate may be implemented to reduce the V_{dc} requirement of the phase shifter. In this case, we simulated another design with the thick-ness of the ferroelectric layer reduced to $T = 0.5$ μm, instead
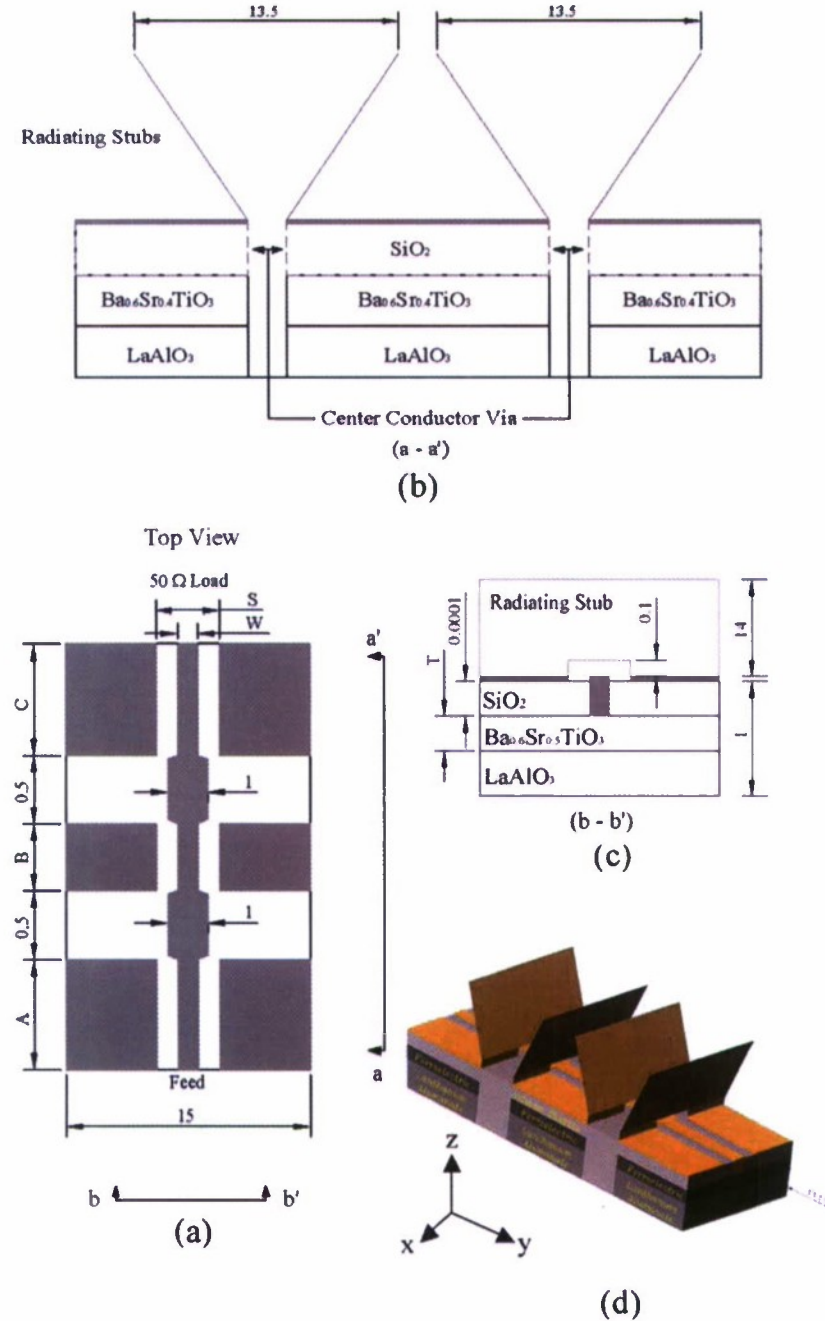
Fig. 11. Layout of the CPW-CTS phased array antenna. (a) Top view, (b) side view, (c) front view, and (d) perspective view, all dimensions in mm. The conductor thickness was 1.5 μm comprised of the multiconductor combination of Cr/Ag/Au (250 Å, 14250 Å, 500 Å).

of $T = 5$ μm, and the obtained results are shown in Fig. 14. For this design, the dimensions $W = 10$ μm, $S = 50$ μm, $A = 9$ mm, $B = 17$ mm, $C = 8.5$ mm, and the thickness of SiO$_2$ layer is 0.1 μm. From Fig. 14 it may be seen that approximately $+/-15°$ of electronic beam scanning was achieved. This is smaller than what was achieved when thicker ferroelectric layer was used, but the gain in this case is ~5.3 dBi for the unbiased case and is ~5.0 dBi for the biased case resulting in only ~0.3 dBi of scan loss, instead of 2.2 dBi scan loss for the earlier design, at 10 GHz. The half power beam width is ~ 42° for the unbiased case and ~ 41° for the biased

case. As shown in Fig. 14, the cross polarization remains below −20 dBi for both ferroelectric conditions and also demonstrates good polarization purity. S_{11} for the unbiased case ($\varepsilon_r(V_{dc} = 0$ V$) = 723(1 - j0.01)$) was −27 dB, and for the biased case ($\varepsilon_r(V_{dc} = 40$ V$) = 441.2(1 - j0.01)$) was −12 dB. In this case, since the distance between elements are longer (17 mm compared to 13 mm) than the previous case, 20 plates for the multidielectric phase shifter provided the necessary convergence.

These and similar design examples show that thinner ferroelectric layer may be employed thus leading to higher directive gain, lower scan loss, but would require an increase in the array
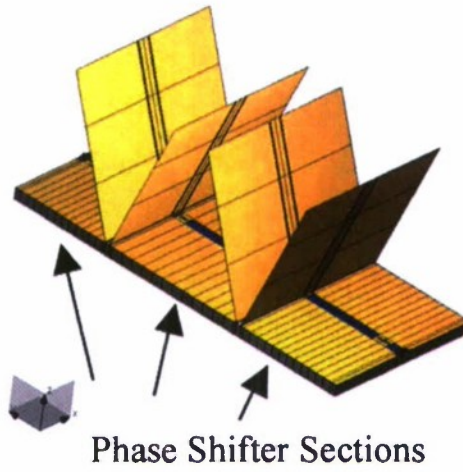
Fig. 12. WIPL-D model of two element CPW-CTS phased array illustrating the high concentration of plates in the multidielectric phase shifter sections.


(a)

(b)
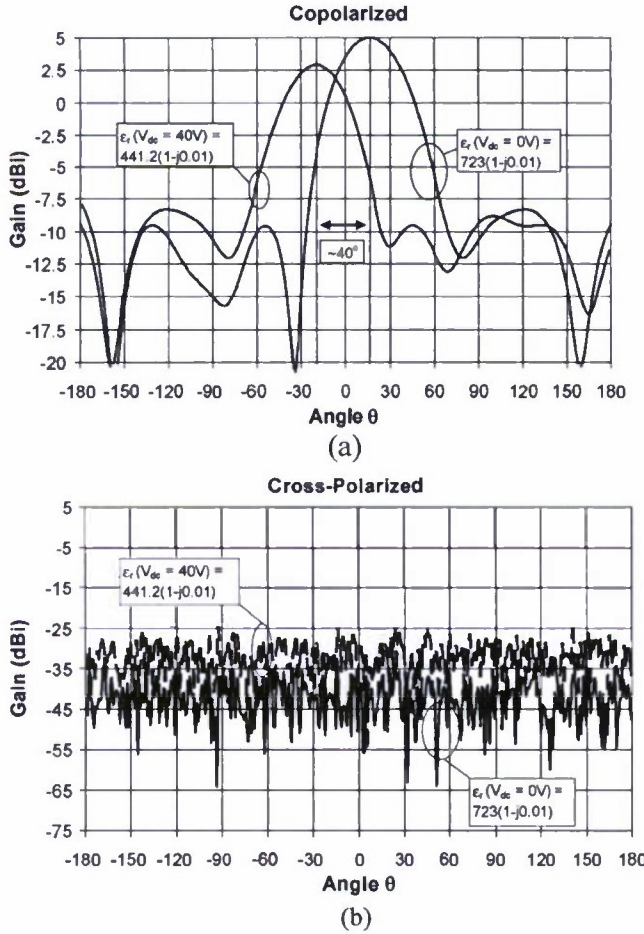
Fig. 13. (a) Co-polarized and (b) cross polarized radiation pattern of the phased array antenna shown in Fig. 11 at 10 GHz with $+/-20°$ of beam scanning.

(a)

(b)

Fig. 14. (a) Co-polarized and (b) cross polarized radiation pattern of the phased array antenna shown in Fig. 11 at 10 GHz with $+/-15°$ of beam scanning.

IV. CONCLUSION

A new biasing approach for the multidielectric layer phase shifter presented in [3] was developed and simulation results demonstrated its effectiveness in biasing the ferroelectric layer. The method of finite difference technique was used to quantify the potential distribution across the cross section of the ferroelectric device. It was found that the distribution was fully pronounced across the ferroelectric layer and that an equivalent voltage with that of the direct metallization case could be used to modulate the permittivity.

In this paper several modeling tools and numerical techniques were used to develop ferroelectric devices and phased array antennas. It is well known that the high permittivity and ferroelectric thin film technology makes modeling computationally intensive. We have presented several approaches to develop effective models. A first principles approach towards obtaining the effective width (w_{eff}) parameter in the Green's function spectral domain algorithm was presented and was in excellent agreement to the values obtained from fitting measured results [6]. If, however, the frequency dependence of attenuation is desired, other unknown parameters namely ν and f_o in (4) are

length. A thicker ferroelectric substrate, on the other hand, may be employed to reduce the overall array length; but this will result in a lower directive gain, increase in the scan loss, and will require larger dc bias, V_{dc}.

required to complete the analysis. The transmission line parameters obtained from LINPAR provides useful information; however as with the spectral domain method, modeling frequency dependent series resistance requires unknown parameters namely f_{max} and r_e in (3). The ability to parameterize individual metallic plates in WIPL-D allows the designer to generate an extremely close replica of the physical device and develop a very accurate model. For high attenuation devices such as ferroelectric phase shifters, a useful model for analyzing the ohmic metal loss was presented. However, the limitation of WIPL-D is that the dielectric domains are treated with isotropic permittivity.

The combination of the Green's function algorithm for analyzing the anisotropic characteristics of the ferroelectric material, LINPAR for determining the transmission line parameters and WIPL-D for full 3-D analysis provides a powerful combination for a first principles approach to ferroelectric device and antenna development. It was shown that the ferroelectric material characterized in [6] may be modeled with either an isotropic or anisotropic permittivity, thus allowing the use of WIPL-D. High frequency simulation of the new phase shifter design showed performance similar to the one reported earlier [3]. Specifically, improvement in both the attenuation and characteristic impedances were observed as well as an increase in FOM by up to $8°/dB$.

Furthermore, after experimentally verifying simulation results for the multielement CPW-CTS array, we presented results for an integrated phased array antenna with beam steering capabilities. Specifically, a two element phased array antenna with electronic beam scanning capabilities was designed at 10 GHz based on the integration of the multidielectric ferroelectric phase shifter and the coplanar waveguide continuous transverse stub array. The phased array antenna design is based on the new coplanar waveguide implementation described in [1]. The phased array produced nearly $+/-20°$ (or $40°$) of beam scanning in conjunction with possessing good impedance match. The use of a thinner ferroelectric layer results in a smaller scan of $+/-15°$ but higher gain and lower scan loss.

ACKNOWLEDGMENT

The authors are indebted to the four reviewers and the associated editor who provided invaluable comments and suggestions that truly contributed to the value of this paper. Their efforts and the detailed evaluation of the manuscript are acknowledged and wholeheartedly appreciated.

REFERENCES

[1] W. Kim and M. F. Iskander, "A new Coplanar Waveguide Continuous Transverse Stub (CPW-CTS) antenna for wireless communications," IEEE AWPL vol. 4, pp. 172–174, 2005 U.S. patent 7,079,082, Jul. 18, 2006.

[2] W. W. Milroy, "Continuous Transverse Stub (CTS) Element Devices and Methods of Making Same," U.S. Patent 5,266,961, Aug. 29, 1991.

[3] W. Kim, M. Iskander, and C. Tanaka, "High-performance low-cost phase-shifter design based on ferroelectric materials technology," Electron. Lett., vol. 40, no. 21, pp. 1345–1347, 2004.

[4] M. Iskander, Electromagnetic Fields and Waves. Prospect Heights, IL: Waveland Press, 1992.

[5] N. Alexopoulos, "Integrated-circuit structures on anisotropic substrates," IEEE Trans. Microw. Theory Tech., vol. MTT-33, no. 10, pp. 847–881, 1985.

[6] C. Krowne, M. Daniel, S. Kirchoefer, and J. Pond, "Anisotropic permittivity and attenuation extraction from propagation constant measurements using an anisotropic full-wave Green's function solver for coplanar ferroelectric thin- film devices," IEEE Trans. Microw. Theory Tech., vol. MTT-50, no. 2, pp. 537–548, 2002.

[7] A. Djordjevic, M. Bazdar, T. Sarkar, and R. Harrington, LINPAR for Windows. Norwood, MA: Artech House, 1999.

[8] B. Kolundzija, J. Ognjanovic, and T. Sarkar, "WIPL-D: electromagnetic modeling of composite metallic and dielectric structures," Professional Version 6.

[9] E. Carlsson and S. Gevorgian, "Effect of enhanced current crowding in a CPW with a thin ferroelectric film," Electron. Lett., vol. 33, no. 2, pp. 145–146, 1997.

Wayne Kim (S'98–M'00) received the B.S. degree from the University of Hawaii in 1998 and the M.S. degree from the University of California at Los Angeles in 2001, both in electrical engineering. He is currently working toward the Ph.D. degree at the University of Hawaii.

From 1998 to 2001, he was with TRW Space and Electronics (now Northrop Grumman) where he was involved in the development of indium phosphide bipolar transistors as well as MMIC design including high efficient power amplifiers. His research interests include developing phased array antennas, smart antenna systems, and associated microwave components for wireless communications. He has several patents.

Mr. Kim was the second place winner in the student paper contest for the Applied Computational Electromagnetics Society (ACES) conference in 2004. He was a recipient of the Achievement Rewards for College Scientists (ARCS) in 2006.

Magdy F. Iskander (F'93) is the Director of the Hawaii Center for Advanced Communications (HCAC), College of Engineering, University of Hawaii at Manoa, Honolulu, Hawaii. He is also a co-director of the NSF Industry/University joint Cooperative Research Center between the University of Hawaii, University of Arizona, Arizona State University, and the RPI in New York. He was a Professor of Electrical Engineering and the Engineering Clinic Endowed Chair Professor at the University of Utah for 25 years. He was also the Director of the Center of Excellence for Multimedia Education and Technology. From 1997–99 he was a Program Director, in the Electrical and Communication Systems Division at the National Science Foundation. While at NSF he formulated and directed a "Wireless Information Technology" initiative in the Engineering Directorate and funded over 29 projects in the microwave/millimeter wave devices, RF MEMS technology, propagation modeling, and the antennas areas. In 1986, he established the Engineering Clinic Program at the University of Utah to attract industrial support for projects for undergraduate engineering students and was the Director of this program since its inception. While in Utah, the program attracted more than 115 projects sponsored by 37 corporations from across the U.S. and resulted in an endowment for scholarships and a professorial chair held by the Director. Upon joining the University of Hawaii, he started a similar Engineering Clinic Program and in 2002–03 he had seven corporate sponsors. He was a member of the National Research Council Committee on Microwave Processing of Materials. He spent sabbaticals and other short leaves at Polytechnic University of New York; Ecole Superieure D'Electricite, France; UCLA; Harvey Mudd College; Tokyo Institute of Technology; Polytechnic University of Catalunya, Spain; and at several universities in China. He authored a textbook Electromagnetic Fields and Waves (Prentice Hall, 1992 and Waveland Press, 2001) edited CAEME Software Books (Vol. I, 1991, and Vol. II, 1994) and edited four other books on Microwave Processing of Materials, all published by the (Materials Research Society, 1990–1996). He is the Founding Editor of Computer Applications in Engineering Education (CAE). This journal is now in its 13th year, and received the Excellence in Publishing Award, by the Association of the American Publishers, in 1993.

He has published over 180 papers in technical journals, has seven patents, and has made numerous presentations in technical conferences. His ongoing research contracts include "Propagation Models for Wireless Communication," funded by the Army Research Office and NSF; "Low-Cost Phased Array Antennas," funded by both the Army Research Lab and NSF; and several other research projects sponsored by corporate sponsors including Raytheon, Trex, Motorola, Kyocera Wireless, Corning, Inc., and BAE Systems. He also recently established a new indoor antenna range and wireless testbed lab facilities at the University of Hawaii as a result of an NSF Major Research Instrumentation (MRI) grant.

Dr. Iskander received the 1985 Curtis W. McGraw ASEE National Research Award, 1991 ASEE George Westinghouse National Education Award, 1992 Richard R. Stoddard Award from the IEEE EMC Society, the 2000 University of Utah Distinguished Teaching Award, and the 2002 Kuhina (Ambassador) Award from the Hawaii Visitors and Convention Bureau. He was a member of the 1999 WTEC panel on "Wireless Information Technology-Europe and Japan," and chaired two panels on "Asian Telecommunication Technology" sponsored by DoD and organized by the International Technology Research Institute (ITRI) in 2001 and 2003. He edited a special issue of the IEEE TRANSACTIONS ON ANTENNAS AND PROPAGATION ON WIRELESS COMMUNICATIONS TECHNOLOGY, May 2002, which included contributions from the NSF funded projects, in 2004 co-edited a special issue of the *IEICE journal* in Japan (September 2004) on recent progress in Wireless Communications, and co-edited the 2006 special issue of IEEE TRANSACTIONS ON ANTENNAS AND PROPAGATION ON WIRELESS COMMUNICATIONS. He organized the first (2001) and the second (2003) "Wireless Grantees Workshop" sponsored by NSF and held at the National Academy of Sciences, and in Honolulu, respectively. He is the 2002 President of the IEEE Antennas and Propagation Society, Vice President in 2001, and was a member of the IEEE APS AdCom from 1997 to 1999. He was the General Chair of the 2000 IEEE AP-S Symposium and URSI meeting in Salt Lake City, UT, the General Chair of the IEEE Conference on Wireless Communications Technology, in 2003, in Hawaii, the General Chair of the 2005 IEEE/ACES joint conference on Wireless Communications and Applied Computational Electromagnetics, and the General Chair for the 2007 IEEE Antennas and Propagation International Symposium in Honolulu, HI. He also edited the 1995 and 1996 proceedings of the International Conference on Simulation and Multimedia in Engineering Education. He was a Distinguished Lecturer for the IEEE AP-S (1994–97) and during this period he gave lectures in Brazil, France, Spain, China, Japan, and at a large number of U.S. universities and IEEE chapters.

W. Devereux Palmer (S'89–M'91–SM'01) was born in Augusta, GA, in 1957. He received the B.A. degree in physics and the M.S. and Ph.D. degrees in electrical engineering from Duke University, Durham, NC, in 1980, 1988, and 1991, respectively. His field of graduate study was electromagnetic theory, and design, construction, and testing of microwave circuits and systems for practical applications.

From 1991 to 2001, he served on the technical staff at MCNC Research and Development Institute where he worked on a number of technologies including silicon vacuum microelectronics for microwave power amplifiers, polymeric MEMS structures, high-Q HTS filters, wide-bandgap semiconductors for power electronics applications, radio and optical communications systems, and optical and electronic packaging. In 2000, he became the Director of the MCNC-RDI Optical and Electronic Packaging group, where he managed programs in development of lead-free flip-chip bumping processes, bumping and assembly of high-density tiled detector arrays for particle accelerators, and packaging for OC-768 optical components. He holds the position of Adjunct Professor in the Department of Electrical and Computer Engineering at Duke University where he collaborates on research activities with other faculty members and graduate students, serves on graduate examination committees, and taught introductory electromagnetics for four semesters. Since his assignment to the U.S. Army Research Office, Research Triangle Park, NC, in 2001, he manages extramural basic research programs in computational electromagnetics, microwave and millimeter-wave circuit integration, compact and multifunctional antenna design, low-power communications systems, and power electronics.

Dr. Palmer is a Professional Engineer registered in North Carolina and a member of URSI Commission C and Commission D, the American Vacuum Society, the Materials Research Society, and Sigma Xi. He serves as the 2006–2008 Chair of the USNC-URSI Commission C. Within the IEEE, he participates in the Antennas and Propagation; Components, Packaging, and Manufacturing Technology; Electron Devices; Microwave Theory and Techniques; Power Electronics; and Professional Communications societies, served on the Vacuum Devices Technical Committee from 1997 to 2003, and served as Guest Editor for the T-ED Special Issue on Vacuum Electronics (January 2001) and the T-MTT Special Issue on Multifunctional RF Systems (March 2005). He currently serves as Secretary for the Eastern North Carolina Section in Region 3, and is a founding member and past Chair of the ACME (AP/CPMT/MTT/ED) local chapter.